Testing the binary black hole nature of compact binary mergers using gravitational wave observations

By

N V Krishnendu

A thesis submitted in partial fulfilment of the requirements
for the degree of Doctor of Philosophy

to

Chennai Mathematical Institute
December 2019

Chennai Mathematical Institute
Plot No. h1, SIPCOT IT Park,
Siruseri, Kelambakkam,
Tamilnadu - 603103
India

CHENNAI
MATHEMATICAL
INSTITUTE

N V Krishnendu

Plot No. h1, SIPCOT IT Park
Siruseri, Kelambakkam
Tamil Nadu, India 603 103
E-mail: krishnendu@cmi.ac.in

DECLARATION

I declare that the thesis entitled **"Testing the binary black hole nature of compact binary mergers using gravitational wave observations"** submitted by me for the degree of **Doctor of Philosophy in Physics** is the record of academic work carried out by me during the period from August 2014 to September 2019 under the guidance of Professor K G Arun and this work has not formed the basis for the award of any degree, diploma, associateship, fellowship or other titles in this University or any other University or Institution of Higher Learning.

N V Krishnendu
Chennai Mathematical Institute
September, 2019.

cmi
CHENNAI
MATHEMATICAL
INSTITUTE
Professor K G Arun

Plot No. h1, SIPCOT IT Park
Siruseri, Kelambakkam
Tamil Nadu, India 603 103
E-mail: kgarun@cmi.ac.in

CERTIFICATE

I certify that the thesis entitled **“Testing the binary black hole nature of compact binary mergers using gravitational wave observations”** submitted for the degree of **Doctor of Philosophy in Physics** by N V Krishnendu is the record of research work carried out by her during the period from August 2014 to September 2019 under my guidance and supervision, and that this work has not formed the basis for the award of any degree, diploma, associateship, fellowship or other titles in this University or any other University or Institution of Higher Learning. I further certify that the new results presented in this thesis represent her independent work in a very substantial measure.

Chennai Mathematical Institute
Date: September, 2019.

Professor K G Arun
Thesis Supervisor

Acknowledgements

I am grateful to my supervisor Prof. K G Arun for his constant encouragement and guidance throughout my Ph.D. I am very thankful to him for introducing me to the vast area of gravitational wave astronomy. We met almost every day and all those discussions were a new experience for me. He always surprised me with his way of interactions and immense patience. Most importantly, he paid attention to all my questions and that was just wonderful.

It was a great experience for me to visit the International Centre for Theoretical Science, Bangalore and I gratefully acknowledge Prof. Parameswaran Ajith for the insightful discussions and encouragements at different stages of my Ph.D. The group at ICTS always helped me understand various aspects of the subject better. I thank Abhirup Ghosh, Archisman Ghosh, Ajit Mehta, Gayathri Raman, M. K. Haris, Rahul Kashyap, and Sumit Kumar for those exciting times I had at ICTS.

I acknowledge the use of LIGO LDG clusters for the computational work done at various stages of my Ph.D. I also thank Chennai Mathematical Institute, Chennai and International Centre for Theoretical Sciences, Bangalore for giving access to their workstations.

I thank Prof. B. Sathyaprakash for all the interesting discussions we had at different stages of my Ph.D. I also thank him for making my visit to Pennsylvania State University possible. Those days I spent at Pennsylvania State University helped me a lot for my further research.

I thank Prof. Alok Laddha for encouraging me at every stage of my Ph.D. The reading courses he provided made me think differently about various topics related to black hole physics and advanced topics in general relativity. I also remember all the valuable comments and suggestions he provided as a doctoral committee member. I am grateful to Prof. L. Sriram Kumar for constantly monitoring the progress of my work and giving suggestions at every stage.

I gratefully acknowledge the support received from Prof. Chandra Kant Mishra starting from the early days of my Ph.D. It was a great experience working with Chandra and hope to continue working with him in the future.

From the initial stages of my thesis project Nathan Johnson-McDaniel has always been helping me with conceptual as well as computational doubts. His long emails been always a good reference whenever I was stuck with something.

I thank Prof. Bala Iyer for his valuable advice at different stages of my Ph.D. and constantly monitoring the thesis progress.

I gratefully acknowledge A. Samajdar and A. Gupta for guiding me through at difficult times both personally and academically.

I thank S. Kastha for all the wonderful interactions we had throughout the last five years.

I am grateful to M. Saleem for patiently listening to all my blunders and forgetting them. I had an entirely different experience working with him and hoping for more such occasions.

I thank Prof. Amitabh Virmani for all those fruitful discussions we had on different topics including black hole perturbation theory and tidal deformations of astrophysical black holes in general relativity. I also thank Prof. Sourish Das for giving his time to discuss with us many of the interesting ideas relating Bayesian statistics and gravitational wave astro-physcis.

The courses taught by Prof. H. S. Mani, Prof. T. R. Govindarajan, Prof. K. P. N. Murthy, and Prof. V. V. Shreedhar during our Ph.D. course work at CMI largely improved my understanding of various topics including classical mechanics, quantum mechanic, electromagnetic theory, general theory of relativity, statistical mechanics. I am grateful to Prof. H. S. Mani for giving me a chance to make a presentation titled gravitational wave astronomy on the occasion of science academies refresher course on quantum mechanics and that was a wonderful experience for me.

I am grateful to Prof. B. V. Rao, Prof. T. R. Ramadas, Prof. N. D. Haridas for constant support and encouragement.

I thank my friends Blessy, Ranjith, Atul, many others and all the teachers who taught us at the Government Higher Secondary School, Thrissilery, Kerala.

I would like to thank all my teachers and friends in Government college Madappally, Vatakara, Kerala. Especially, Prof. G. Hari Krishnan, Prof. Suresh Babu, Prof. Suneera, and Prof. Ramakrishnan. They taught us a lot of Physics as well as a bit of Philosophy of life. I had a second thought for doing masters in Malayalam only because of the presence of Prof. Veerankutty and Prof. Rajendran Edathumkara. I thank both of them for their immense help at any issue I had. I also thank Prof. K. B. Roy for many interesting discussions. I am grateful to all my friends from Madappally, they are just near to me whenever I need to talk.

I thank Prof. Titus Mathew, (late) Prof. V. C. Kuriakose and (late) Prof. M. Sabir of Cochin University of Science and Technology for many useful discussions and support which helped me pursue a Ph.D. in Physics.

The last year in CMI is unforgettable for me because of the time I spent with Anjali Yelikar, Aniket Khairnar, and Sayantani Dutta. It was not only a different academic environment but also helped me think more confidently about myself. Each day was special and I thank all of them.

Many thanks to Vishnu for being with me at the office, hostel, during our meals in the canteen, in Ramaniyam and the way back to TVH. That feeling of support is just awesome. I thank R. Govind for listening to me on any topic. I always felt comfortable talking with him irrespective of the content. Anbu is more close to me and I am grateful to him for keeping all of us always happy and energetic. The most beautiful experience ever was to share the office with my office mates Praveen, Murugan, Sumit, and Pritvijit (Vishnu and Anbu) and I wish if the same arrangement can last for more. We were together every single day of mine in CMI. I believe we will continue to be friends. I am grateful to all other colleagues in CMI and the pleasure we shared is of inestimable worth.

I have to remember the CMI coffee breaks, Krishna tea stall, Classic, all other random places we had snacks, chats, tea, coffee and anything else. I thank Vishnu Dath, KD, Ajjath, Sanjay, Gaadha, Pranav Ashok, Swati, Kishor Salunkhe, Navaneeth Mohan, Chinmay Kalaghatgi for joining with me at different places at different times.

The love and care I received from the CMI securities, cleaning staffs, Sajuettan and his team and all other workers are invaluable. I thank all of them and wishing a happy and prosperous life ahead.

I thank the CMI office staffs, Ranjini Girish, V Vijayalakshmi, Rajeswari, and S Sripathy.

Anjusha is with me from my Bachelor degree days and she always wanted me to stay happy and productive. I thank her for all that we exchanged for each other.

The most joyful company I got from CMI is Thomas and the bond I feel with him is very special. I thank him for all those moments we had together.

I got three amazing people in my life, Achhan, Amma, and Kannan. That is the force that makes me move forward and I am grateful for being with them.

N V Krishnendu
CMI, September 2019.

Abstract

We propose a novel method to test the binary black hole (BBH) nature of compact binaries detectable through gravitational wave (GW) interferometers and hence constrain the parameter space of other exotic compact objects. The spirit of the test lies in the "no-hair" conjecture for black holes where all properties of a Kerr black hole are characterised by its mass and spin. The method relies on observationally measuring the quadrupole moments of the compact binary constituents induced due to their spins. If the compact object is a Kerr black hole (BH), its quadrupole moment is expressible solely in terms of its mass and spin. Otherwise, the quadrupole moment can depend on additional parameters (such as equation of state of the object). The higher order spin effects in phase and amplitude of a gravitational waveform, which explicitly contains the spin-induced quadrupole moments of compact objects, hence uniquely encodes the nature of the compact binary. Thus we argue that an independent measurement of the spin-induced quadrupole moment of the compact binaries from GW observations can provide a unique way to distinguish binary BH systems from binaries consisting of exotic compact objects.

We quantify the expected statistical precision in measuring the spin-induced multipole moments using this method by means of the Fisher information matrix. Also, we implement this into the software package developed and currently used by the LIGO scientific collaboration and using this we obtain the first observational bounds on the spin-induced quadrupole moment parameter of a binary black hole system observed by the ground-based gravitational wave detectors. We further compute the projected accuracies with which the spin-induced multipole moments of a compact binary may be estimated with the future ground and space-based gravitational wave observatories.

Contents

List of Figures

List of Tables

Chapter 1

Introduction

1.1 Basics of gravitational waves

In 1916 Einstein proposed the existence of gravitational waves (GWs) as a consequence of his general theory of relativity [17]. Gravitational waves can be thought of as ripples in spacetime. They are transverse in nature and propagate at the speed of light according to Einstein's general theory of relativity. While electromagnetic waves are oscillating electric and magnetic fields that propagate through spacetime, gravitational waves are produced due to the oscillations of the spacetime itself. Unlike electromagnetic waves that are easily absorbed and scattered by the medium of propagation, GWs are hardly affected by the intervening medium due to the weak interaction of gravity.

Below we briefly describe gravitational waves in linearised general relativity. Einstein's equation connects spacetime geometry to the matter distribution in the following way,

$$\mathsf{R}_{\mu\nu} - \frac{1}{2}\mathsf{g}_{\mu\nu}\,\mathsf{R} = \frac{8\,\pi\,\mathsf{G}}{\mathsf{c}^4}\mathsf{T}_{\mu\nu}. \tag{1.1}$$

In Eq. (1.1), $\mathsf{R}_{\mu\nu}$ is called the *Ricci tensor*, R is the *Ricci scalar* and $\mathsf{T}_{\mu\nu}$ is the *energy momentum tensor* characterizing the source. Gravitation constant and the speed of light are represented by G and c respectively. The spacetime is completely specified the metric $g_{\mu\nu}$ which is characterized by, $\mathsf{ds}^2 = \mathsf{g}_{\mu\nu}\,\mathsf{x}^{\mu}\,\mathsf{x}^{\nu}$ where $\mu,\ \nu = 0,\ 1,\ 2,\ 3.$ In order to understand the wavelike solutions of Eq. (1.1) in a simple way, we assume that the spacetime is nearly flat and Einstein's equation can be studied as an expansion around flat spacetime. This method is called the linearized gravity approximation. In this case we write the spacetime metric $\mathsf{g}_{\mu\nu}$ as $\mathsf{g}_{\mu\nu} = \eta_{\mu\nu} + \mathsf{h}_{\mu\nu}$, where $\eta_{\mu\nu}$ is the flat spacetime metric (Minkowski) and $\mathsf{h}_{\mu\nu}$ is a small perturbation to it. How small is the tensor perturbation is not easy to define. But there exists a reference frame in which the numerical values of $\mathsf{h}_{\mu\nu}$ is less than 1. Linearized theory of general relativity has a redundant gauge freedom which is the invariance of the theory under the following coordinate transformations, $x^{\mu} \to x'^{\mu} = x^{\mu} + \zeta^{\mu}$. We define the following $\bar{\mathsf{h}}_{\mu\nu}$=$\mathsf{h}_{\mu\nu} - \frac{1}{2}\,\mathsf{h}\,\eta_{\mu\nu}$, $h = \eta^{\mu\nu} h_{\mu\nu}$ and in this case Eq. (1.1) reduces to,

$$\Box\bar{\mathsf{h}}_{\mu\nu} + \eta_{\mu\nu}\partial^{\rho}\partial^{\sigma}\bar{\mathsf{h}}_{\rho\sigma} - \partial^{\rho}\partial_{\nu}\bar{\mathsf{h}}_{\mu\rho} - \partial^{\rho}\partial_{\mu}\bar{\mathsf{h}}_{\nu\rho} = -\frac{16\,\pi\,\mathsf{G}}{\mathsf{c}^4}\mathsf{T}_{\mu\nu}. \tag{1.2}$$

The same gauge freedom can be used to choose Lorentz gauge, $\partial^{\nu}\bar{\mathsf{h}}_{\mu\nu} = 0$ and Eq. (1.2) reduces to,

$$\Box\bar{\mathsf{h}}_{\mu\nu} = -\frac{16\,\pi\,\mathsf{G}}{\mathsf{c}^4}\mathsf{T}_{\mu\nu}. \tag{1.3}$$

Equation (1.3) resembles that of the Maxwell's equations for electromagnetic fields which can be written as, $\Box\mathcal{A}_{\mu} = \frac{4\pi}{c}\,\mathcal{J}_{\mu}$. Here $\mathcal{A}_{\mu} = (\Phi,\, \tilde{A})$ represents the electric (Φ) and vector potential ($\tilde{A}$) while $\mathcal{J}_{\mu} = (c\rho,\, \tilde{J})$ denotes charge (ρ) and current densities ($\tilde{J}$) of the source. Unlike the second rank tensors in Eq. (1.1), electromagnetic field equations are vector equations. The same way electromagnetic field equations are sourced by the charge and current densities of the source, gravitational waves are wave equations sourced by energy momentum tensor of the gravitating source [1]. It is also important to emphasis that both electromagnetic and gravitational waves can exist in vacuum.

After solving Eq. (1.3) for a slowly moving source, where the time component of the metric perturbation can be neglected, with appropriate gauge choices (we work with the transverse-trace less gauge, often expressed as TT gauge [18]) one obtains the leading order solution as,

$$\mathsf{h}_{\mathsf{ij}}^{\mathsf{TT}}(\mathsf{t},\,\mathsf{x}) = \frac{2\,\mathsf{G}}{\mathsf{r}\,\mathsf{c}^4}\,\ddot{\mathsf{Q}}_{\mathsf{ij}}(\mathsf{t} - \mathsf{r}/\mathsf{c}), \tag{1.4}$$

where $(t - r/c)$ represents the retarded time, Q is the quadrupole moment of the source and r is the distance to the source. There are a few things to note here. The perturbation metric in the TT gauge can be expressed as a multipolar expansion of different source moments, similar to the electromagnetic waves (here we show only the leading order contribution). The monopole and dipole contributions to the expansion turn out to be zero as a consequence of conservation of mass and linear momentum of the source, respectively. Hence the leading order contribution to the gravitational wave

---

[1] Notice that sources are not necessary for gravitational or electromagnetic waves, cosmic micro wave background radiation is an example of one such case.

comes from the quadrupole moment in general relativity as shown in Eq. (1.4) and this equation is called the *quadrupole formula*. Hence, any source with non-vanishing second time derivative of quadrupole moment can emit gravitational waves and the amplitude is always inversely related to the distance to the source, r. Most importantly, the solution given in Eq. (1.4) has only two degrees of freedom left as a consequence of symmetries of Einstein's equations which we imposed through this particular gauge choice and the gravitational wave strain satisfies the conditions, $\mathsf{h}_{0\mu} = 0$, $\mathsf{h}^{\mathsf{i}}_{\mathsf{i}} = 0$ and $\partial^i \mathsf{h}_{\mathsf{ij}} = 0$. This implies that we finally obtain a transverse plane wave solution with two independent components correspond to two polarization states of the wave: the plus and the cross polarization. When a gravitational wave passes orthogonal through a ring of test masses, the relative separation between the test masses changes as an effect of the wave. This will change the shape of the ring depending upon the polarisation state of the gravitational wave. This property of gravitational waves is used in interferometric gravitational wave detectors. As in the case of electromagnetic theory where the Poynting flux is proportional to the square of the first time derivative of the vector potential, here the GW flux is proportional to the first time derivative of the amplitude of the GW given in Eq. (1.4). That is the GW flux is proportional to $\dddot{Q}_{ij}^{\,2}$. In the quadrupole approximation, we get the luminosity of gravitational waves as given by $\mathcal{L}_{\mathsf{gw}} = \frac{\mathsf{G}}{5\,\mathsf{c}^5}\left(\dddot{Q}_{jk}\,\dddot{Q}_{jk} - \frac{1}{3}\dddot{Q}^2\right)$.

The quadrupole moment $\ddot{Q}_{ij}(t - r/c)$ given in Eq. (1.4) can be expanded at the leading order as an integral of the mass density (time-time component of the stress tensor) as, $Q_{ij} = \int \mathsf{d}^3\mathsf{x}\,\mathsf{T}_{00}(\mathsf{t},\,\mathsf{x})\,\mathsf{x}_\mathsf{i}\,\mathsf{x}_\mathsf{j}$.

As an example, we take a two body bound system which evolve under gravitational radiation reaction. Assume the masses to be m_1, m_2 with reduced mass $\mu = \frac{m_1\,m_2}{m_1+m_2}$. The relative separation from the centre of mass of the system is denoted by a and the source is viewed along the angular momentum axis of the binary system. This means the inclination angle, which measures the angle between the observer's line of sight and the orbital angular momentum axis of the binary, is assumed to be zero. The non-vanishing contributions to the quadrupole moment tensor can be written as, $\mathsf{Q}_{11} = \mu\,\mathsf{a}^2\,\cos^2\phi$, $\mathsf{Q}_{22} = \mu\,\mathsf{a}^2\,\sin^2\phi$, $\mathsf{Q}_{12} = \mu\,\mathsf{a}^2\,\cos\phi\,\sin\phi$ and $\mathsf{Q}_{12} = -\mathsf{Q}_{21}$. The corresponding metric tensor takes the form,

$$\mathsf{h}_{\mathsf{ij}}^{\mathsf{TT}} = -\frac{4\,\mathsf{G}\,\mu\,\mathsf{a}^2\,\omega^2}{\mathsf{c}^4\,\mathsf{r}}\begin{bmatrix}\mathsf{h}_+ & \mathsf{h}_\times & 0\\ \mathsf{h}_\times & -\mathsf{h}_+ & 0\\ 0 & 0 & 0\end{bmatrix}. \tag{1.5}$$

The two independent components of the metric in this case are $\mathsf{h}_+ = \cos 2\phi$ and $\mathsf{h}_\times = \sin 2\phi$, where ϕ is the orbital phase and the gravitational wave phase will be twice the orbital phase at the leading order. The time derivative of the orbital phase, angular velocity, is denoted by the letter ω [19].

In order to compare the amplitude of the gravitational wave signals emitted from different sources, we will do a rough calculation by assuming a highly relativistic source, like a rotating neutron star with time varying quadrupole moment of the form $\ddot{Q}_{ij}(t - r/c) \sim \mathsf{m}\,\mathsf{v_{ns}}^2$ ($\mathsf{v_{ns}}$ is the non-spherical velocity), the expression given in Eq. (1.4) will be reduce to $\mathsf{h(t, x)} \sim \frac{2\,\mathsf{G}}{\mathsf{r\,c^4}}\,\mathsf{m\,v_{ns}}^2$ [19]. One can compare this with the Newtonian potential, $\phi(r) = \frac{\mathsf{G\,m}}{\mathsf{c^2\,R}}$ and we see that $\mathsf{h(t, x)} \sim \phi(\mathsf{r})\frac{\mathsf{v^2_{ns}}}{\mathsf{c^2}}$. Now if we place this neutron star system at a distance of $r \sim 60\mathsf{Mly}$ assuming $\phi(r) \sim 0.2\,c^2$ the GW amplitude will be $\sim 5 \times 10^{-22}$. For this system, an order of magnitude estimate for the GW luminosity can be obtained as follows, $\mathcal{L}_{\mathsf{gw}} \sim \frac{\mathsf{G}}{5\,\mathsf{c}^5}\,\dddot{Q}^2 \sim \frac{\mathsf{G}}{5\,\mathsf{c}^5}\,\left(\frac{\mathsf{G\,m}}{\mathsf{c^2\,R}}\right)^2\,\left(\frac{\mathsf{v_{ns}}}{\mathsf{c}}\right)^6$ and this is $\sim 10^{52}\,W$ for $\frac{\mathsf{v_{ns}}}{\mathsf{c}} = 1$ (measure of how relativistic is the source is) and $\frac{\mathsf{G\,m}}{\mathsf{c^2\,R}} = 0.5$ (called the compactness of the source). We summarize by saying that the GWs will be detectable only from a source which is highly relativistic and whose compactness is close to the maximum value.

1.2 Astrophysical sources of gravitational waves

As we discussed in the previous section, only sources of gravitational waves which are astrophysical in origin have the strength good enough to be detected by the currently available technology.

1.2.1 Gravitational wave burst sources

Gravitational wave burst sources are short duration (less than a few seconds) transients. Examples for these kind of sources are, supernovae, cosmic string cusps, high mass BBH merger etc. Data analysis algorithms which are capable of detecting burst sources look for excess energy (power) in the noisy data obtained from the detector. There are multiple transient search methods include coherent wave-burst (cWB) [20] and omicron-LALInference-Bursts (oLIB) [21] for the search of GW transients. Reference [22], reports the all sky search for short duration GW signals in the observation runs of second generation detectors and found no new signals.

1.2.2 Continuous gravitational wave sources

For continuous GW sources the GW frequency will remain almost a constant during the time over which the signal is observed. The strength of GW signal produced by these sources are several orders of magnitude weaker compared to coalescing binaries. One such source is spinning NS with non-axi symmetry (which has got a non-zero time varying quadrupole moment). As the star rotates, the non-axi symmetries of the star lead to the generation of gravitational waves. As far as the sensitivity of current ground based gravitational wave detectors are concerned the most interesting continuous GW sources are highly spinning galactic NSs. The detailed search for continuous GWs in the LIGO data is reported in Ref. [23].

1.2.3 Stochastic gravitational wave sources

Stochastic gravitational waves are background radiation can be of astrophysical (generated by superposition of the signals compact binaries, CW, supernova, etc) or primordial (produced in the early universe) origin. Unlike the other GW sources which comes from a particular direction of the sky, stochastic GW background may not be always directional. One example for a stochastic gravitational wave background from astrophysical origin which is directional could be where a large concentration of galaxies in some direction in the sky producing overlapping sources or signals. The strength of GW in different directions for stochastic backgrounds could be different and that is precisely what allows us to learn about the early universe. The gravitational wave signal is identified by cross correlating the data from multiple detectors [24].

The strength of the cosmological stochastic GW background predicted by the standard inflationary cosmology is too weak to be detected by current detectors but the astrophysical background from binary coalescence is expected to be detectable in the next few years with improved detector sensitivities of ground-based gravitational wave detectors. As reported in Ref. [25, 26], the current searches of stochastic gravitational wave data from ground-based detectors have produced interesting upper limits.

1.2.4 Compact binary coalescence

Another class, perhaps the most important and the one central to this thesis, of GW sources is the compact binary coalescence (CBC). A binary consisting of two compact objects merge under gravitational wave radiation reaction to form a new compact object. Given the compactness requirements for the detectability of gravitational waves (see Sec. 1.1) the binaries that are most promising are those composed of NSs or BHs.

Broadly, the compact binary dynamics consists of three major phases, inspiral, merger and ringdown. The initial stage of the dynamics, where the orbit start shrinking due to the GW radiation reaction and they come closer. As the orbital separation between the two decreases, the emission rate increases. This is called the *inspiral*. Depending upon the intrinsic parameters, especially masses and spin angular momenta, this process may take several millions of years. End of the inspiral leads to the merger of the compact binary system to form a new object. This highly relativistic stage is called *merger*. The merger remnant maybe highly deformed and emit GWs while it settles down to a stable configuration. This final regime of the binary dynamics is called the *ringdown*. From the inspiral to merger both the frequency and amplitude of the gravitational wave increases as a function of time and hence referred to as GW chirp.

One can model the inspiral phase using post-Newtonian formalism[27] whereas numerical relativity simulations are needed to model the merger regime [28]. In order to study the ringdown part of the dynamics, one may use black hole perturbation theory techniques [29]. The inspiral waveform is a function of the masses and spins of the binary components, the position and orientation of the source in the sky with respect to the observer and the distance to the source. The damped sinusoidal ringdwon radiation for a black hole is characterized by the frequency and damping time. Fig. 1.1 shows the gravitational waveform from inspiral-merger-ringdown dynamics of a binary black hole system.

The post-Newtonian (PN) approximation provides an accurate description of the dynamics of early inspiral of compact binary coalescence and here the relevant quantities are expressed as expansions of PN parameter, v/c [27]. There are many physical effects that appear in the waveform which can be modelled through the analytical techniques of PN theory. For example, the spin angular momentum [30], the orbital precession [31], the eccentricity of the orbit [32], the tidal deformations (due to the presence of external gravitating fields) [33], spin-induced deformations (arise due to spinning motion of the object) [34], the spin-tidal effects [35] etc.

The only reliable way to obtain the GW forms of CBCs near the merger to early ringdown is by solving Einstein's equations numerically, as the analytical methods such as post-Newtonian theory break down beyond a point. Solving the full Einstein

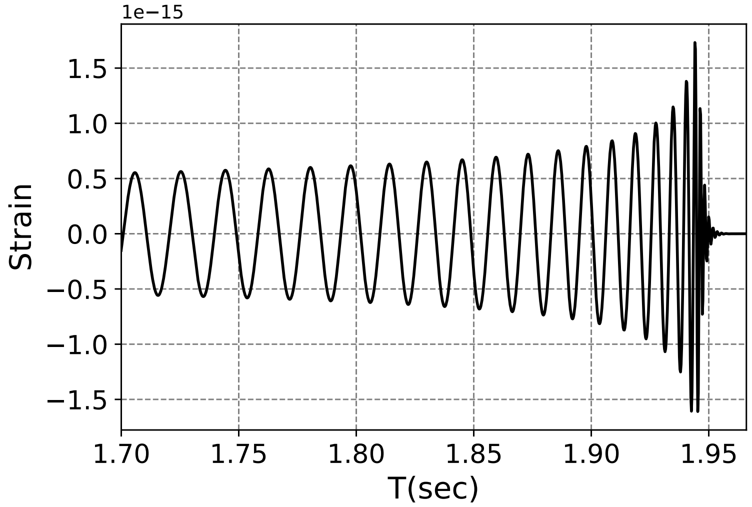

FIGURE 1.1: The gravitational waveform model of a non-spinning binary black hole system with a total mass of $30M_{\odot}$ and mass ratio of 2. As we discussed in Sec. 1.2.4, the dynamics can be broadly classified to three regimes, *inspiral*, *merger* and *ringdown*.

equations on a computer itself was a hard task and first done by Susan Hahn and Richard Lindquist in 1963 [36] following the theoretical calculations done by Charles Misner, Richard Arnowitt and Stanley Deser [37] for two black holes. This was further studied in Ref. [38] where the evolution starts with two black holes and collide to form a highly distorted black hole which emit gravitational waves to settle down to the stable state, this was the first demonstration of geometrodynamics using numerical relativity simulations. Even though many groups including the joint Cornell/Caltech Program to Simulate eXtreme Spacetimes (SXS) actively involved in studying the numerical simulations of two orbiting BHs, the orbital evolution and merger of a binary black hole system was first carried out by Frans Pretorius in 2005 [39]. This remarkable achievement lead to several other findings starting from the simple extension of this work to the spinning case [40, 41] and to the detailed catalog of BBH numerical waveforms with arbitrary spin magnitudes, orientations and mass ratios [42–44].

Solving the Einstein equation numerically and generate waveform models with thousands of cycles is computationally challenging. There are several approaches to build GW forms describing all the three phases of the binary dynamics by combining the inspiral part (analytical) and the numerical relativity part. For example, the Effective one body waveform families, which provides accurate analytical model for the inspiral-post inspiral phase of the binary, have been extended by fixing post inspiral coefficients from the numerical data describing the strong field regime [45, 46] which incorporates physical effects such as spins [47], tides [48] etc. In Ref. [49–52], authors developed a phenomenological family of waveforms where the PN inspiral phase is interpolated to merger ringdown phases by fitting unknown coefficients using numerical data. Recent extensions of this frequency domain waveform include spin precession effects [53], tidal effects [54] etc and has been used for GW searches and parameter extraction [55].

The inspiral-merger-ringdown features will vary with respect to the properties of the compact object constituting the binary system. More importantly, the predicted observational features in the gravitational waveform will strongly depend upon the underline theory (if it is not GR) and also on the nature of the compact object (if it is not a black hole or a neutron star).

The most accurate waveform models for compact binary coalescence are needed for both detection and parameter estimation of gravitational wave signals. In the next section, we discuss the matched filter analysis, which can be used to search for compact binary signals from the data consists of both true signal and noise. Further, we also give a brief overview of gravitational wave parameter estimation techniques emphasising the importance of most accurate waveform models.

1.3 Gravitational wave data analysis techniques and parameter estimation for compact binaries

Matched filtering is a general data analysis technique for searching known signals in a noisy data hence can be used to look for gravitational wave signals. In this section we discuss more details about the GW signal extraction techniques and parameter estimations once we provided with the GW strain data.

1.3.1 GW signal extraction from the data

1.3.1.1 Matched filter analysis for compact binaries

Matched filtering is a data analysis technique that efficiently searches for a GW signal from a compact binary system buried in a noisy data. A detector output consists of the gravitational wave signal and the background noise which can be written as,

$$s(t) = h(t; \overrightarrow{\theta_i}) + n(t), \tag{1.6}$$

For simplicity we start with the assumption that the noise to be stationary and Gaussian with zero mean, $\langle n(t)\rangle$=0. The auto-correlation function is defined as the correlation between noise at time t and t$'$, and is defined as, $K(t, t') = K(t-t') =< n(t)n(t') >$. For a wide sense stationary noise where, $K(t, t') = K(t+\tau, t'+\tau)$ where τ is infinitesimally small time translation. In this case the auto-correlation function depends only on τ the time difference, irrespective of the time t. We define $\tilde{n}(f)$ as the Fourier transform of $n(t)$ and in the Fourier space the auto-correlation takes the form, $\langle \tilde{n}(f)\tilde{n}^*(f')\rangle = S_n(f)\delta(f'-f)$. The Fourier transform of the correlation function $S_n(f) = \int_{-\infty}^{\infty} e^{2\pi i f'\tau} K(\tau)d\tau$ is called the power spectral density of the noise. Each detector is characterized by the noise spectral density, $S_n(f)$, we will discuss this in detail in the next section.

Suppose we define a cross correlation function, $C_{sq}(t) = \int_{-\infty}^{\infty} s(\tau)q(t+\tau)d\tau$ given the detector output $s(t)$ and a linear filter q(t). The matched filter analysis provides the optimal filter which maximises the ratio of mean of correlation function to its variance. This is called the matched filter SNR and is defined as $SNR = \frac{\langle C_{sq}(t)\rangle}{\sqrt{\langle (C_{sq}(t))^2\rangle - (\langle C_{sq}(t)\rangle)^2}}$. With appropriate substitutions, the above expression in the frequency domain simplifies to,

$$\mathrm{SNR} = \frac{\int_{-\infty}^{\infty} \tilde{\mathrm{q}}(\mathrm{f})\tilde{\mathrm{h}}^*(\mathrm{f})\mathrm{e}^{\mathrm{i}2\pi\mathrm{f}\mathrm{t}}\mathrm{df}}{\sqrt{\int_{-\infty}^{\infty} \mathrm{S_n}(\mathrm{f})|\tilde{\mathrm{q}}(\mathrm{f})|^2\mathrm{df}}}. \tag{1.7}$$

As we can see from this equation, the SNR is only a function of the $\tilde{q}(f)$ given the signal model $\tilde{h}^*(f)$. By invoking the Schwartz inequality, we can establish that the filter which maximizes the SNR will be $\tilde{q}(f) = A\frac{\tilde{h}(f)}{S_n(f)}$. The constant A is fixed by the normalization condition for the filter, $\int_{-\infty}^{\infty} S_n(f)|\tilde{q}(f)|^2 df = 1$. It is evident from the above expression that the filter obtained by this procedure is not just a copy of signal but it is weighted by the noise PSD. From this, we can re-express the SNR in terms of the optimal filter,

$$\rho = \sqrt{\int_0^{\infty} \frac{|\tilde{h}^*(f)|^2}{S_n(f)} df}. \tag{1.8}$$

Here, $S_n(f)$ has dimensions of time since this quantity is defined in frequency domain conventionally we follow the dimension as Hz^{-1}. In Fig. 1.4, we show the power spectral densities of various ground and space-based gravitational wave detectors.

To perform the searches for compact binaries one can cross correlate the data with waveform models predicted by general relativity using the *matched filter* analysis described above. PyCBC [56] and GstLAL [57] are two independent pipelines one can use to calculate the matched filter SNR given the gravitational wave strain data.

1.3.2 Parameter estimation techniques for compact binary coalescence

1.3.2.1 Parameter estimation using the Fisher Information Matrix analysis

When we have an accurate model for the signal of interest and the expected sensitivity of the detector, Fisher information matrix approach can be used to compute the expected 1-σ error bars on the parameters of the signal [58] assuming the noise in the detector is Gaussian-stationary and the signal-to-noise ratio is high. A quick review of Fisher information matrix formalism is given here. More details can be found in [58].

As shown in Eq. (1.6), the data contain noise and hence the measured parameters $\overrightarrow{\theta_i}$ can fluctuate about the true value leading to errors associated with their measurements. Hence measured value of $\overrightarrow{\theta_i} = \overrightarrow{\theta_i}^{\mathsf{true}} \pm \Delta\overrightarrow{\theta_i}$, where $\overrightarrow{\theta_i}^{\mathsf{true}}$ is the true value of the parameter and $\Delta\overrightarrow{\theta_i}$ is the error associated with the measurement due to noise, give us information about the parameter $\overrightarrow{\theta_i}$. The measurement errors on $\overrightarrow{\theta_i}$ can be estimated using the semi-analytic parameter estimation technique, Fisher information matrix. From the measurement, we are interested in the posterior probability distribution function for $\overrightarrow{\theta_i}$ given the signal $s(t)$. When we consider flat prior on $\overrightarrow{\theta_i}$ posterior probability distribution is nothing but the likelihood function which is of the form, $p(s|\overrightarrow{\theta_i})$. It can be shown that, for Gaussian noise in the limit of high signal-to-noise ratios, the Fisher information matrix is related to the likelihood distribution function as,

$$p(s|\overrightarrow{\theta_i}) \propto \mathrm{e}^{-\frac{1}{2}(\Gamma_{jk}\Delta\overrightarrow{\theta_j}\Delta\overrightarrow{\theta_k})}, \tag{1.9}$$

. where Γ_{ij} is called the Fisher information matrix [59, 60] defined as follows,

$$\Gamma_{ij} = 2\int_{f_{\mathsf{lower}}}^{f_{\mathsf{upper}}} df \frac{\tilde{h}_i(f)\tilde{h}_j^*(f) + \tilde{h}_j(f)\tilde{h}_i^*(f)}{S_n(f)}, \tag{1.10}$$

where $S_n(f)$ represents the noise power spectral density (PSD) of the detector and $\tilde{h}_i \equiv \partial\tilde{h}(f;\overrightarrow{\theta_i})/\partial\overrightarrow{\theta_i}$ is evaluated at the true value of the parameter $\overrightarrow{\theta_i} = \overrightarrow{\theta_i}^{\mathsf{true}}$. The inverse of the Fisher matrix provides a lower bound on the covariance matrix (Σ_{ij}) through the Cramer-Rao bound and the error (σ_i) on each parameter $\overrightarrow{\theta_i}$ is given by the square root of the diagonal entries of the covariance matrix. That is,

$$\sigma_i = \sqrt{\Sigma_{ii}}. \tag{1.11}$$

The upper and lower cut-off frequencies given in Eq. (1.10), f_{upper} and f_{lower} are chosen according to the sensitivity of the detector configuration which is in consideration.

1.3.2.2 Bayesian inference for parameter estimation and model selection

In the gravitational wave parameter estimation, we would like to address two questions under the framework of Bayesian inference. First question is that, given the GW data, what are the parameters characterizing the source under the assumption of a fixed waveform model. The next question would be that, which is the preferred model among the different models describing the dynamics of the GW source. In this section, we give a brief overview of these methods and how to use them for the parameter estimation and model selection of compact binary described by general relativity. See references [12, 61–63] for a detailed review of gravitational wave parameter estimation methods using Bayesian inference.

To begin with, we introduce a hypothesis $\mathcal{H}$ which is (one of) our assumption(s) about the true waveform model underlying in the data d recorded by the detectors. If $\overrightarrow{\theta_i} = \{\theta_1, \theta_2..\theta_N\}$ is the set of parameters describing the model $\mathcal{H}$, then using Bayes' theorem, one can write,

$$P(\overrightarrow{\theta_i}|\mathcal{H}, d) = \frac{P(\overrightarrow{\theta_i}|\mathcal{H})\, P(d|\mathcal{H}, \overrightarrow{\theta_i})}{P(d|\mathcal{H})}, \tag{1.12}$$

where, the quantity on the left hand side, $P(\overrightarrow{\theta_i}|\mathcal{H}, d)$, is the *posterior probability* of the parameter $\overrightarrow{\theta_i}$, given the data. $P(\overrightarrow{\theta_i}|\mathcal{H})$ is known as the *prior probability* which is our state of knowledge of $\overrightarrow{\theta_i}$ prior to the data being available. The quantity $P(d\,|\overrightarrow{\theta_i}, \mathcal{H})$ is known as the *likelihood function* which is the probability of data given the $\mathcal{H}$ as the underlying model and $\overrightarrow{\theta_i}$ is the true set parameters characterizing the hypothesis. For a

Gaussian stationary noise, the *likelihood function* can be expressed as,

$$P(d|\mathcal{H},\overrightarrow{\theta_i}) \propto \exp\left(-\frac{(\tilde{d}-\tilde{h}|\tilde{d}-\tilde{h})}{2}\right), \tag{1.13}$$

where, $\tilde{d}$ and $\tilde{h}$ are respectively the data and model waveform in frequency domain. The noise weighted inner product $(.|.)$ in the exponent is defined as,

$$(\tilde{d}-\tilde{h}|\tilde{d}-\tilde{h}) = 4\int_{f_{\rm lower}}^{f_{\rm upper}} \frac{(\tilde{d}-\tilde{h})^*(\tilde{d}-\tilde{h})}{S_{\rm n}(\rm f)} df \tag{1.14}$$

where the integration is over a domain between the lower and upper cutoff frequencies of the analysis and the * in the numerator denotes the operation of complex conjugation. The denominator $S_{\rm n}(\rm f)$ is the one-sided noise power spectral density of the GW interferometer. Further, the term $P(d|\mathcal{H})$ in Eq. (1.12) is known as the *evidence* of the model $\mathcal{H}$, denoted by $\mathcal{Z}$, which can be obtained by the following integral following Eq. (1.12),

$$\mathcal{Z} = P(d|\mathcal{H}) = \int P(\overrightarrow{\theta_i}|\mathcal{H})\,P(d|\overrightarrow{\theta_i},\mathcal{H})d\overrightarrow{\theta_i}, \tag{1.15}$$

where the integration is over the entire prior domain (or volume) of the multi-dimensional parameter space. Evidence, also known as the marginalized likelihood, is a measure of how well the data d is in agreement with the model $\mathcal{H}$ within the prior domain of the parameter space.

For a multi-dimensional parameter space $\overrightarrow{\theta_i} = \{\theta_1,\theta_2,...\theta_N\}$, the *posterior probability distribution* for a given parameter θ_1 is calculated by marginalizing the multi-dimensional posterior distribution over the remaining parameters,

$$P(\theta_1|d,\mathcal{H}) = \int P(\overrightarrow{\theta_i}|d,\mathcal{H})\,d\theta_2,...d\theta_N. \tag{1.16}$$

The mean μ_θ and variance σ_θ for a single parameter θ (*i.e.,* , of a 1-dimensional posterior distribution) can be obtained, respectively, by

$$\mu_\theta = \int_{\theta_{min}}^{\theta_{max}} \theta\,P(\theta|d,\mathcal{H})\,d\theta, \tag{1.17}$$

$$\sigma_\theta^2 = \int_{\theta_{min}}^{\theta_{max}} (\theta-\mu_\theta)^2\,P(\theta|d,\mathcal{H})\,d\theta, \tag{1.18}$$

and the 90% credible intervals are obtained as the shortest interval $(\theta_{\rm left}, \theta_{\rm right})$ which contains 90% of the posterior probability distribution, *i.e.,*

$$\int_{\theta_{\rm left}}^{\theta_{\rm right}} P(\theta|d,\mathcal{H})d\theta \sim 0.9. \tag{1.19}$$

In order to perform a model selection between two competing hypotheses $\mathcal{H}_1$ and $\mathcal{H}_2$, one computes the odds ratio $\mathcal{O}_2^1$ between the two models which is defined as the ratio of the posterior probability of the two models given the data,

$$\mathcal{O}_2^1 = \frac{P(\mathcal{H}_1|d)}{P(\mathcal{H}_2|d)} \tag{1.20}$$

Odds ratio is a useful quantity to express how well the data prefers a given hypothesis $(\mathcal{H}_1)$ over the other $(\mathcal{H}_2)$. When the data d favors the the model $\mathcal{H}_1$ over $\mathcal{H}_2$, then the numerator will be larger and hence an odds ratio will be larger than 1. Using Bayes' theorem, the above expression can be written as

$$\begin{aligned} \mathcal{O}_2^1 &= \frac{P(\mathcal{H}_1)}{P(\mathcal{H}_2)}\frac{P(d|\mathcal{H}_1)}{P(d|\mathcal{H}_2)} \\ &= \frac{P(\mathcal{H}_1)}{P(\mathcal{H}_2)}\frac{\mathcal{Z}_1}{\mathcal{Z}_2} \\ &= \frac{P(\mathcal{H}_1)}{P(\mathcal{H}_2)}\mathcal{B}_2^1 \end{aligned} \tag{1.21}$$

with

$$\mathcal{B}_2^1 = \frac{\mathcal{Z}_1}{\mathcal{Z}_2} \tag{1.22}$$

where $\mathcal{Z}_1$ and $\mathcal{Z}_2$ are the evidences of the models $\mathcal{H}_1$ and $\mathcal{H}_2$ respectively as defined in Eq. (1.15). The quantity $\mathcal{B}_2^1$ is known as Bayes factor of the two models $\mathcal{H}_1$ and $\mathcal{H}_2$. In those cases where there are no strong prior information (*i.e.,* we do not prefer one model over the other a priori), then one generally assumes flat priors (uniform prior) for each model. In such cases, the ratio of priors $\frac{P(\mathcal{H}_1)}{P(\mathcal{H}_2)}$ in above equation will be unity and therefore the odds ratio will be simply equal to the Bayes factor. In such cases Bayes factor $\mathcal{B}_2^1$ is the quantity of most interest for the model selection purposes as it only depends on the data not on data and prior information.

LALInference [12] is a Bayesian inference toolkit available in LIGO Algorithm Library (LAL) which performs parameter estimation and model selection discussed above, for gravitational wave signals. In order to achieve this, *LALInference* makes use of stochastic sampling algorithms such as Nested Sampling [64], Markov Chain Monte Carlo (MCMC) sampling *etc* [65–67] *etc.*

The primary goal of the *LALInference* pipeline is to perform parameter estimation on real GW signals. However, *LALInference* can also be run on simulated signals known as software injections, with known physical parameters, widely used for exploratory studies. This allows one to inject software injections on real data segments (noise) from LIGO-VIRGO runs as well as fake noise which is generated by a random number generator. Further, *LALInference* allows to choose zero-noise realization (zero-noise injections) which ensures that the estimates obtained are free of systematics due to the particular noise realization and hence will have effects only from the parameter space degeneracies and correlations which are more likely related to underlying physics of the GW waveform.

1.4 Towards the detection of gravitational waves

1.4.1 Early efforts: Bar detectors and binary pulsar observations

In early 1960s, Joseph Weber proposed the idea of using resonant bars to detect gravitational waves [68–70]. The basic idea was to capture the vibrations on the solid aluminium cylinders, about 2 meters long and 1 meter in diameter, due to gravitational wave passage at its resonant frequency of about 1660Hz. A piezoelectric crystal was used to convert the resonant vibrations into an electrical signal. Weber demonstrated a method to isolate real signal from noise which was expected to arise from seismic and electromagnetic disturbances to the cylinders and the random thermal motion of the aluminium atoms where he introduced the idea of signal threshold. Even though he reported the detection of GWs at two different locations on earth no other scientist could reproduce the claims made by Weber [68–70].

In the meanwhile, binary pulsar observations by Taylor and Russell Hulse provided strong evidence for the existence of gravitational waves. The study started in 1974 and they continued observing the orbital decay of a binary system, PSR B1913+16, composed of a pulsar in orbit around a neutron star [71, 72]. The rate of shrinkage of the orbit over time was consistent with theoretical predictions which rely on the assumptions of gravitationally dissipating system [73]. For this remarkable discovery, Hulse and Taylor were awarded the Physics Nobel Prize in 1993 [74, 75] and this speed up the developments of laser interferometric gravitational wave detectors.

1.4.2 Interferometric detectors and the first direct detection of gravitational waves

1.4.2.1 Interferometric gravitational wave detectors: working principle

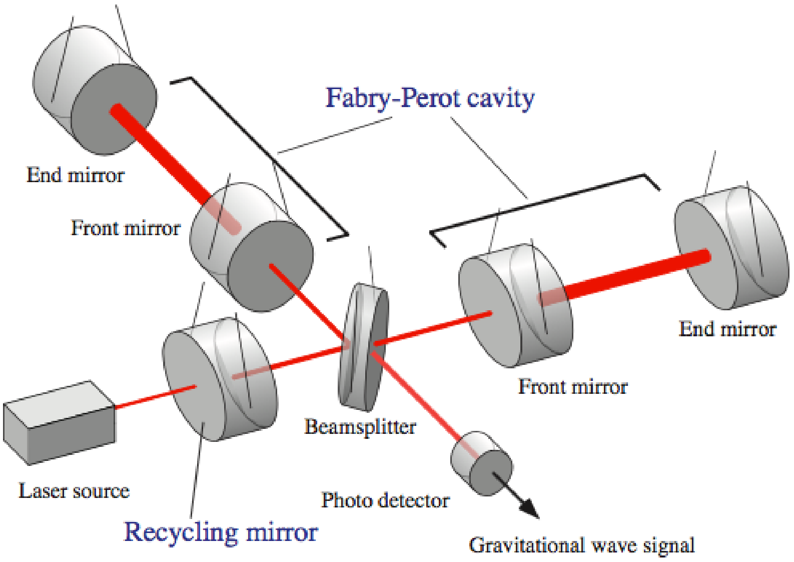

FIGURE 1.2: Demonstration of the basic working principle of laser interferometric gravitational wave detectors [1].

The working principle of interferometric GW detectors is the same as that of a Michelson interferometer. As shown in Fig. 1.2, in a Michelson interferometer a beam of light falls on a half-reflecting surface, called the beam splitter. The light splits in to two, one part is transmitted and the other part is reflected to the perpendicular direction of initial propagation as the beam splitter is oriented at 45 degrees with respect to the propagation of the light ray. Light rays on both the directions travel till the end mirrors, which is kept at equidistant from the beamsplitter, and reflect back to the beam spitter. At the beam splitter the two beams recombine to produce minimum amplitude (destructive interference) or maximum amplitude (constructive interference) depending upon the phase difference between the two rays.

If a plane GW passes transverse to the interferometer, one arm stretches and the other squeezes depending upon the polarization of the incoming wave and relative orientation of the detector with respect to the source. This differential motion of the freely suspended end mirrors at each arm of the detector lead to a change in the interference pattern observed, and this leads to variation in the photo diode output. In summary, if there is no GW passes through the detector (interferometer) arm lengths remain unaltered hence the phase shift of the electromagnetic wave (high power lasers) will not change. In this case, the time difference $\Delta\tau = \tau_x - \tau_y = 0$, that is both the rays take equal time and the photodiode registers no signal if both rays were out of phase (destructive interference). In the presence of a plane GW passing perpendicular to the detector, there will be a time difference $\Delta\tau = \tau_x - \tau_y$, equal to $\frac{2L}{c}\,h(t)$, unlike the previous case. Using the simple relation connecting the time delay to the phase shift, $\Delta\phi = \frac{2\pi}{\lambda}\Delta\tau$ (where λ is the wavelength of the light used), we can write the above equation in the form as $\Delta\phi = \frac{2\pi}{\lambda}\,\frac{2L}{c}\,h(t)$ and this phase shift will be registered in the photodetector [76].

As we discussed in Sec. 1.1, the GW strain amplitude from a typical astrophysical source of gravitational waves is $h(t) \sim 10^{-21}$. The question then one can ask is how to achieve this sensitivity. Simple way would be to increase the arm length, L. This is not easy to realise it in practice due to various reasons. But by introducing optical cavities (indicated as Fabry-Perot cavities in Fig. 1.2) and bouncing the laser beam several times inside this optical cavity the optical path length can be increased without altering the physical arm length [2]. The noise due to photon count in the detector is proportional to the intensity (number of photons) of the radiation used. Instead of generating very high power lasers, which again is not practical, power recycling mirrors are used in current detectors [3]. These two will thereby help improve the sensitivity by a factor of almost $\sim 10^6$!

---

[2] For current second generation detectors the arm length is increased from a few kilo meters (4km) to a few thousand kilo meters (1120 km) by bouncing the beam inside the cavity for a few hundred times (~ 300)

[3] The input laser power of a few hundred Watt (200W) is amplified to a few thousand Watt (750kW)

1.4.2.2 Noise sources for interferometric gravitational wave detectors

Another big challenge to construct the interferometric detectors and hence to detect a gravitational wave signal was to control all possible noises at different frequency bands and improve the sensitivity of the detector. The fundamental noise sources to the interferometric GW detectors are from Newtonian noise (or gravity gradient noise dominated at lower frequencies, < 10Hz), thermal noise (present mostly at intermediate frequency region, few hundred Hertz) and the quantum noise which is a combination of photon shot noise (appear at high frequencies) and radiation pressure noise (which appears at lower frequencies). Further more there are technical noise sources those can be controlled by different technological advances.

1.4.3 Direct detection of gravitational waves

Over the past years ground based interferometric detectors were proposed with potential sensitivity in the frequency range 20Hz to 10kHz targeting gravitational waves of astrophysical origin. The first generation Laser Interferometric Gravitational Observatories (LIGO) were functioning until 2010, though there was no gravitational wave detection [77]. After installing the advanced LIGO detectors [78], the first observing run started operation in 2015 September with enhanced sensitivity compared to the initial detectors.

Detection of GWs is a hard task as one needs most sensitive experimental setups which can achieve an accuracy of the order of $\sim 10^{-21}$ as we discussed. The first direct detection of the gravitational waves from a binary black hole merger (named as GW150914) event happened on 14 September 2015 at 09:50:45 UTC, in the two second generation LIGO detectors one in Hanford, and another in Livingston within a time difference of $6.9^{+0.5}_{-0.4}$ milli seconds [79]. The GW150914 signal was produced by a binary black hole system with masses $\sim 35M_{\odot}$ and $\sim 29M_{\odot}$ at a luminosity distance of ~ 410Mpc. The signal lasted for 0.2s in the detector band with a frequency chirp of 35Hz to 250 Hz. This detection happened as a results of huge effort from scientists working in many different areas including theoretical modelling of astrophysical sources, parameter estimation, detector characterization etc. For this remarkable discovery Rainer Weiss Barry C. Barish and Kip S. Thorne awarded the Physics Nobel prize in 2017. In Fig. 1.3, we show the GW form from GW150914 and it describes the inspiral-merger-ringdown regimes. Notice that the numerical relativity model in Fig. 1.3

matches with the reconstructed template within the statistical uncertainty and this statistical uncertainty in the estimated parameters is shown in shaded region.

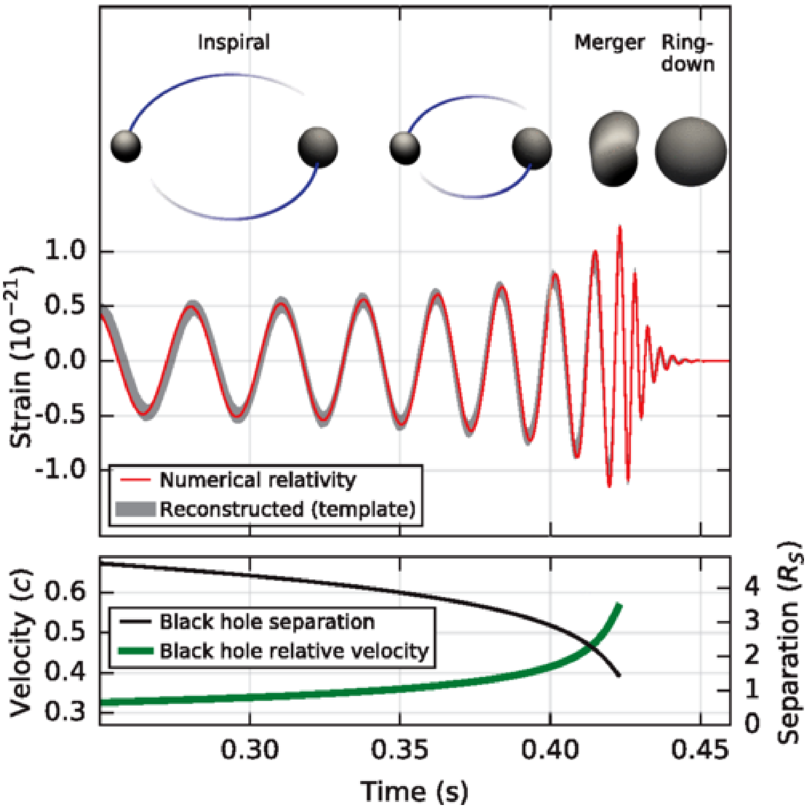

FIGURE 1.3: Observed gravitational wave signal from GW150914 [2].

After this discovery, the LIGO-VIRGO (joined the network of two LIGO detectors on 1st August 2017) detectors announced another nine binary black hole mergers and one binary neutron star merger during their first and second observational runsThe one year long third observation run of the ground based gravitational wave detectors with improved sensitivity started on April 2019.

1.5 Implications of gravitational wave detection to astrophysics, fundamental physics and cosmology

The direct detection of GWs by LIGO and Virgo detectors had profound impact on our understanding of astrophysics, fundamental physics and cosmology. Here we give a quick overview of what we learned from these observations.

1.5.1 Probing the strong field gravity

1.5.1.1 Tests of consistency with GR

We discuss two methods used to test the consistency of the gravitational wave signals with GR. These model independent null tests were carried out to see if the GR waveform model indeed matches with the observed signal.

Residual test: Residual test relies on checking the consistency of residual obtained by subtracting the best fit waveform from the data and see if is is in agreement with the instrumental noises. One obtain the maximum aposteriori values or the MAP values characterizing the binary signal from parameter estimation (for the LIGO-VIRGO analysis *LALInference* is used for this) and use this to reconstruct the binary waveform. After removing the best fit from the data, analyse the residual using a transient search algorithm (for the LIGO-VIRGO analysis Bayeswave [80] is used for this). There will not be an excess power left if the data and reconstructed signal are consistent with each other. The transient algorithm compares the signal-to-noise (measure the excess power in the data) and signal-to-noise (measures the coherence of excess power in various detectors) Bayes' factors 1.3 and use this to make statistically meaningful statements about the available residual. The studies carried till now on the detected events, including the first GW detection [81] and the results from the first BBH catalog [82], the residual obtained found to be statistically indistinguishable from the instrumental noise.

Inspiral-merger-ringdown consistency test: Recently, Ghosh et al. proposed a method [83, 84] to study the consistency of the inspiral-merger-ringdown dynamics of a binary black hole system to the one predicted by general relativity. The idea here is to infer the mass and spin parameters of the merger remnant from the post-inspiral part of the gravitational wave signal and ask if this is consistent with the same as inferred from the inspiral part of the gravitational wave signal (using the numerical fitting formula given in [85]). This method allows one to quantify how close the observed high mass compact binary mergers are to the mergers of binary black holes in general relativity [2, 15].

1.5.1.2 Tests related to the source dynamics/Tests of gravity from GW generation

Constraining the parametrized deviations from general relativistic inspiral-merger-ringdown waveform models: If the true theory is not GR there will be a change in the dynamics of the source and will also reflect in the gravitational waveform models which assume GR as the correct theory. The waveform models which describe the evolution of the binary system contain coefficients which are determined either analytically or numerically. These inspiral-merger-ringdown coefficients have particular functional dependence on the intrinsic and extrinsic parameters of the binary system if GR is the correct theory. By introducing parametrized deviations to these coefficients one can test the true nature of the theory [86, 86–91]. These tests have been carried out for all the detected binary black hole systems so far and there was no deviation found within the allowed statistical errors [15, 79, 92–94].

Mapping parametrized PN deviation parameters to alternative gravity models: Measurements of deviations of post-Newtonian coefficients at different PN orders can be used to constrain different alternative theories. There are scalar tensor theories of gravity, like Brans-Dicke theory, which allow dipole radiation unlike GR.One can put strong constraints on the free parameters corresponding to the dipole radiation of the alternative theories of gravity from GW observations [95]. From the binary neutron star inspiral observed in the second observing run of LIGO-VIRGO detectors, GW170817, we got constraints on the dipole radiation coefficient assuming the Brans-Dicke scalar field theory and which is the first of this kind though it is weaker compared to the ones from pulsar timing measurements [96].

1.5.1.3 Tests of gravity from GW propagation

Constraining the parameters characterizing the modified dispersion relations: GW propagation in GR is non-dispersive (velocity of propagation is independent of frequency) and the graviton is massless with a corresponding infinite Compton wavelength. There are alternative theories of gravity predictions for GWs with dispersion where the local Lorentz in-variance is not respected [97]. By considering modified dispersion relations, $E^2 = p^2\,c^2 + \mathcal{A}\,p^{\alpha}\,c^{\alpha}$, and obtaining bounds on these modified dispersion parameters $\mathcal{A}$ and α (here $\mathcal{A}$ is the dispersion amplitude and has dimension of $[\mathsf{Energy}]^{2-\alpha}$ and α is a dimensionless constant) one might be able to set constraints on the alternative theories of gravity models [98–101]. As shown in Ref. [98, 102], one can use GW observations to get possible constraints on the modified dispersion parameters. The first bound on the Compton wavelength (which is a finite value for any massive graviton theory) from GW observations of a BBH signal is $\lambda_g > 10^{13}\mathsf{km}$ [92] and this has been extended to more generic cases in subsequent analysis [15, 82, 103]. This bounds on Compton wavelength will translates to graviton mass, $m_g \leq 5 \times 10^{-23}\mathsf{eV}/\mathsf{c}^2$, and this result is a slightly better compared to the solar system constraints [82].

1.5.2 Binary neutron star detection and gravitational wave multi-messenger astronomy

The merger of compact binary systems with one of the component being NSs expected to emit photons and neutrinos with GWs. The LIGO-Virgo detector network observed a gravitational-wave signal which is consistent with a binary neutron star (BNS) system [104]. This was the loudest inspiral signal ever detected. The BNS detection allowed the possibility of electromagnetic and neutrino follow-ups and a large number of scientists working for different instruments participated in the effort.

A binary neutron star merger is an expected progenitor for short GRBs, which is a beamed emission of isotropic equivalent energy of almost $\sim 10^{49} - 10^{51}$ erg. After ~ 1.7s from the detection of GW170817 [104] an associated gamma-ray-burst, GRB 170817A, detected by Fermi-GBM and this indeed confirms the first link between short-GRBs and BNS merger. Subsequently, an optical transient (AT 2017gfo), UV, optical, IR, X-ray and radio radiations were detected after few hours to days of GRB observation from the extended search in different frequency ranges from various observatories. Also lead to the identification of source location in the galaxy NGC 4993 which is situated approximately at a luminosity distance of 40Mpc [105].

Associated with a short-GRB emission, there expected to be energy emission through neutrinos and this observations could help us understanding the nature of hadronic matter formed during such relativistic phenomena [106]. The ANTARES [107], IceCube [108], and Pierre Auger Observatories [109] could carry out an extensive high energy neutrino search and no evidence for neutrinos found (in the ± 500s of data). This null results was expected if the short GRB emission is off axis to the observer [110].

1.5.2.1 Measuring the Hubble constant from gravitational wave standard siren

It was proposed in Ref. [111] that by combining the luminosity distance to the source inferred purely from the gravitational-wave signal with the recession velocity inferred from measurements of the redshift using electromagnetic data can be used to obtain the Hubble constant, which is measure of the expansion rate of the universe. This proposed idea was studied in the context of compact binary mergers observable by ground based GW detectors in Ref. [112] and the authors concluded that, as the number of such detections (where both EM and GW informations obtained from the same source) the measurement accuracy can be improved dramatically [112]. From the GW luminosity distance estimation of $43.8^{+2.9}_{-6.9}$Mpc and the host galaxy identification NGC 4993 of GW170817 the Hubble constant is determined as $70.0^{+12.0}_{-8.0}\mathrm{km/sMpc}$ at 68% credible interval. This result is completely consistent with other existing measurements based on the Planck observations [113] of temperature and polarization anisotropies of the cosmic microwave background (CMB) radiation and the SH0ES (Supernovae, H0, for the Equation of State of dark energy) team of HST (Hubble Space Telescope) [114].

1.5.2.2 Extreme matter physics

Neutron stars are interesting astrophysical sources to study the dense nuclear matter as any of the current terrestrial experiments fail to reach such high dense regions. The details about the matter inside a star are encoded in the equation of state, which describes how the pressure of the star is related to its density. From the accurate modelling of the equation of state we can derive the mass-radius relations for the star which can be used to calculate macroscopic properties such as the multipole moment structure and the tidal deformability parameter of the system. On the other hand, one can measure the mass, radius, moment of inertia, tidal deformability parameter (etc) from observations and understand the nature of equation of state of the star [115]. The gravitational wave data contain informations such as the tidal deformability and the spin-induced multipole moments of the source, using accurate parameter estimation techniques and prior knowledge about such physical effects one can infer those and can be used to constrain different equation of state parameters. As the NS is found to be slowly spinning the spin-induced effects are less important compared to the tidal deformation. The first detection of GWs from BNS merger with EM counter parts allow us to investigate the properties of the nuclear matter in a great detail. For example, in

Ref. [104] the preliminary estimates on the component masses and the tidal deformability are given. A more detailed study is carried out to construct the mass-radius relation for a NS system from the GW observations of tidal deformability parameter is in Ref. [116]. This has been extended by considering astrophysically motivated prior on mass and spin of the NS can be found in Ref. [117]. Measured values of neutron star radii are $R_1 = 10.8^{+2.0}_{-1.7} km$ ($R_1 = 11.9^{1.4}_{1.4}$) for the heavier star and $R_2 = 10.7^{+2.1}_{-1.5} km$ ($R_2 = 11.9^{1.4}_{1.4}$) for the lighter star within the 90% credible interval (with the assumption that the maximum mass allowed for the NS is less than $1.97 M_{\odot}$). These measurements can be translated to the the equation of state parameter, and the pressure at twice the nuclear density is bounded as $p(\rho_{nuc}) = 3.5^{+2.7}_{-1.7} \times 10^{34} dyn/cm^2$ with 90% statistical confidence [117].

1.5.2.3 Constraints on the number of space time dimensions

By a comparison between the distance measurements from GW and EM observations we can constrain the spacetime dimensions. In many of the higher dimensional theories, there are predictions for damping of the waveform due to gravitational leakage into large extra dimensions [118]. This leakage in to extra dimensions will be reflected in the way GW amplitude scale with the luminosity dustance [93, 119]. By constructing a phenomenological ansatz for the GW strain amplitude, constraints obtained on the number of extra dimensions (D=4 in GR) and the screening length (again a characteristic length scale beyond which the gravity assumed to leak in to extra dimensions) from the observed luminosity distance from GW170817 and associated distance measure from the EM observations of the same source [93, 119].

1.5.2.4 Fundamental physics and other astrophysical implications

The observed time offset between the electromagnetic and gravitational waves can be used constrain on the fractional speed difference between gravitational and electromagnetic waves. For example, in the case of GW170817 and GRB170817A the time lag was 1.74 ± 0.05s and this translate to a fractional speed difference of $-3 \times 10^{-15} \leq \frac{\Delta v}{v_{\rm EM}} \leq 7 \times 10^{-16}$. From the observed temporal delay, the inferred distance to the source and the expected emission difference (need more number of detections to disentangle the emission time difference from the relative propagation time for which we need complete understanding of the emission mechanisms) we can also perform other tests such as tests of equivalence principle and tests for Lorentz violations [120]. Most importantly the combined information from a GW and EM from the same source, similar to the case with GW170817 and GRB170817A, we will be able to better understand the short GRB physics and the properties of neutron star EOS [120].

1.6 Future gravitational wave detectors

As we pointed out earlier the advanced LIGO and advanced VIRGO detectors started the third-observation runs and will be continued till August 2020 and the KAGRA [121] detector will join in the later part. LIGO-India is a planned second generation detector placed in India as a part of world wide network of LIGO detectors expected to be operational by ~ 2025 [122]. Adding this to the existing LIGO-VIRGO-KAGRA detector network is expected to increase the detection rate, by increasing the sensitivity and duty cycle of the network will lead to increased detection confidence, better identification of parameters, improved sky localization and so on. Three up-gradations of advanced LIGO are A_+ [123, 124], LIGO Voyager [123] and Cosmic Explorer [125]. Though A_+ and LIGO Voyager are proposed to be installed at the same site as LIGO, Cosmic Explorer is a stand alone project at a different location with ten times more sensitivity than that of advanced LIGO and is expected to be commissioned by 2035 [125] with a low frequency cut-off down to 5 Hz . Further more, Einstein Telescope is another proposed third-generation underground detector with sensitivity comparable to that of LIGO Cosmic Explorer with maximum achievable lower cut-off frequency on earth (~ 1Hz).

The sensitivity of ground-based gravitational wave detectors at lower frequencies is limited by the seismic noise [126, 127]. In order to overcome this and to extend the gravitational wave frequency spectrum to even lower frequency regions we need detectors which operate at frequencies less than 1 Hz [7, 128–131]. The space-based gravitational wave detectors, such as Laser Interferometric Space Antenna (LISA) [130, 132, 133], DECi-hertz Interferometer Gravitational wave Observatory(DECIGO) [7, 131, 134, 135] and Big Bang Observer (BBO) [128, 136], will have the capability to probe gravitational wave frequencies from a few milli-Hz to tens of Hz. Among these, the LISA mission is already funded and is expected to be operational by 2034 after successfully demonstrating some of the key technologies it will use, through the LISA Pathfinder mission [130, 132, 133] which was launched in December 2015.

The Japanese DECIGO mission is designed to bridge the gap between terrestrial GW detectors and LISA and is expected to operate in the deci-Hz band [7, 131, 134, 135]. Though the DECIGO configuration was initially designed to probe signatures of the early universe including cosmic acceleration and gravitational wave background from inflation [134], one can also look for intermediate-mass black hole binaries with masses of the order of a few (hundred) thousand solar masses [137], along with binary neutron stars and stellar-mass binary black holes [6, 138]. Currently, the DECIGO configuration is a proposal whose science potential is being assessed.

Figure 1.4 show the noise spectral densities for different ground and space-based gravitational wave detectors. Right panel of the same figure shows the expected signal to noise ratios for a representative system in each band as a function of the total mass of the system.

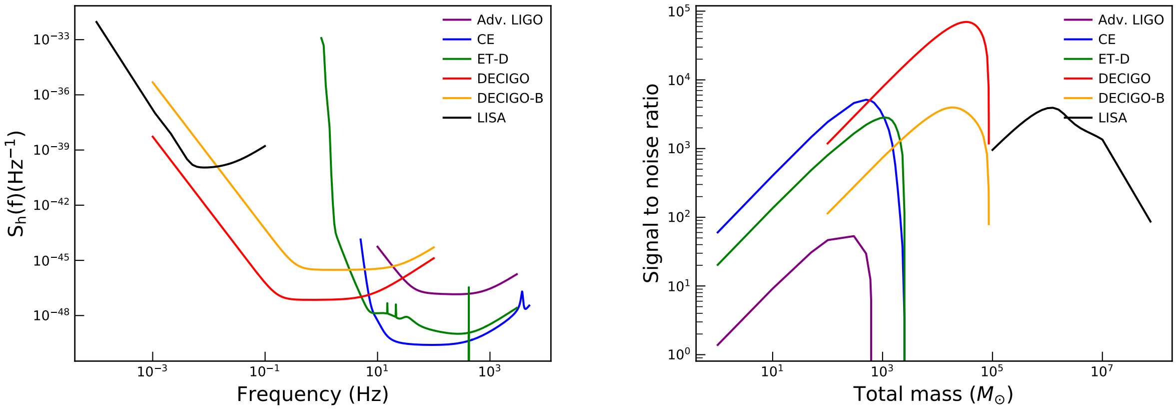

FIGURE 1.4: Noise power spectral densities for various ground and space-based gravitational detectors. Adv. LIGO [3] (purple), Cosmic Explorer [4, 5] (CE, blue), Einstein Telescope [5] (ET-D, green), DECi-Hertz Gravitational wave observatory [6, 7] (DECIGO, red and orange for two different configurations) and Laser Interferometric Space Antenna [8] (LISA, black) corresponding SNRs are given in the right panel. In order to calculate the SNR we choose binaries optimally oriented at 1Gpc and the total mass ranges varies according to the detector sensitivities with a mass ratio of 2.

The combined information from different ground and space-based detectors can be used to improve the parameter estimation accuracy [139–141]. For example, early inspiral of stellar mass binary black hole mergers like GW150914 will be detectable in the LISA band and can be used to give alerts to ground based detectors and EM partner groups [142]. In a similar way, information from the ground-based detections will help to reduce the threshold SNR for space-based detectors [143]. The impact of *multi-band astronomy* has been studied in different contexts [6, 7, 144–146]. In [144], it is shown that the constraints on the dipole radiation can be improved by six orders of magnitude by the joint observations using advanced LIGO and LISA detectors. This has been extended to a more general case by considering the parameterized tests of GR and applications to parity-violating gravity, various space-borne GW detector combinations with Cosmic Explorer and space-borne detectors [145] such as TianQin [147], LISA [146], B-DECIGO [7] and DECIGO [6].

.

1.7 Topic of the thesis

Recent detections of binary black hole mergers by advanced LIGO and advanced VIRGO interferometers [148], confirm that black holes (BHs) are no longer just elegant mathematical entities, but a physical reality [2, 10, 14, 79]. Now we know that BHs do exist in nature, can form a binary BH system and merge emitting GWs to form a single BH. The detected signals show excellent agreement with the numerical relativity model of merger of two Kerr black holes shown in Fig. 1.3, though one can not completely rule out the possibility of any alternatives to black holes (and neutron stars). One of the important questions, from a fundamental physics view point, is whether we can confidently distinguish the mergers of BBHs from that of binaries comprised of exotic compact objects such as gravastars [149] , boson stars [150] etc, which may mimic many features of a BBH merger (see also [151, 152] for reviews on possible BH mimickers and their GW signatures). Studying compact objects composed of exotic (unknown) matter may help us answer many fundamental physics questions including the strong field tests of gravity and to propose new theories, physics beyond standard model, quantifying the existence of horizon and related quantum phenomena, understanding the exact physical nature of cold dark matter (or existence of axions or any other such particle) and obtain the correct model for the inflation. Electromagnetic and gravitational wave signatures of such objects, give us evidence for the existence of such objects, if they exists.

In this thesis, we propose a novel method to test the black hole nature of compact objects using gravitational wave observations. This test relies on measuring the spin-induced multipole moment coefficients of the object, which arise due to the spinning motion of the object and explicitly appear in the PN waveform. We give a brief introduction to exotic compact objects in Chapter 2, describe this method in Chapter 3 and in Chapter 4, we develop a Bayesian inference based infrastructure to perform this analysis on the real gravitational wave events and perform the test on two of the detected events GW151226 and GW170608. In Chapter 5 we discuss the possible applications of the test in the context of upcoming GW detectors.

Chapter 2

Black hole mimickers and tests of black hole nature

2.1 Introduction

The name *black hole mimickers* broadly refers to any astrophysical object which can potentially mimic the observational properties of black holes. These would also include compact objects with matter which are described by equations of state or fields that are 'exotic' and hence referred to as exotic compact objects. Hence throughout the chapter, we will use the words *black hole mimickers* and *exotic compact objects* interchangeably.

In this chapter, we aim to give a general introduction to black hole mimickers (exotic compact objects) in Sec. 2.2, examples for different black hole mimicker models are given in Sec. 2.3, different ways of testing the nature of compact objects using gravitational and electromagnetic wave observations (Sec. 2.4) and we conclude by introducing a new test which can be used to distinguish black holes from black hole mimickers (Sec. 2.5) which forms the basis for this thesis.

2.2 Compact objects: 'conventional' and 'exotic'

Compact objects: Death of a star is predominantly determined by its initial mass, according to our current knowledge of stellar evolution. A compact object is formed once the nuclear fuel, which keeps the star in equilibrium, is completely consumed or burned. Depending upon the nature of the force which balances gravity after this stage, a star may end up as a white dwarf, neutron star or a black hole. In the case of white dwarfs, it is the electron degeneracy pressure that balances gravity, neutron degeneracy pressure balances gravity in the case of neutron stars. When the core of the collapsing star is so heavy that none of the above can balance gravity, the star ends up as a black hole. Compactness is a measure of how closely the matter is packed in a compact object and is defined as $C \sim \mathsf{M}/\mathsf{R}$, where M and R are the mass and radius of the star.

White dwarfs are comparatively less compact compared to neutron stars with a maximum allowed mass of $1.4 M_{\odot}$ (highest observational value found to be $\sim 1.33 M_{\odot}$ [153]) and radius a few thousand km. Properties of matter constituting neutron stars are still unknown at highly dense regions. The maximum mass observed for a neutron star is $\sim 2.02 M_{\odot}$ [154], though there are theoretical models for neutron star with larger masses. Usually, the compactness of neutron star lies between $\sim 0.001 - 0.2$ [155] depending upon the internal structure. Another important property is the high magnetic field which may be $\sim 10^{15}$Gauss for a neutron star, usually called magnetar.

Black holes: Black holes are characterized by a central singularity (where the physics is not known) which is covered by a surface of infinite redshift, called event horizon which acts as a one-way membrane: things can fall in but cannot come out! The event horizon is a unique property of BHs hence this can be used to distinguish BHs from alternatives to BHs. In general relativity, all of the black hole's multipole moments are completely described by its mass and spin according to the "no-hair" conjecture [156–161] (review of BHs can be found here [162, 163]). Most of the probes for BH nature focus on addressing the question whether the multipole moments of the BH nature are solely characterized by its mass and spin or are there additional fields which play a role (these fields are referred to as 'hairs').

Depending upon the mass range, black holes may be broadly classified into four categories; sub-solar mass BHs, stellar-mass BHs, intermediate-mass BHs, and supermassive BHs. Notice that the formation mechanism in each case could be different and may not follow the usual stellar evolution channels described above. Sub-solar mass BHs are BHs with masses less than the mass of the sun, $M < 1 M_{\odot}$. One of the possibilities of sub-solar mass BH formation suggested is of primordial origin [164]. Also, there are studies were the sub-solar mass BHs are expected to contribute to a fraction of the total dark matter content of the universe [165]. Gravitational-wave searches for sub-solar mass BHs are in progress and yielded no candidate found to date from first and second observational runs of ground-based detectors [166].

Stellar-mass BHs are of masses from a few solar mass up to 100s of solar masses. The masses of detected compact binary systems through gravitational waves, in the source frame, roughly range between $\sim 7 - 80 M_{\odot}$ [167]. The strongest observational evidence for their existence has come from the direct GW observations using ground-based detectors [2, 10, 11, 14, 15, 79, 103, 167]. Their existence was indirectly confirmed by various EM observations in the last three-four decades, mainly from X-ray binaries in our galaxy [168].

Intermediate-mass BHs are predicted to have masses of the order of $\sim 10^2 - 10^5 M_{\odot}$ and their formation mechanism is currently not known completely [169, 170]. Indirect evidence for IMBHs from electromagnetic observations is promising and also motivate new proposals for gravitational wave detectors in the corresponding frequency range. The ultra-luminous X-ray source HLX-1 hosted by galaxy ESO 243-49 is believed to be an intermediate-mass BH of mass $\sim 500 M_{\odot}$ [171]. Another observational evidence for intermediate-mass BH came from the X-ray quasi-periodic oscillations of M82 X-1, which is the brightest X-ray source in the galaxy M82 [172]. In Ref. [173], authors demonstrated the existence of an electromagnetically dark black hole in the globular cluster 47 Tucanae with mass $\sim 2300 M_{\odot}$ through the observed pulsar acceleration rates together with N-body simulations. Recent studies [172] support the evidence for intermediate-mass BHs and motivates them to develop set-ups to probe the number of such systems to know their formation and evolution.

Supermassive BHs are even more massive and the masses are assumed to be of the order of $10^5 - 10^{10} M_{\odot}$. Various electromagnetic observations tell us that there exists a supermassive black hole of mass $\sim 10^5 - 10^{10} M_{\odot}$ at the center of each galaxy [174–176]. Sagittarius A^* is the closest supermassive black hole situated at the center of our Milky Way galaxy with a mass of $\sim 4 \times 10^6 M_{\odot}$ [177, 178]. Observational evidence for supermassive black holes (SMBHs) also include the quasar observations from the Sloan Digital Sky Survey [179], a recent study which combined information from the Sloan Digital Sky Survey, the Two Micron All Sky Survey, and the Wide-field Infrared Survey Explorer [180] and the quasar (ULAS J1120+0641) with mass $\sim 2 \times 10^9 M_{\odot}$ at a redshift of ~ 7.085 identified by the United Kingdom Infrared Telescope (UKIRT) Infrared Deep Sky Survey (UKIDSS) Eighth Data Release in 2010 [181], to name a few. The formation mechanism of such systems is still not completely understood, though they are proposed to have formed through galaxy mergers [175]. The first-ever image of a supermassive black hole situated at the center of the elliptic galaxy M87 has been produced by the Event Horizon Telescope (EHT). This radio source is situated around 16 Mpc away with a mass of $\sim 6.5 \times 10^9 M_\odot$ [176].

2.3 Models for black hole mimickers

Black hole mimickers: As the name indicates black hole mimickers are compact objects, which can mimic some of the properties of black holes including mass and spin. We will review below some of the prime candidates for BH mimickers and observational probes for their existence. We consider two types of black hole mimickers. One where there are exotic matter or fields present (Sec. 2.3.1) and the other which are parametrized deformations of black hole (Sec. 2.3.2).

2.3.1 Exotic compact object models

2.3.1.1 Boson stars

Boson stars are compact objects formed by equilibrium configurations of a scalar field tied up with its own gravity and the gravitational collapse of such a system is prohibited by Heisenberg uncertainty principle [182]. Boson stars have been introduced in the literature at different contexts, as dark matter candidates(for example in Ref. [183]) and models for black hole mimickers [184–186] *etc.* Depending upon the nature of the scalar field coupling there are mainly three types of boson stars such as mini (minimal) boson stars [187], solitonic boson [188] stars and massive boson stars [189] as discussed in Ref. [190]. The minimum mass of the boson particle will differ in each of these cases and roughly vary from $\sim 10^{-11} eV$ to $\sim 10^2 GeV$. There have been several works on rotating boson stars [191, 192] (boson stars with spin angular momenta) including the important work of Ryan et. al. [193] which we discuss later in this chapter. The first attempt to give a boson star model in Brans-Dicke theory, one of the alternative theories of gravity, was done in [194]. This detailed study also provides a comparison between boson star solutions in general relativity and Bans Dicke theory for different scalar field couplings. This has been extended to general scalar-tensor theories in Ref. [195]. The existence of equilibrium boson star solutions in the context of gravity theories with dilaton is studied in Ref. [196].

Accurate modelling of compact binary systems is very important for GW detection as well as parameter estimation studies. In this context, it is also important to develop waveform models for compact binaries composed of black hole mimickers.

The dynamics and GW signatures of the inspiral of binaries consisting of non-rotating solitonic BSs with fixed compactness are studied in Ref. [197] and the numerical simulations performed by the authors found that the merger remnant can either be a non-rotating BS or a BH. A recent study in Ref. [197] extended the work of Ref. [198] for rotating solitonic BSs also considering different compactness for the stars. The late-inspiral waveform of the colliding solitonic BS system found to be different from that of BH unless the initial compactness of the star is close to the BH value. Furthermore, the peak GW frequency corresponding to a binary BS merger is shown to be shifted away from that of BNS and BBH mergers. The late ringdown of such mergers is expected to exhibit physical features such as echoes [199]. Similarly, three-dimensional head-on collisions and the distinguishable features in the ringdown radiation compared to that of BBH mergers of mini boson stars are studied by numerically evolving the field equations [200].

2.3.1.2 Gravastars

Gravitational condensate stars (gravastars, GS) are a class of compact stars proposed as an alternative to black holes (BHs) [149]. In Ref. [149] authors introduce a five-layer model for a gravastar with thermodynamic stability. In general, a GS model consists of an interior de-Sitter region and an exterior Schwarzschild region. The de-Sitter space-time models a star with negative pressure. The thin shell gravastar model with a three-layer structure was first proposed by Visser et.al. [201] which is a simpler model than the original five-layer structure. In other words, the finite thickness wall in the five-layer model which differentiates the two spacetimes is replaced by an infinitesimally thin wall in the case of thin shell GS models.

2.3.2 Parametric models of non-Kerr geometry

2.3.2.1 Bumpy black hole models

Black holes have always been test beds for strong-field gravity (See, for example, this review article [202]). The Kerr black hole spacetime is completely specified by its mass and spin. Motivated by the fact that the null tests of black hole nature can be carried out through constraining the multipolar deviations from Kerr black holes, Collins and Hughes introduced a new set of objects, non-rotating BHs with a small 'bump' on them, called bumpy black holes [203]. The bumpy black hole space-time approaches the corresponding black hole limit as the *bumpiness* vanishes hence the multipolar structure of these class of objects is very close to BHs. The main issues with this model were resolved in [204] where the authors provided a more general framework for bumpy black holes with arbitrary spins. The accumulated orbital phase will carry information about the non-Kerrness of the space-time and this could be measured through experiments. Here the physical mechanisms by which the bumps are created on a BH geometry could be due to the presence of some unknown matter. In Ref. [205] authors introduced waveform models for deformed bumpy black holes as an extension of their numerical kludge waveform models for extreme mass ratio inspirals [206].

2.3.2.2 Quasi-Kerr BHs

The gravitational waves emitted from a binary system containing a massive central body and less massive object orbiting will carry information about the space-time of the central object [207]. If the central object is not a Kerr black hole the measured quadrupole moment parameter of the system may not be a function of only the mass and spin of the system. In the quasi-Kerr framework, the quadrupole moment of the central object is not necessarily that of a Kerr black hole. The deviation parameter characterizes the non-Kerr nature of the space-time and it takes zero value for Kerr black holes. The idea was introduced in [208] and extended studies were carried in Refs. [209–211].

2.3.2.3 Kerr black holes with scalar hair

In Ref. [212] authors obtained a class of solutions of Einstein-Klein Gordon equations. These asymptotically flat regular black hole solutions can be interpolated to obtain boson stars as a limiting case. Equilibrium configurations of this set of solutions are named as Kerr black holes with scalar hair. These proposed models were extended by many authors in different ways [213–216].

2.4 Model independent null tests and black hole nature of the object

Modelling mergers of these exotic objects is a hard problem and their direct deployment for data analysis is not likely to happen in the near future. So a more pragmatic approach would be to devise tests that are generic and model-independent and are based on our solid understanding of the binary black hole dynamics. *One of the efficient methods to probe the presence of exotic compact objects is to understand different ways in which these objects would modify the properties of black holes and study how these modifications would affect the gravitational waveforms from binary black holes. Ideally, one would like to have a parametrized deformation of the binary black hole waveform in GR in terms of some free parameters which characterize these exotic objects. It is important to devolep methods to measure these parameters through various means and put constraints on the black hole mimcker models.* These tests are often referred to as “null tests" as the free parameters are zero for binary black holes. In order to develop such model-independent null tests of black hole mimickers, it is important to identify those properties which are unique to black holes and trace their imprints on the gravitational waveform so that we can measure them from observations.

One of the characteristic properties of black holes in the general theory of relativity is related to the “no-hair” conjecture, which says that all the multipole moments of a Kerr black hole are completely specified by its mass and spin. This means that, it is always possible to relate the ℓ^{th} multipole of the Kerr black hole to the mass (M) and the dimensionless spin parameter ($\chi = S/M^2$) as, $M_\ell + \mathrm{i}\, S_\ell = M^{\ell+1}(\mathrm{i}\,\chi)^\ell$ [156–161]. Here M_ℓ and S_ℓ are the mass- and the current-type multipole moments, respectively. This property leads to several observational predictions unique to a black hole which are built-in to the gravitational waveform facilitating tests of black hole nature, some of which are discussed below.

Even though our main focus is on tests based on gravitational observations, we also like to mention about the possible tests of BH nature using electromagnetic observations. As demonstrated in a series of papers the *X-ray observations* of reflection spectra from the accretion disc of black holes can be used as a probe to test the nature of the compact object. The idea is to fit the thermal spectra of the black hole accretion disc with a known model which will be a function of BH parameters as well as a deviation parameter. This method is called continuum fitting method [217] and is recently used to study the distinguishability of boson star accretions from that of black holes [218–221].

As the spin of the BH is highly correlated with the deviation parameter getting an accurate fit is not easy unless the BH is highly spinning or there is a very large deviation from the Kerr nature [222]. Another proposed method to distinguish BHs from other compact objects is to look for a certain unique feature in the emission spectra such as the properties of Iron K_α [223–225]. Usually, one expects more wide and broadened lines from a Kerr BH accretion disc as it involves highly relativistic phenomena. This iron line method is more efficient compared to the continuum fitting method as in this case it is easier to get independent measurements of the BH spin parameter and the Kerr deviation parameter [226, 227]. There have been methods based on the measurements of quasi-periodic oscillation frequencies [228] and X-ray polarimetry etc. Through the *measurements of radio waves* emitted from the supermassive black hole at galactic centres, one can test the nature of the object. One such test has been demonstrated using the BH shadow observations [229], the Event Horizon Telescope team recently achieved the first step towards this goal by imaging the supermassive BH in the galaxy M87 utilizing the very larger baseline interferometry [230, 231]. Another way is to study the pulsars in the vicinity of such a supermassive BH and see how much information about the central BH we can get from these. The inferred mass and spin parameter of the BH could be used to do a standard test of the Kerr nature.

2.4.1 Gravitational wave based tests of BH mimickers

2.4.1.1 Tidal deformability parameter estimation

The fact that a black hole cannot be tidally deformed, leads to a vanishing tidal Love number [232, 233]. Using a gravitational wave phasing formula which contains the tidal Love numbers [234, 235], one can directly measure these parameters from observations which in turn can be used to constrain the nature of the compact object constituting the binary system [190, 236, 237]. Measurement of the tidal deformability parameter from gravitational wave observations for various neutron star models is also studied in different contexts [234]. Recently, Cardoso et. al. [190] have calculated the tidal deformability parameters of non-black hole compact objects (including boson stars, gravastars, wormholes, and other toy models for quantum corrections at the horizon scale) and have studied the detectability of such parameters using advanced gravitational wave detectors. In reference [236], authors studied the distinguishability of boson star systems from black holes and neutron stars by measuring the tidal deformability parameter. A rigorous formulation of this test using Bayesian inference [237] has brought the idea closer to implementation on detected gravitational wave events.

In Ref. [190] authors calculated the tidal deformability parameter for different varieties of non-spinning boson stars and studied their detectability through gravitational-wave observations. The tidal deformability of boson stars with solitonic potential and quartic (minimal boson star) potential are obtained in a more general framework in [238] and authors find that the solitonic boson stars can be distinguished from black holes and neutron stars using the gravitational wave measurements of second-generation detectors. This analysis also shows that in order to distinguish quartic boson stars one needs to invoke more sensitive gravitational wave detectors such as Einstein Telescope. Table 2 of Maselli *et. al.* [239] provides a set of coefficients that can be used to obtain the equation of state independent universal relations connecting the moment of inertia, quadrupole moment and the tidal deformability parameter of a boson star.

Equation of state independent universal relations and the logarithmic limit to BH values for thin-shell gravastar models are studied in Ref.[240]. One can also use this to study the fundamental difference between gravastars and other compact objects.

2.4.1.2 The quasi-normal mode measurements

Another way to test the black hole nature is by using the quasi-normal modes [241] of the perturbed black hole formed by the merger [242–245]. For a Kerr black hole, all the quasi-normal modes are characterized by the mass and spin of the black hole according to the “no-hair” conjecture. Though the waveform models for exotic compact objects are less developed, there have been various attempts to calculate the quasi-normal modes of boson stars [246–248] and gravastars [249–251]. These can be used to discern boson stars and gravastars from black holes.

There have been studies to look into the difference in the quasi-normal modes emitted by boson stars compared to the BH case [252]. In Ref. [253], authors describe the possible quasi-normal mode spectra of minimal, massive and solitonic boson stars under axial and polar perturbations. It was found that the quasi-normal mode spectra has distinct features and can be used to distinguish black holes and boson stars.

The axial QNMs of a thick shell gravastar are calculated by Chirenti *et.al* [249] and for the case of thin shell GSs the QNMs corresponding to the axial and polar perturbations are studied by Pani et. al [254]. It is found that the QNM structure of a

GS is entirely different from that of a BH, and hence can be used to distinguish it from a BH [255].

2.4.1.3 Tidal heating estimation

Measurement of the so-called tidal heating parameter can also be used as a tool to test the black hole nature. Consider a black hole event horizon surrounded by external gravitating objects. The rotational energy of this black hole may dissipate gravitationally due to the tidal disruption of exterior matter [256]. The loss of energy and angular momentum of a Kerr black hole near the horizon can lead to non-zero values of the tidal heating parameter. The measured value of the tidal heating parameter will be zero for any system without an event horizon. The tidal heating effect shows up in the gravitational wave phasing [257, 258] which helps us to measure this effect from observations [259] and thereby test the black hole nature of the compact object.

2.4.1.4 From the echoes

It was proposed in Ref. [199] that the late ringdown waves can be used to distinguish black holes from black hole mimickers. Since the ringdown is a property related to the photon sphere, horizonless objects with the photon sphere can also exhibit ringdown modes hence it may also show similar waveform features compared to BH quasi-normal mode spectrum. On the other hand, the late-time ringdown signal is expected to eventually show up differences in the observed spectrum, this can be used to rule out possibilities of alternatives to black holes. In Ref. [199], authors demonstrated the importance of such tests to probe quantum effects at the horizon scale. This difference in the gravitational waveform, in the case of (horizonless) exotic compact objects, can be observed as the repeated damped sinusoidal waves appear at the late-ringdown. These are called echoes and in Ref. [260] the observable properties including the time delay between two consecutive echoes is calculated by considering various models for exotic compact object models. In order to measure echoes from gravitational wave observations of late-ringdown signal, a template-based search based on Bayesian inference is developed [261] and is ready to apply for real events.

2.5 A new method to test the binary black hole nature using gravitational wave observations

As we pointed out in the previous section, the definition of a Kerr BH is very closely tied with the "no-hair" conjecture which says that all the properties of a Kerr BH are completely described by its mass and spin. Tests based on the "no-hair" conjecture conjecture include quasi-normal mode ringdown analysis [242, 247, 248, 262], extreme mass ratio inspiraling binary system based analysis [207, 263–267], tidal deformability parameter estimation etc.

In this thesis, we propose a new method to test the binary black hole nature of the detected GW event by measuring the spin-induced quadrupole moments of the binary's constituents, whose values are unique for Kerr BHs in GR due to the "no-hair" conjecture. For an isolated Kerr BH, it is well-known that quadrupole moment scalar is given by $Q = -m^3\,\chi^2$, where m is the mass of the BH and χ is the magnitude of the dimensionless spin parameter defined as $\vec{\chi} = \frac{\vec{S}}{m^2}$ (where $\vec{S}$ is the spin angular momentum vector of the BH). For a non-BH compact object, this may be generalized to $Q = -\kappa\, m^3\,\chi^2$, with $\kappa = 1$ as the BH limit. Depending on the equation of state, studies have shown that for neutron stars (NS), κ may range between $\simeq$ 2–14 [268, 269]), for boson stars between $\simeq$ 10–150 [193].

The next higher-order effect, called the spin-induced octupole moment term is related to the mass and spin of the system as, $O = -\lambda\, M^4\,\chi^3$ where the coefficient λ take the value unity for Kerr black holes whereas $\lambda \sim 4 - 30$ for neutron stars [270–272]. The spin-induced multipole moments of many of the black hole mimicker models are also available. For example, the variation of spin-induced quadrupole and octupole moment parameters of a specific class of spinning boson star system in the mass-spin parameter plane is shown respectively in Figs. 4 and 5 of [193]. The κ and λ values for this case found to be vary between $\sim 10 - 150$ and $\sim 10 - 200$ respectively [193].

Refs. [149, 240, 273] discusses the spin-induced multipole moments for thin shell gravastar models. According to their model, the quadrupole moment of a thin shell gravastar can be written as (see Eq. (2.11) of Ref.[240]),

$$Q_A = \chi_A^2\, M_A^3 + \frac{8}{5} B_A M_A^3, \tag{2.1}$$

where M_A is the mass of the component of the system and B_A is an integration constant. We used index A to denote the binary constituents. The value of B_A depends solely on the particular GS model chosen and the expression can be found in the appendix C of Ref. [273], which is shown to be a function of mass, compactness, inner and outer radii, angular momentum etc of the model chosen. We can rewrite the Eq. (2.1) as,

$$Q_A = \chi_A^2 \, M_A^3 \left(1 + \frac{8}{5} \frac{B_A}{\chi_A^2}\right) \tag{2.2}$$

The value of $\left(1 + \frac{8}{5} \frac{B_A}{\chi_A^2}\right)$ is unity for a Kerr BH and is called the spin-induced quadrupole moment coefficient. The variation of the spin-induced quadrupole moment parameter of a thin shell GS model as a function of the inverse of the compactness for different values of the dimensionless mass parameter is shown in Fig. 7 of [273]. It is shown that the value can be negative, positive or zero depending upon the value of the properties of the model chosen, such as the mass, compactness, inner and outer radii, angular momentum, etc. As the spin-induced quadrupole moment parameter value also crosses (goes beyond the BH value) the BH value it is not easy to distinguish a GS from a BH just from the measurement of the spin-induced multipole moment parameters.

We propose to use the inferred values of spin-induced quadrupole and octupole moment parameters from the gravitational observations of a binary black hole system to distinguish them from binaries composed of black hole mimickers. As we discussed in Sec. 1.3, the post-Newtonian waveform carries information about the spin-induced moments of binary black hole systems. By using various parameter estimation techniques (Sec. 1.4), we can quantify the precision with which the spin-induced multipole moment parameters can be measured within the statistical error bars. If we find that the signal agrees with the black hole value, the bounds (or the width of the posterior distribution) obtained at that particular case can be mapped to the constraints on the black hole mimicker model parameters. If we find an offset from the binary black hole value this will need detailed further investigation. We explore these possibilities in detail in the coming chapters utilizing the sensitivities of various ground and space-based gravitational wave detectors.

Chapter 3

Testing the binary black hole nature using spin-induced multipole moment measurements

In this chapter, we discuss the details of our proposal to use spin-induced multipole moment parameters to distinguish black holes from other objects. We also show the explicit appearance of these parameters in gravitational wave forms in Sec. 3.1. In Sec. 3.2, we provide a crisp summary of the analysis with details.

3.1 Spin-induced multipole moment terms in the post-Newtonian waveforms

Evolution of a compact binary system during the inspiral phase is accurately modeled by the post-Newtonian formalism (see [274] for a review). While sufficiently accurate post-Newtonian gravitational waveforms (for the purposes of detection and the parameter estimation) from compact binaries with non-spinning constituents in quasi-circular orbits were made available as early as early 2000s [275–277], higher order spin effects were included through a number of recent investigations [278–288]. For our purposes, we choose to work with a frequency domain waveform where the spins are (anti-) aligned with respect to the orbital angular momentum [288]. The state-of-the-art frequency domain waveform for compact binaries with (anti-) aligned spin components incorporates spin-orbit effects in phasing up to 4PN (leading effect appears at 1.5PN order in the phase), spin-spin effects up to 3PN (starting at 2PN) and the leading cubic-spin terms at 3.5PN. Moreover, the amplitude involves spin effects up to 2PN.

This waveform is a variant of the one that is presented in Ref. [30]. These are constructed by simply making the dependences on parameters characterising the spin-induced quadrupole moment (through κ_s and κ_a) and spin-induced octupole moment (through λ_s and λ_a) explicit in the waveform, which were set to their respective values for Kerr BHs while writing the waveform model of Ref. [30]. In this section we list various pieces of the waveform where such dependences occur.

Let us first recall the schematic expression for the frequency domain amplitude of a gravitational wave signal, $\tilde{h}(f)$, given in Ref. [30]. [1] This reads,

$$\tilde{h}(f) = \frac{M^2}{D_L}\sqrt{\frac{5\,\pi\,\nu}{48}}\sum_{n=0}^{4}\sum_{k=1}^{6} V_k^{n-7/2}\,C_k^{(n)}\,e^{\mathrm{i}(k\,\Psi_{\mathrm{SPA}}(f/k)-\pi/4)}\,. \tag{3.1}$$

Here, M, ν and D_L denote the total mass, symmetric mass ratio parameter and the distance to the binary, respectively and the indices n and k denote the PN order and harmonic number, respectively. The coefficients $\mathcal{C}_k^{(n)}$ denote the amplitude corrections associated with the contribution from kth harmonic at nth PN order (notice that n takes half integer values as well). The post-Newtonian parameter, V_k, is defined as v= V_k(f)=(2 M f/k) forthekthharmonic. Related expressions for each of the $\mathcal{C}_k^{(n)}$s can be found in Ref. [30, 284]. In Appendix A we list the only coefficient which has explicit dependence on the parameters (κ_s and κ_a) and corresponds to the contributions from the 2nd harmonic at the 2PN order ($\mathcal{C}_2^{(4)}$). In addition, Ψ_{SPA} represents the phase of the first harmonic in the frequency domain as obtained under the Stationary Phase Approximation (SPA) (see sec. VI of Ref. [284] for details on SPA). Schematically the expression for this phase can be written as follows

$$\Psi_{\mathrm{SPA}}(f) = 2\pi f\,t_{\mathrm{c}} - \phi_{\mathrm{c}} + \left\{\frac{3}{256\,\nu\,v^5}\left[\psi_{\mathrm{NS}} + \psi_{\mathrm{SO}} + \psi_{\mathrm{SS}} + \psi_{\mathrm{SSS}}\right]\right\}_{v=V_k(f)}\,, \tag{3.2}$$

where ϕ_{c} denotes the orbital phase at the instant t_{c} of coalescence, ψ_{NS} represents the non-spinning contributions to the phasing. In Eq. 3.2, ψ_{SS} and ψ_{SSS} denote quadratic and cubic in spin terms respectively.

---

[1] Pre-factor of Eq. 1 of Ref. [30] should be multiplied with a factor $1/\sqrt{\nu}$. We have corrected this in the Eq. ((15)).

We provide expressions for coefficients that contain explicit dependence on κ_s, κ_a and λ_s, λ_a in Appendix A 5.5 and can be combined to those listed in Ref. [30, 284] to write the final waveform expression. The spin-induced quadrupole and octupole moment parameters of the binary system, κ_s, κ_a and λ_s, λ_a are defined as, $\kappa_s{=}\frac{1}{2}\left(\kappa_1+\kappa_2\right)$, $\kappa_a{=}\frac{1}{2}\left(\kappa_1-\kappa_2\right)$ and $\lambda_s{=}\frac{1}{2}\left(\lambda_1+\lambda_2\right)$, $\lambda_a{=}\frac{1}{2}\left(\lambda_1-\lambda_2\right)$. In our notation, κ_1 and κ_2 (λ_1 and λ_2) are the spin-induced quadrupole moment (octupole) parameters of the binary constituents.

As we briefly mentioned earlier, the effect of the leading spin-induced multipole moment (mass-type quadrupole, $M_2{=}-M^3\,\chi^2$) in the phasing of gravitational waves from binary black hole systems was first computed in [289] and contributes to the gravitational wave phase at 2PN order. Here, the symbols M and χ again represent the mass and dimensionless spin parameter for *each* binary component while the negative sign (by convention) indicates that the spin induces oblateness to the black hole. Post-Newtonian corrections to this at 3PN order has been computed in [282]. The sub-leading, spin-induced multipole moment (current-type octupole, $S_3=-M^4\,\chi^3$) starts to contribute to the phase at 3.5PN order and was computed in [283]. Notice, the spin dependences of the spin-induced multipole moments here: $M_2(S_3)$ have quadratic (cubic) dependences on the spin parameter and first appear in the phasing formula at 2PN (3.5PN) order because these are the orders at which quadratic-in-spin (cubic-in-spin) terms start to appear in the gravitational wave phase.

Note that the relations for M_2 and S_3 assume that the binary constituents are black holes but can be generalized for a non-BH compact object by introducing coefficients that characterize the degree of deformation. For instance, we can rewrite these relations as : $M_2{=}-\kappa\,M^3\,\chi^2$ and $S_3=-\lambda\,M^4\,\chi^3$ where the coefficients κ and λ take the value unity for Kerr black holes whereas they deviate from unity for other types of compact objects including exotic alternatives to black holes. For example, the values of κ and λ for neutron stars, depending upon the neutron star equation of state and mass, range between $\sim 2-14$ and $\sim 4-30$, respectively [270–272]. The spin-induced multipole moments of a few exotic compact objects are also computed in the literature: for a particular class of spinning boson star system κ (λ) can take values between $\sim 10-150$ ($\sim 10-200$) [193]. Variation of quadrupole and octupole moment parameters in the boson star mass-spin parameter plane is shown respectively in Figs. 4 and 5 of [193]. Similar computations have been done for gravastars, see for instance Refs. [149, 240, 273] which discuss spin-induced multipole moments for thin shell gravastar models. If the observed values of spin-induced quadrupole moments are offset from black hole value,

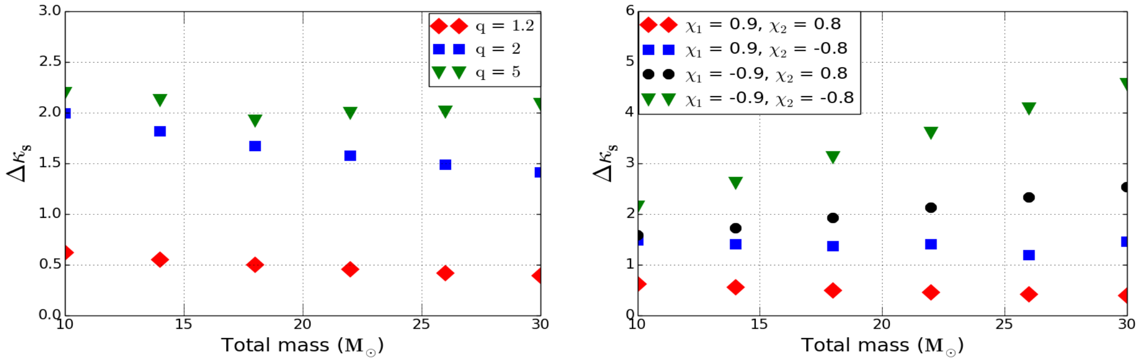

FIGURE 3.1: Errors in measuring κ_s as a function of binary's total mass for three different mass ratio cases (left panel) and for different spin configurations (right panel) for advanced LIGO. The values of dimensionless spin parameters (χ_1, χ_2) are fixed at 0.9 and 0.8 for the left panel plots where as mass ratio (q) is fixed to be 1.2 for the plots in the right panel. Both panels assume a fixed inclination angle of the binary, $\iota = \frac{\pi}{3}$. The binary's location and other angular parameters are chosen in a way that produces an observed signal to noise ratio of 10.

it may be interpreted as an evidence of an exotic compact object. On the other hand, if the posterior distribution for the observed value is found to be peaking at 1 with a width, the corresponding error bars can be translated into an upper bound on the allowed value of the parameter for the particular system.

In this chapter, we compute the projected accuracies on the measurement of the spin-induced quadrupole moment coefficient of the binary system using the semi-analytical parameter estimation technique of the Fisher information matrix in order to demonstrate the method follows with the detailed results, see Sec. 1.3.2 for more details about the Fisher matrix analysis.

3.2 Demonstration of the method

3.2.1 Details of the analysis

In the PN model of compact binaries, the spin-induced quadrupole moment terms appear at the same order where the leading order quadratic-in-spin terms appear (note $Q \propto \chi^2$), which is second PN order [34]. The parameter, κ, that characterises the magnitude of the spin-induced quadrupole moment (given the nature of the object), for each binary component, can be tagged as κ_1 and κ_2, following the notation of [290].[2] If we re-write the waveforms in terms of the symmetric and anti-symmetric combinations of κ_1 and κ_2 given by $\kappa_s = (\kappa_1 + \kappa_2)/2$ and $\kappa_a = (\kappa_1 - \kappa_2)/2$, respectively, then a BBH system is specified by $\kappa_s = 1, \kappa_a = 0$. This suggests, if we can accurately measure κ_s and κ_a to be 1 and 0, respectively, we have established that the detected compact binary is a BBH.

However, note that κ_s and κ_a are highly degenerate parameters whose simultaneous extraction turns out to yield almost no constraint on them. Hence, we resort to a method where we fix κ_a to be 0, as expected for a Kerr BBH, and then calculate the error bars associated with the measurement of κ_s from GW observations. The aim here is to see how well can we estimate κ_s around the true value of 1 (for a BBH) and hence confirm that the observed system is indeed a BBH. These error bars can be interpreted as upper bounds on the value of κ_s allowed for exotic compact objects. In this sense, the proposed test is a “null-test" of the BBH nature, where, observations would constrain the allowed range of deviations of κ_s from the BBH value. Moreover, since the spirit of the test relies on the fact that quadrupole moments of BHs in a BBH system would depend only on the mass and the spin, the proposed test can be regarded as the “no-hair” theorem test for the BBHs.

We wish to clarify that the error bars here refers to the width of the measured distribution of κ_s at a fixed confidence level (in our case 1σ). Depending on the masses and spins of the system, this width may be much larger than 1, in which case this may be better interpreted as an upper bound on the allowed value of κ_s for the given system. In most cases we have studied (in context of advanced LIGO), it is less than ~ 20 (see Figs 1 and 2). Since κ_s for interesting BH mimickers such as Boson stars can be as high as 150, the proposed method will be able to put stringent, model independent constraints on the parameter space of BH mimickers. It should also be noted that, though we have posed this as a null test, the proposed test can detect the signatures of exotic compact objects through a shift in the peak of the measured distribution away from 1, as is expected for BH mimickers.

In general, if we parametrize the deviation of κ by $\kappa = 1 + \alpha$ (where α is the deformation parameter which is 0 for BHs), and assume that the constituents of the binary are of identical types ($\alpha_1 = \alpha_2$) then, again, showing $\kappa_s = 1$ is equivalent to showing the BBH nature of the compact binary system. This is because we again have

---

[2] Throughout the thesis, suffix 1 refers to the heavier compact binary component and 2 the lighter one.

$\kappa_a \equiv 0$, which is consistent with our original assumption for BBHs. Note that even if the detected compact binary constitute of two stars which have $\kappa \neq 1$, the proposed method will be sensitive in detecting them as they will add to the systematic offset in the measured value of κ_s from 1. Hence our proposal to measure only κ_s should work for compact binaries with any combination of compact objects when applied to the real data.

Here we use a waveform which is 2PN in amplitude and 4PN [3] in phase and spins of the two compact objects are considered to be along or opposite to the orbital angular momentum vector of the binary as explained in Sec. 3.1. The spin-induced quadrupole moment coefficient appears at 2PN, 3PN and 3.5PN orders. The spin-induced octupole moment coefficient which appear at 3.5PN is set to 1, the BH value as we focus only on quadrupole here. See Appendix 5.5 for more details.

3.2.2 Estimation of κ_s

We use the semi-analytical parameter estimation technique based on the Fisher information matrix formalism [291] to deduce typical accuracies with which κ_s may be estimated from GW observations. Fisher information matrix approach allows us to calculate the the widths of the posterior distribution of various parameters for Gaussian noise and in the limit of high signal to noise ratio (SNR) (see [292] for detailed discussion on the possible caveats). Unlike previous works with PN waveforms which have sub-dominant modes (e.g. [293, 294]), we truncate the waveforms at *twice* the orbital frequency of the binary when it reaches the inner-most stable circular orbit ($2F_{\rm ISCO}$) as opposed to the choice of $kF_{\rm ISCO}$, where k is the maximum number of harmonics of the orbital phase present in the waveform. Here, the ISCO frequency is computed using numerical fitting formulae listed in Eqs. (3.7)-(3.8) of [295, 296]. By doing so we hope to control the systematics due to the neglect of merger and ringdown. Though much less realistic than numerical methods based on algorithms such as Markov chain Monte-Carlo (MCMC), the semi-analytic method used here is significantly inexpensive in terms of computational time and is expected to match with the predictions of numerical methods in the high SNR limit [297]. However, we caution that the errors we quote here should be taken as a typical order of magnitude of the expected errors which will be quantified in the future with MCMC investigations.

---

[3] Note that the phasing formula at the 4PN only includes spin-orbit tail terms and hence is only partial. See a related discussion in Ref. [30]

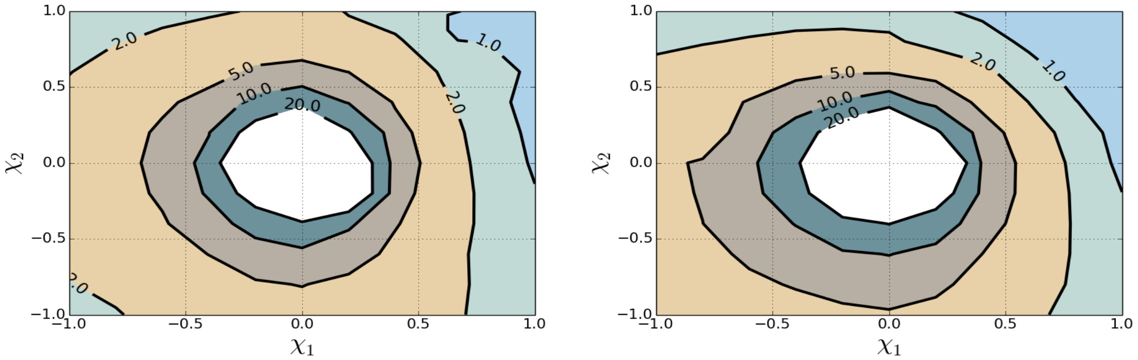

FIGURE 3.2: Two dimensional error contours indicating the measurability of κ_s in the $\chi_1 - \chi_2$ plane for two representative binary systems: $(5,4)M_\odot$ (left panel) and $(10,9)M_\odot$ (right panel) for advanced LIGO sensitivity. The inclination angle of the binary is chosen to a value of $\pi/3$ and the source is located and oriented in such a way that it produces a signal-to-noise ratio of 10 at the detector.

For every system of interest, we construct a Fisher information matrix, using the waveform model discussed above for the set of parameters $\{t_c, \phi_c, D_L, \iota, \mathcal{M}, \delta, \chi_1, \chi_2, \kappa_s\}$ which describe the signal. Here, t_c and ϕ_c denote time and phase of the waveform at coalescence, two mass parameters; $\mathcal{M} = (m_1 m_2)^{3/5}/(m_1+m_2)^{2/5}$ and $\delta = |m_1 - m_2|/(m_1+m_2)$, are known as the chirp mass and difference mass-ratio of the binary; parameters (χ_1, χ_2) denote the dimensionless spins of the binary components; finally, D_L and ι are the luminosity distance and the inclination angle of the binary, respectively. We consider the problem from a single detector stand point, and hence do not include the angles which describe the source location in the set of parameters. We compute the lower bound on the errors of each parameters (Cramer-Rao bound) by taking the square root of the diagonal values of the inverse of the 9×9 Fisher information matrix (co-variance matrix). These errors are calculated for different masses and spins of the compact binary systems as well as for different inclination angles (ι). We consider the sources to be located and oriented in such a way that it produces an SNR of 10 at the detector. Projected advanced LIGO noise PSD [52] is used to compute the errors. The 1σ error bars on κ_s (with a peak at 1) assumes $\kappa_a = 0$, which is the case for Kerr BBHs. From a GW event, if we find that the posterior distribution for κ_s is offset from 1, it may be taken as a signature for at least one of the binary component to be a non-BH object. Throughout the paper we quote errors in the measurement of parameters characterising the spin-induced effects. However, as mentioned earlier, for many parts of the parameter space we find that errors are larger than 100% for which the quoted errors should be considered as 'bounds' on the parameter in question.

3.2.3 Results and Discussions

The dependencies of the errors (for a fixed SNR of 10) in measuring κ_s as a function of the total mass, for few mass ratio cases (left panel) and spin configurations for a near-equal mass system (right panel) for advanced LIGO sensitivity are shown in Fig. 3.1. This clearly shows that the proposed test works very well for *highly spinning, near equal mass systems.* Evidently, the observed improvement for rapidly spinning systems can be attributed to the large spin-induced quadrupole moment they possess. In addition, for nearly equal mass systems, the best estimates of κ_s come from compact binaries in which the spins of both components are aligned w.r.t. the orbital angular momentum vector of the binary and the worst estimates are for those cases where the component spins are anti-aligned w.r.t. the orbital angular momentum. The decrease in the errors with mass ratio may be attributed to the additional mass ratio and inclination angle dependences that amplitude corrections bring in, which affect the correlation of κ_s with other parameters (especially spins) in a non-trivial way leading to the observed trend. On the other hand, the dependence of the errors on the spin orientation is due to its effects on the upper cut-off frequency. The figure shows that even with a moderate SNR of 10, the proposed test works very well for a number of mass ratio and spin configurations, where the best cases have $\Delta\kappa_s < 0.5$ (50%). It is worth recalling that the allowed values of κ_s for BBH mimickers, such as binaries involving boson stars, can be as high as 150. Hence the expected bounds are capable of putting stringent constraints on those models.

Figure 3.2 displays the dependence of the errors of κ_s on the component spins for two representative stellar mass compact binaries with component masses $(5,4)M_\odot$ and $(10,9)M_\odot$. Results are very promising and show that for dimensionless spins larger than 0.5, the errors in estimating κ_s is smaller than ~ 5 in both the cases. This would mean that the proposed test could be effective in certain cases even with moderate spins.

Since the GW detectors are poised to observe tens to hundreds of BBH mergers in the coming years, we also have the interesting possibility of combining the constraints from these individual observations. If there are N events for which the test yields a meaningful bounds on κ_s, the resulting bound combining all the N events would be better by $\sim \sqrt{N}$. Hence the combined posterior of about 100 events, on the null hypothesis, may narrow down the constraints on κ_s by a factor 10.

Possible constraints on κ_s from space-based detectors: With the recent success of LISA pathfinder mission [298], there is renewed interest in pursuing a GW

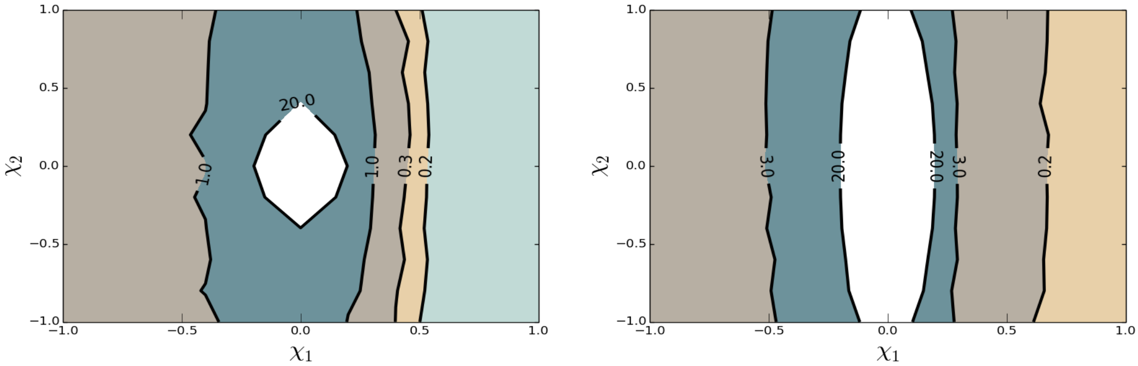

FIGURE 3.3: Projected constraints from GW observations of supermassive BBH (SMBBH) mergers by LISA detector as a function of the component spins for two representative SMBBH configurations, $(5 \times 10^6, 10^6)M_\odot$ (left panel) and $(10^7, 10^6)M_\odot$ (right panel), located at 3 Gpc. The inclination angle of the binary is chosen to a value of $\pi/3$.

detector in space with low frequency sensitivity, capable of observing supermassive BBH (SMBBH) mergers. Towards this goal, we extend our study to the case of low frequency space based detectors like LISA and projected constraints possible on κ_s from them. The results are shown in Fig. 3.3 which uses the noise PSD of Ref. [8]. The SMBBH system is assumed to be at a luminosity distance of 3 Gpc. We find that the LISA observations of SMBBH mergers can very accurately constrain the κ_s parameter and hence confirm the BBH nature of the observed sources, tightly constraining any alternatives to BBHs. It should be clear from Fig. 3.3 that errors in measuring κ_s are smaller than 10% for a number of configurations with moderate spins–making the test an extremely deep probe of any possible deviation from BBH nature. These results show how LISA can be a very sensitive probe of fundamental physics.

Possible constraints on BH mimickers: Since boson stars can have κ between $\sim 10-150$ [193], binary systems of boson stars may have κ_s in the range $\sim 10-150$. This allowed range lies well within the reach of the proposed test. Recently for slowly rotating thin shell gravastars, Ref. [299] showed that the spin-induced quadrupole can take a wide range of values depending on the specifics of the model (see Fig. 7 of [299]). This range includes $\kappa = 1$, the BH value, too. Indeed, if $\kappa_{GS} = 1$, our test will not be able to distinguish it from a BH. Except for this very fine-tuned scenario, the projected bounds from the proposed test might significantly help to constrain the allowed parameter space of gravastars and can influence the theoretical developments in the field. Details of the bounds possible on specific BH mimicker models will be reported elsewhere [300].

3.3 Conclusions

Spin-induced multipole moment parameters explicitly appear in the post-Newtonian waveforms, which models inspiralling compact binaries, can be used test the black hole nature of the compact object using gravitational waves. Using Fisher information matrix analysis we can estimate the expected upper bounds on the spin-induced quadrupole moment parameters as they explicitly appear in the post-Newtonian waveform models. In chapter 5 we will show the implications of this test binary black hole systems which are observable by third generation gravitational wave detectors and space-based gravitational wave detectors.

We note that the proposed test may not be very sensitive in distinguishing a BH from a BH mimicker in a NS-BH system. This is because the neutron stars are expected to have small spins (≤ 0.05) for which spin-induced quadrupole would be very small. Moreover, since NS are expected to have κ value in the range $2-14$, very accurate estimation of the κ parameters of both the binary components is necessary to make the above distinction. This may be possible only with the future generation of GW detectors.

There are some effects which can potentially contaminate the effectiveness of the proposed test. Because the compact objects in binaries are, strictly speaking, not isolated, the “no-hair” conjecture holds only approximately due to which there can be systematic effects which may affect the test (see Ref. [301] for a discussion on this aspect). Further, if the BHs are charged, then the resulting values of κ will be offset from the Kerr value. Lastly, the choice of upper cut-off frequency may be different from ours if the object has structure and hence can cause systematic errors in our estimates. These issues need more careful examination which will be carried out in the future.

We conclude by noting that, once implemented in a Bayesian framework, this proposal can be used to represent every detected compact binary system as contours in the $\kappa_1 - \kappa_2$ space. Using multiple observations, the joint posteriors can tighten the bounds from this proposed null test, potentially constraining the parameter space allowed for non-BH compact objects. Inclusion of precessional features in the waveform and incorporating this effect into effective one body waveforms or phenomenological waveforms, which capture merger and ringdown phases as well, are likely to yield tighter constraints and will be explored in the later chapters.

Chapter 4

Application of the method to real gravitational wave events

Here, we present a Bayesian framework to carry out the tests of BH nature where we measure the symmetric combination of individual spin-induced quadrupole moment parameters fixing the anti-symmetric combination to be zero. The analysis is restricted to the inspiral part of the signal as the spin-induced deformations are not modelled in the post-inspiral regime. We perform detailed simulations to investigate the applicability of this method for compact binaries of different masses and spins and also explore various degeneracies in the parameter space which can affect this test.

We then apply this method to the gravitational wave events, GW151226 and GW170608 detected during the first and second observing runs of Advanced LIGO and Advanced Virgo detectors. We find the two events to be consistent with binary black hole mergers in general relativity. By combining information from several more of such events in future, this method can be used to set constraints on the black hole nature of the population of compact binaries that are detected by the Advanced LIGO and Advanced Virgo detectors.

4.1 Introduction

In Chapter 3, we proposed a new method to distinguish between binary black holes and binary black hole mimickers by measuring the spin-induced multipole moments of the compact objects.This Fisher matrix study carried out in chapter 3, explored the accuracy with which the spin-induced quadrupole moment parameters can be measured for non-precessing binaries with various masses and spins. This test was performed with a post-Newtonian waveform with 4PN (*partial*) phase corrections and 2PN amplitude corrections and considered a one-parameter deformation of the binary black hole waveforms parametrized by the symmetric combination defined by $\kappa_s = \frac{1}{2}(\kappa_1 + \kappa_2)$, where $\kappa_{1,2}$ denote the spin-induced quadrupole moment parameters of the binary constituents. The study showed that with the second generation (2G) ground-based detectors, the spin-induced quadrupole moment parameters can be measured with reasonable accuracy for highly spinning and nearly equal mass binaries with aligned spin orientations.

In this chapter, we implement and demonstrate the method given in chapter 3(also [302]) within the framework of Bayesian inference and perform tests of binary black hole nature of the LIGO-Virgo detected binary black hole events. Our method uses binary black hole waveforms with parametrized deformations on the spin-induced quadrupole moment coefficients κ, defined as $\kappa = 1 + \delta\kappa$ where the parametrized deformations (labeled as $\delta\kappa$) represents the deviations from binary black hole nature. We make use of the *LALInference* [12, 303] library to measure the parameterized deformations $\delta\kappa$ of compact binaries which can be considered as the bounds on their departures from binary black hole natures. Our method also includes estimation of Bayes factors to perform Bayesian model selection between binary black hole models and black hole mimicker models.

We perform detailed studies to demonstrate the method using simulated GW signals (injections) which include those of various masses and spins. We investigate in detail about various degeneracies in the parameter space and associated systematics in the estimated parameters, which may often restrict the applicability of this test. Finally, we apply this method on the LIGO-Virgo detected binary black holes GW151226 and GW170608 and obtain constraints on their BH natures.

The rest of this chapter is organized as follows. In Section 4.2, we discuss the waveform model used in this study and give a brief overview of Bayesian inference for parameter estimation and model selection. Section 4.3 covers our detailed simulation studies and results, and in section 4.4, we present the constraints obtained from the real events GW151226 and GW170608.

4.2 Method

4.2.1 The waveform model

In frequency domain, the gravitational wave signal from compact binary inspirals in the detector frame can be schematically written as,

$$\tilde{h}(f) = \mathcal{C}\,\mathcal{A}(f)\,e^{i\psi(f)}, \tag{4.1}$$

where, $\psi(f)$ is the phase and $\mathcal{A}(f)$ is the amplitude of the gravitational wave signal which is given by $\sim D_L^{-1}\,M_c^{5/6}\,f^{-7/6}$ where M_c is the chirp mass, which is related to individual masses m_1 and m_2 as, $M_c = \frac{(m_1\,m_2)^{3/5}}{(m_1+m_2)^{1/5}}$, and D_L is the luminosity distance to the source. The factor $\mathcal{C}$ carries the antenna response of the interferometers as a function of the source location and orientation parameters.

The orbital evolution of the inspiralling binary is largely encoded in the phasing formula and appears in terms of the masses and spins of the binary [1]. Due to the recent developments in the post-Newtonian modeling of compact binaries [27], the phasing formula for the inspiralling binary has been computed accurately up to 3.5PN order [46, 48, 274, 278–283, 285–288, 304, 305].

This phasing formula accounts for the higher-order spin corrections such as spin-orbit interactions (at 1.5PN, 2PN, 3PN and 3.5PN orders) and spin-spin interactions (at 2PN and 3PN orders).

Since the spin-induced quadrupole moment parameter is unity for Kerr BHs, the waveforms which are particularly developed for binary black hole systems a priori assume the value unity. However, for this study, since our interest is in those binary systems for which κ departs from *unity*, we re-write the Eqn. $Q = -\kappa\,\chi^2\,m^3$ in the following form,

$$Q = -(1+\delta\kappa)\,\chi^2\,m^3, \tag{4.2}$$

where $\delta\kappa$ is the parametrized departure of κ from unity. Hence $\delta\kappa = 0$ is the BH limit and non-zero $\delta\kappa$ corresponds to non-BH objects. Our proposal is to independently measure $\delta\kappa$ and use the measurement to put possible constraints on the allowed parameter space of BH mimicker models from observed gravitational wave events.

---

[1] We have not considered the effects due to orbital eccentricity, tidal deformations due to the presence of external gravitational field *etc.* in the waveform.

For this study, we use the `IMRPhenomPv2` [306] waveform approximant which is available in LSC Algorithm Library, by incorporating into it, the parametrized deformations shown in Eq. (4.2). `IMRPhenomPv2` is a frequency domain inspiral-merger-ringdown waveform model whose inspiral part of the phasing agrees with the PN phasing and the merger-ringdown parts are obtained by calibrating to the *numerical-relativity* waveforms [305–309]. These *numerical-relativity* waveforms have been computed by assuming binary black hole nature (*ie*, $\delta\kappa_s = 0$) by default. Therefore the merger and ringdown phases of the `IMRPhenomPv2` do not account for the κ effects hence the analytical parametrization described in Eq. (4.2) is not expected to be valid once the binary enters into the merger regime of the evolution. To avoid any systematic biases due to this, we truncate our analysis at the inspiral-to-merger transition frequency of the `IMRPhenomPv2` defined by $f_{\text{upper}} = 0.018/M$, where M is the total mass of the system [13]. As investigated in Ref. [83], we expect negligible amount of spectral leakage effects due to this sharp cut-off.

4.2.2 Choice of test parameters

In the most general case, each compact object in the binary can have independent spin-induced quadrupole moments κ_1 and κ_2 which are different from the Kerr value of unity. Hence we can parametrize a potential deviation of the BH nature by introducing two independent deformation parameters $\delta\kappa_1$ and $\delta\kappa_2$ given by $\kappa_{1,2} = 1 + \delta\kappa_{1,2}$. Due to the strong degeneracy between $\delta\kappa_{1,2}$ in the gravitational waveform, simultaneous measurement of the two would yield very weak constraints [302, 310].

Hence one may resort to an alternative approach where one of the linear combinations of the $\delta\kappa_{1,2}$ parameters is estimated from the data. Following [302], we consider the symmetric combination $\delta\kappa_s = \frac{1}{2}(\delta\kappa_1 + \delta\kappa_2)$ as the parameter which captures the deviation from binary black hole nature and estimates the associated error bars when the anti-symmetric combination is zero ($\delta\kappa_1 = \delta\kappa_2$). Though restrictive, this does not weaken the proposed null test because a break down of this assumption is also likely to lead to a shift of the peak of the posterior of $\delta\kappa_s$ away from zero which is what we look for as evidence for the presence of black hole mimickers.

4.2.3 Overview of Bayesian inference

Following the brief review of Bayesian inference for gravitational wave parameter estimation and model selection provided in Sec. 1.4, here we summarise the technical details keeping the present context of testing the binary black hole nature in mind.

To test the binary black hole nature of the compact binaries, we define the following two models:

1. The binary black hole model $\mathcal{H}_{BH}$ which reads as "*The source of the gravitational wave signal is binary black holes in general relativity*". For this model, the waveform assumes κ_s to be unity (or $\delta\kappa_s = 0$) and the set of parameters defining this model (*i.e.*, binary black hole parameters) is denoted as $\vec{\theta}_{\rm BH}$.

2. The non-BH model $\mathcal{H}_{non-BH}$ which reads as "*The source of the gravitational wave signal is a binary of non-BH compact objects aka BH mimickers*". The waveform for this model allows κ_s to deviate from unity. Therefore we use $\delta\kappa_s$ as a free parameter and the set of parameters defining this model is given as $\vec{\theta}_{\rm NBH} = \{\vec{\theta}_{\rm BH}, \delta\kappa_s\}$.

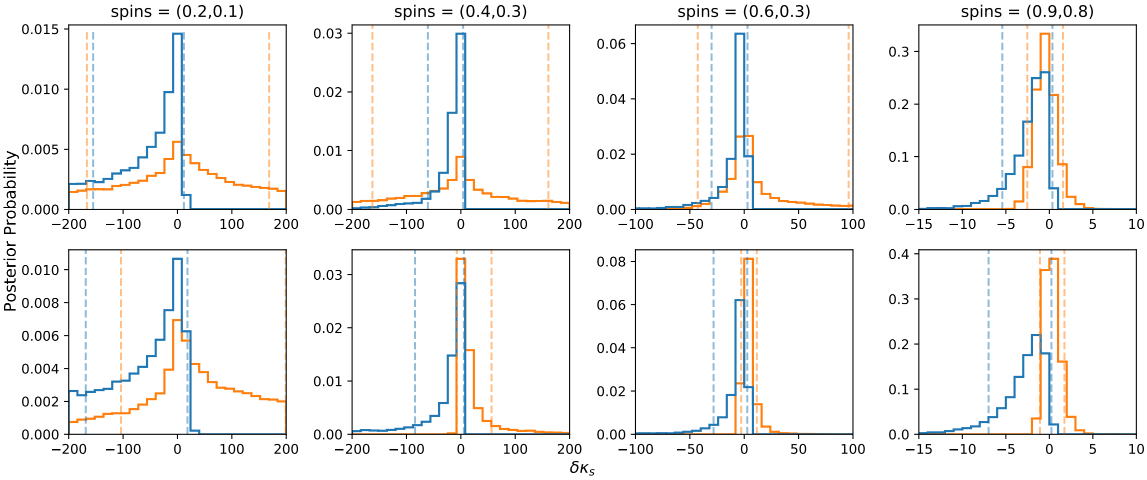

FIGURE 4.1: Posterior distributions on $\delta\kappa_s$ for a binary systems with total mass $15 M_\odot$ and mass ratio 1 (top row) and 2 (bottom row) for different spin magnitudes of (0.2, 0.1), (0.4, 0.3), (0.6, 0.3) and (0.9, 0.8) from left to right in each row. Binaries are assumed to be optimally oriented at a luminosity distance of 400 Mpc. Different colours represent different injected spin orientations: both spins aligned to the orbital angular momentum (light blue) and both spins anti-aligned to the orbital angular momentum (orange).

The one-dimensional posterior for $\delta\kappa_s$ parameter can be obtained by marginalizing the multi-dimensional posterior over the other parameters, *i.e.*,

$$P(\delta\kappa_s|\mathcal{H}_{non-BH}, d) = \int P\left(\{\overrightarrow{\theta}_{\rm BH}, \delta\kappa_s\}|\mathcal{H}_{non-BH}, d\right)\, d\overrightarrow{\theta}_{\rm BH}, \tag{4.3}$$

and the 90% credible intervals on $\delta\kappa_s$ are obtained as the shortest interval $(\delta\kappa_s^l, \delta\kappa_s^r)$ which contains 90% of the posterior probability distribution, *i.e.*,

$$\int_{\delta\kappa_s^l}^{\delta\kappa_s^r} P(\delta\kappa_s\,|\mathcal{H}_{non-BH}, d)\, d\delta\kappa_s \sim 0.9. \tag{4.4}$$

To perform model selection between the BH and non-BH models, we compute the Bayes factor between $\mathcal{H}_{non-BH}$ and $\mathcal{H}_{BH}$ as follows,

$$\mathcal{B}_{BH}^{generic} = \frac{\mathcal{Z}_2}{\mathcal{Z}_1}, \tag{4.5}$$

which quantifies how well the data favors the BH mimicker hypothesis $\mathcal{H}_{non-BH}$ over the BH hypothesis $\mathcal{H}_{BH}$. When there is no prior preference for one model over the other, then Bayes factor is same as the odds ratio between the two models (Odds ratio is defined as the ratio of posterior probabilities of the two models *i.e.*, $P(\mathcal{H}_{non-BH}|d)/P(\mathcal{H}_{BH}|d)$). Following definition of evidence in Eq. (1.15), the Bayes factor in Eq. (4.5) can be written as,

$$\mathcal{B}_{BH}^{generic} = \frac{\int P(\overrightarrow{\theta}_{\rm NBH}|\mathcal{H}_{non-BH})\, P(d|\overrightarrow{\theta}_{\rm NBH}, \mathcal{H}_{non-BH}) d\overrightarrow{\theta}_{\rm BH}\, d\delta\kappa_s}{\int P(\overrightarrow{\theta}_{\rm BH}|\mathcal{H}_{BH})\, P(d|\overrightarrow{\theta}_{\rm BH}, \mathcal{H}_{BH})\, d\overrightarrow{\theta}_{\rm BH}}. \tag{4.6}$$

For both parameter estimation as well as model selection studies in this chapter, we use *LALInference* [12] which is a Bayesian inference package available in the LSC Algorithm Library [12, 303]. *LALInference* makes use of stochastic sampling algorithms such as Nested Sampling [64], Markov Chain Monte Carlo (MCMC) sampling [65–67] *etc.* and we use Nested Sampling algorithm for the analysis in this study.

4.3 Studies using simulated data and results

In this section, we perform detailed studies using simulated data to assess the efficiency of the proposed method to distinguish between binary black holes and binaries comprising of black hole mimickers. The aim is primarily to quantify the bounds on the $\delta\kappa_s$ parameter as a function of the source parameters of the expected gravitational wave signal. We also present the Bayes factors between black hole mimickers and black hole models as a function of $\delta\kappa_s$.

4.3.1 Details of simulations

Masses: We choose binary systems with the total mass $M = 15M_\odot$ in the detector frame [2] and mass ratios $q = 1$ and $q = 2$ as representative cases. The masses are chosen such that they ensure the signals have a significant amount of inspiral in the detector band as the parametrization we employ is in the inspiral part of the waveform.

Spins: Four combinations of component spins (dimensionless spin magnitudes) are used: (0.2, 0.1), (0.4, 0.3), (0.6, 0.3) and (0.9, 0.8) which represent low, moderate, and high spins, respectively here the heavier BH in the binary always assumed to be highly spinning compared to the lower mass BH. Each component spin can be either aligned or anti-aligned with respect to the orbital angular momentum vector. Therefore, for each binary we consider four possible spin configurations: both are aligned, the heavier BH spin is aligned but the lighter BH spin is anti-aligned, the heavier BH spin is anti-aligned but the lighter BH spin is aligned and both BH spins are anti-aligned.

$\delta\kappa_s$ parameter: Binary black hole injections are generated with $\delta\kappa_s$=0 while non-BH injections are generated by choosing $\delta\kappa_s$ in the range [-40, 40]. The non-BH injections are used to compute the Bayes factors between the non-BH and BH hypotheses.

Extrinsic parameters: We choose a fixed distance of 400 Mpc for all the systems which is broadly motivated by the typical distances of several binary black hole mergers during the first two observing runs of Advanced LIGO and Advanced Virgo. For all the systems above, the sky-location and orientation are chosen in such a way that the optimal SNR for the detector network is highest for a given source with fixed distance and inclination. Both sky-location and orientation of the source can affect our estimates of $\delta\kappa_s$ only through the signal-to-noise ratio.

Prior choices: We use prior on $\delta\kappa_s$ to be uniform in [-200,200]. This range includes the spin-induced quadrupole moment values predicted for various binary black hole mimicker models [193, 273]. Priors on the dimensionless spin parameters (component

---

[2] Total mass of $M = 15M_\odot$ in the detector frame will corresponds to $M \sim 13.8M_\odot$ in the source frame if we assume the luminosity distance to source to be 400 Mpc.

spins) are chosen such that their magnitudes are uniform in [0, 1] and their directions are isotropically distributed. Component mass priors are uniform in [4, 100]$M_\odot$. Further, all the injections are non-precessing (*i.e.,* aligned or anti-aligned spins) whereas the recovery waveform models account for precession effects.

Network configuration: Throughout our studies, we consider a three-detector network (HLV) which includes two advanced LIGO detectors at Hanford (H) and Livingston (L) [311–313] and advanced Virgo detector (V) [314, 315], assuming both LIGO and Virgo at their design sensitivities given by references [316] and [314, 317], respectively.

Zero-noise injections: Injections are generated using the `lalsim-inspiral` library available in the LSC Algorithm Library [303] with `IMRPhenomPv2` as the waveform approximant. For all the injections, we assume noise realizations to be zero (zero-noise injections) in order to avoid biases in the parameter estimates introduced by a particular noise realization. Results from a zero-noise realization is equivalent to results averaged over many realizations of zero-mean random noise. A noise realization is not to be confused with the noise PSD $S_n(f)$ which appears in the likelihood integral (see Eq. (1.14)) which is always used while computing the relevant quantities.

Other details: For the *LALInference* analysis, we use a sensitive lower cut-off frequency of f_{lower} =20Hz for all three detectors. The upper cut-off frequency f_{upper} of the integral in Eq. (1.14) is chosen as the inspiral-to-merger transition frequency of the IMRPhenomPv2 waveform which is related to the total mass of the system through the relation $M\,f_{\text{upper}} = 0.018$ [13], as described earlier.

4.3.2 Bounds on $\delta\kappa_s$ parameter

Fig. 4.1 shows the posterior probability distributions of $\delta\kappa_s$ parameter obtained from the various simulations. The first row corresponds to component masses (7.5, 7.5)$M_\odot$ (mass ratio = 1) and the second row corresponds to component masses (10, 5)$M_\odot$ (mass ratio = 2). In each row, the four different columns correspond to four spin magnitudes (0.2, 0.1), (0.4, 0.3), (0.6, 0.3) and (0.9, 0.8) from left to right. The different colors represent different injected spin orientations: both the spins aligned (light blue) and both spins anti-aligned (orange) to the orbital angular momentum axis. The dashed vertical lines are the 90% credible bounds following the respective colors of the histograms. Recall

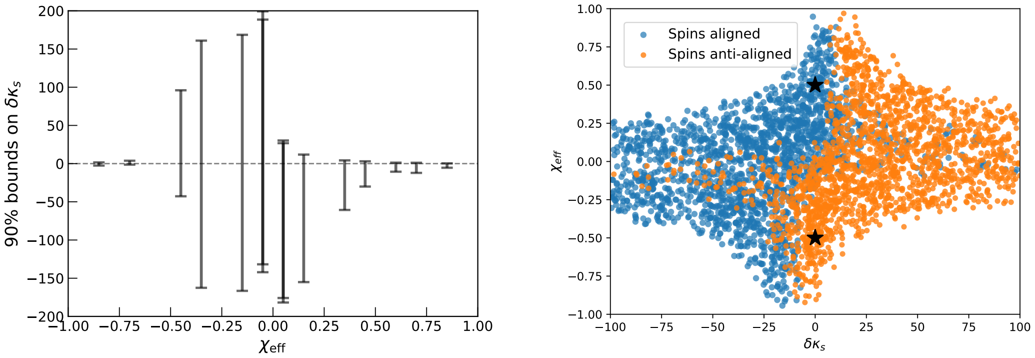

FIGURE 4.2: **Left:** The 90% bounds on the spin-induced quadrupole moment parameter ($\delta\kappa_s$) given in Eq. (4.4) as a function of the injected values of effective spin parameter (see Eq. (4.7)). All the injections are compact binary inspirals with fixed total mass of $15 M_\odot$ while varying the mass ratio, spin magnitudes and orientations which results in different values of effective spin parameter. **Right:** Figure showing the degenerate regions in the non-BH parameter space ($\delta\kappa_s - \chi_{\mathrm{eff}}$) for binary black hole injections with two different spin orientations aligned (0.6, 0.3) and anti-aligned (-0.6, -0.3). The light blue and orange represent aligned and anti-aligned cases respectively and the injected parameters are marked by black stars. The scattered points show the region at which the non-BH waveform has a very high overlap ($\mathcal{O} > 0.995$) with the BH injection(s) (See Eq. (4.8)).

that the bounds are estimated as the highest density intervals of the posteriors as defined in Eq. (4.4).

It is evident from Fig. 4.1 that the bounds on $\delta\kappa_s$ are stronger when the spin magnitudes are larger (see the panels from left to right together with their narrowing axis range). This is expected because, for larger spin magnitudes, the waveform has stronger signatures of spin-induced quadrupole moments (see Eq. (4.2)) which in turn improves the measurement.

Though all the posteriors in Fig. 4.1 peak at their injected values ($\delta\kappa_s = 0$), we notice that there is skewness in all the posteriors about their injected values. This skewness gets mirror-reflected when the spin orientation is reversed. In other words, comparing the light blue and orange histograms in each panel, one notices that the longer tail for light blue is towards left-hand side while for orange, it is towards the right-hand side. This indicates that our ability to constrain the non-BH nature is different for aligned and anti-aligned spin orientations. For aligned cases, the type of non-BH nature with $\delta\kappa_s > 0$ (such as binaries of boson stars) can be better constrained than the type of non-BH nature with $\delta\kappa_s < 0$ (such as binaries of gravastars). On the other hand, for anti-aligned cases, it is vice versa. We investigate these features in detail below.

4.3.2.1 Role of effective spin parameter

We find that the effective spin parameter $\chi_{\rm eff}$ plays a major role in the features observed in the posteriors discussed above. Effective spin parameter defined as

$$\chi_{\rm eff} = \frac{m_1\,\chi_{1z} + m_2\,\chi_{2z}}{(m_1 + m_2)}, \tag{4.7}$$

is a combination of component masses m_1, m_2 and component spins χ_{1z}, χ_{2z} and appears as the leading order spin dependence in the inspiral PN waveform [309]. In Fig. 4.2 (left panel), we have shown the bounds on $\delta\kappa_s$ parameter as a function of their injected $\chi_{\rm eff}$ values where the vertical bars correspond to the 90% credible intervals of the $\delta\kappa_s$ parameter. The larger the magnitude of $\chi_{\rm eff}$, the tighter the bounds on $\delta\kappa_s$. For systems with small magnitudes of $\chi_{\rm eff}$ (for example, $\chi_{\rm eff} < 0.3$), the $\delta\kappa_s$ parameter is almost unconstrained. Further, when $\chi_{\rm eff}$ is large and positive, the region with $\delta\kappa_s > 0$ is better constrained, whereas when the $\chi_{\rm eff}$ is large and negative, the region with $\delta\kappa_s < 0$ is better constrained.

The dependence of $\delta\kappa_s$ posteriors on $\chi_{\rm eff}$ discussed above holds true despite the fact that the systems considered for this plot include those with various component masses and spins. In fact, it is difficult to disentangle the individual effects of the component masses and spins due to the degeneracy between spins and mass ratio parameters [318]. However, $\chi_{\rm eff}$ captures the combined effects of all these parameters on the $\delta\kappa_s$ posteriors and hence is the most important single parameter which describes our ability to constrain $\delta\kappa_s$ parameter for any given system.

We further investigate the skewness of the posteriors in detail and show that they are primarily caused by the waveform degeneracies between $\delta\kappa_s$ and $\chi_{\rm eff}$ parameters. To demonstrate this, we first define the overlap function $\mathcal{O}$ between a binary black hole injection $\tilde{h}^{\rm BH}$ and a non-BH template $\tilde{h}^{\rm NBH}$ as,

$$\mathcal{O} = \frac{\left(\tilde{h}^{\rm BH}|\tilde{h}^{\rm NBH}\right)}{\sqrt{\left(\tilde{h}^{\rm BH}|\tilde{h}^{\rm BH}\right)\left(\tilde{h}^{\rm NBH}|\tilde{h}^{\rm NBH}\right)}} \tag{4.8}$$

where $(.|.)$ is the noise weighted inner product defined in Eq. (1.14) and both $\tilde{h}^{\rm BH}$ and $\tilde{h}^{\rm NBH}$ are in frequency domain. Overlap quantifies how similar are the two signals $\tilde{h}^{\rm BH}$ and $\tilde{h}^{\rm NBH}$ and its value is maximum ($\mathcal{O} = 1$) when $\tilde{h}^{\rm BH} = \tilde{h}^{\rm NBH}$.

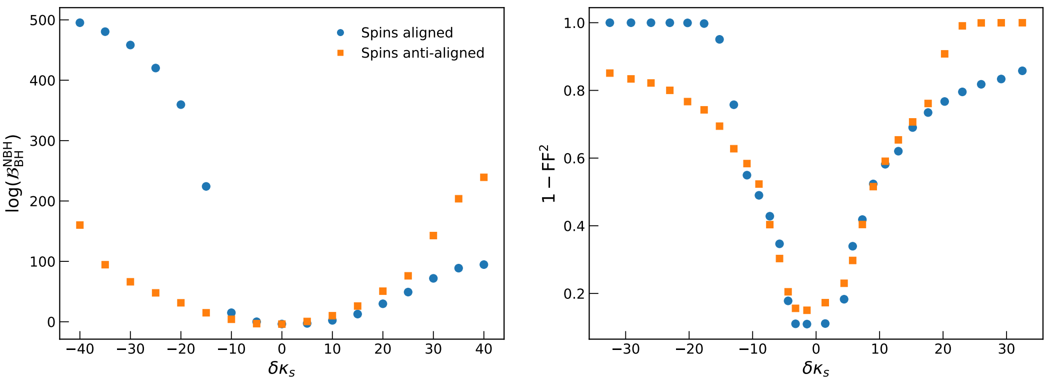

FIGURE 4.3: **Left:** Demonstration of Bayes factor between non-BH and BH models for different non-BH injections. The x-axis shows the injected value of $\delta\kappa_s$ and y-axis shows the log of Bayes factors. All the injections are of component masses $(10+5)M_\odot$ and fixed spin magnitudes $(0.6, 0.3)$ while the light blue and orange markers correspond to aligned and anti-aligned spin orientations respectively. **Right:** Complementary analysis done using *fitting factors* motivated by [9]. For each non-BH injection with values of $\delta\kappa_s$ as given on x-axis, the *fitting factor* FF was computed *w.r.t* the BH waveforms by maximizing the overlap over the BH parameter space. Here the maximization is done on a restricted BH parameter space with $\chi_{\rm eff}$ being the only free parameter, with the remaining parameters fixed to their injected values. The quantity on y-axis is $1-\mathsf{FF}^2$ which explicitly appears in the approximate scheme of [9] (See Eq. (4.10))

We have taken two binary black hole injections with both of them having identical component masses $(10, 5)M_\odot$ but different spin orientations (0.6, 0.3) and (-0.6, -0.3) whose $\chi_{\rm eff}$ values are 0.5 and -0.5 respectively. The templates $\tilde{h}^{\mathrm{NBH}}$ are uniformly distributed in the non-BH parameter space with component spins ranging in [-1, 1] and $\delta\kappa_s$ ranging between [-100, 100]. The masses of the templates are kept fixed at their injection values which will be justified later with the results.

We show the results of this overlap calculation in the right panel of Fig. 4.2. Templates having very high overlaps with the injections ($\mathcal{O} > 0.995$) are shown as scattered points in the $\delta\kappa_s - \chi_{\rm eff}$ plane (light blue for aligned-spin injection and orange for anti-aligned spin injection). The injected parameters are marked with stars (black color). For the aligned spin case (light blue), there are more scattered points on the left half ($\delta\kappa_s < 0$) compared to the right half ($\delta\kappa_s > 0$). This indicates that the left half is more degenerate and hence less distinguishable from the injected binary black hole signal, compared to the right half. This is exactly the feature observed in the posteriors as well as the bar plot (Fig. 4.1 and Fig. 4.2 left) that for systems with aligned spins (or $\chi_{\rm eff} > 0$), the positive side of the $\delta\kappa_s$ posterior is better constrained than the negative side. A similar explanation holds for the anti-aligned spin case as well with all the features turned exactly opposite.

The fact that the masses of the templates are fixed to the injected values might be considered as ignoring some of the other potential degeneracies which are present. However, ignoring the role of such degeneracies can be justified since we have shown above that the $\delta\kappa_s - \chi_{\rm eff}$ degeneracies could solely explain the features of the posteriors. In other words, the overlap study with masses fixed to the injections helps underline that it is the $\delta\kappa_s - \chi_{\rm eff}$ degeneracy which is primarily responsible for the features of the posteriors.

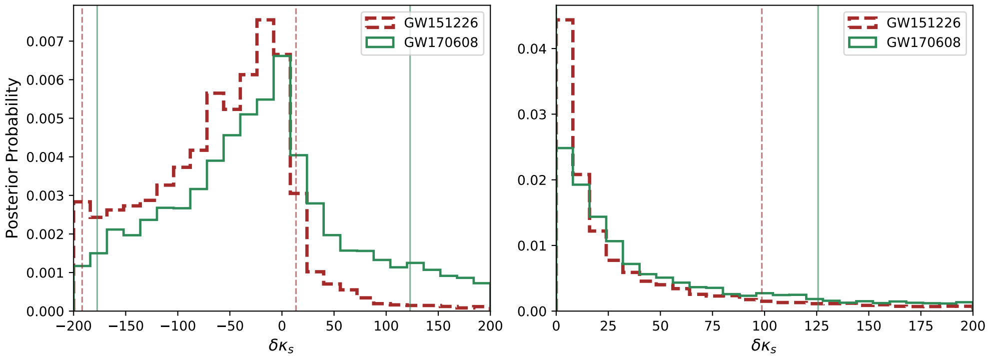

FIGURE 4.4: Posterior distributions on the spin-induced quadrupole moment parameter $\delta\kappa_s$, estimated from the observed gravitational wave events GW151226 [10] and GW170608 [11]. Left and right panels correspond to two different physically motivated priors on $\delta\kappa_s$ parameter (symmetric and one-sided). The posteriors are obtained from the Bayesian analysis of the O1/O2 public GW data using *LALInference* [12]. We used `IMRPhenomPv2` waveform models [13] for the analysis, truncated at the inspiral-to-merger transition frequency as the spin-induced deformations are not modelled in the merger and ringdown phases. The vertical dotted lines show the 90% credible bounds (highest density intervals) on $\delta\kappa_s$.

4.3.3 Model selection between BH and non-BH models

In this section, we discuss the model selection studies between non-BH and BH models by obtaining Bayes factors between them. We estimate the Bayes factors $\mathcal{B}_1^2$ (see Eq. (4.6)) using *LALInference* for a set of non-BH injections whose $\delta\kappa_s$ varies in the range [-40, 40]. All the injections are of fixed component masses (10, 5)$M_\odot$ while the analysis is repeated with two spin choices for the injections: (0.6, 0.3) and (-0.6, -0.3), which as followed in the previous section, represents the aligned and anti-aligned orientations respectively.

The results are shown in the left panel of Fig. 4.3 where the log of the Bayes factors ($\log \mathcal{B}_1^2$) are plotted as a function of the injected $\delta\kappa_s$ values. The light blue and orange colors correspond to aligned and anti-aligned spins respectively. As one would expect, when the magnitude of the injected $\delta\kappa_s$ increases, the Bayes factor increases which mean that they can be better distinguished from binary black hole models. We notice that the way Bayes factor increases with $\delta\kappa_s$ is different for aligned and anti-aligned cases. For example, among all the injections with $\delta\kappa_s > 0$ (such as binaries of boson stars), Bayes factors are larger for those whose spins are anti-aligned (or negative $\chi_{\rm eff}$) compared to those whose spins are aligned (or positive $\chi_{\rm eff}$). The reverse is true for the injections with $\delta\kappa_s < 0$ (such as binaries of gravastars).

The features discussed above can have possible consequences on the identification of BH mimicker populations. For example, among the population of boson star binaries, our ability to distinguish them from binary black holes will be inclined towards those with anti-aligned spins. As a result, the population which we identify as binary boson stars will have more sources with anti-aligned spins (or negative $\chi_{\rm eff}$). Similarly, the population which we identify as binary gravastars will have more sources with aligned spins (or positive $\chi_{\rm eff}$).

4.3.3.1 Further investigations using Fitting Factor

In order to investigate various features in the Bayes factor plot (Fig. 4.3, left panel), we perform a study using *fitting factor* to complement the Bayesian analysis. The *fitting factor* of a non-BH waveform $\tilde{h}^{\rm NBH}$, with a BH waveform model $\tilde{h}^{\rm BH}$ is given by,

$$\mathsf{FF}(\overrightarrow{\theta}_{\rm NBH}) = \max_{\overrightarrow{\theta}_{\rm BH}} \left(\frac{\left(\tilde{\mathsf{h}}^{\rm NBH}|\tilde{\mathsf{h}}^{\rm BH}(\overrightarrow{\theta}_{\rm BH})\right)}{\sqrt{\left(\tilde{\mathsf{h}}^{\rm NBH}|\tilde{\mathsf{h}}^{\rm NBH}\right)\left(\tilde{\mathsf{h}}^{\rm BH}(\overrightarrow{\theta}_{\rm BH})|\tilde{\mathsf{h}}^{\rm BH}(\overrightarrow{\theta}_{\rm BH})\right)}} \right) \tag{4.9}$$

where $\tilde{h}^{\rm NBH}$ is evaluated at a given point $\overrightarrow{\theta}_{\rm NBH}$ in the non-BH parameter space and $\overrightarrow{\theta}_{\rm BH}$ is any arbitrary point in the BH parameter space over which the maximisation is carried out. One can see from Eq. (4.9) that $\mathsf{FF}(\overrightarrow{\theta}_{\rm NBH})$ is equal to the *overlap*, defined in Eq. (4.8), maximised over the BH parameter space. Qualitatively, $\mathsf{FF}(\overrightarrow{\theta}_{\rm NBH})$ is regarded as a measure of how well the BH waveform model $\tilde{h}^{\rm BH}$ can mimic the given non-BH signal $\tilde{h}^{\rm NBH}(\overrightarrow{\theta}_{\rm NBH})$. In other words, $\mathsf{FF}(\overrightarrow{\theta}_{\rm NBH})$ describes how well the non-BH corrections contained in $\tilde{h}^{\rm NBH}(\overrightarrow{\theta}_{\rm NBH})$ can be re-absorbed[3] into the BH waveform $\tilde{h}^{\rm BH}(\overrightarrow{\theta}_{\rm BH})$, by varying $\overrightarrow{\theta}_{\rm BH}$ within its allowed range.

---

[3] We closely follow the terminology used by Vallisneri [9] here.

As discussed before, the Bayes factor $\mathcal{B}_1^2$ for a given signal is high when the signal has a non-BH component of the form that can not be re-absorbed into the BH waveform. Broadly this implies that a high Bayes factor is closely related to a low *fitting factor*. Cornish et al. [319] and Vallisneriet al. [9] showed an approximate scheme to relate the Bayes factor and *fitting factor* which, for our context (considering only the dominant term in the expression) would read as,

$$\log \mathcal{B}_1^2 \propto \rho^2 \times \left(1 - \mathsf{FF}(\overrightarrow{\theta}_{\rm NBH})^2\right) \tag{4.10}$$

where ρ is the signal-to-noise ratio. In a later work, Del Pozzo et al. [320] explored this in more detail using numerical simulations and extended its validity regimes by introducing additional correction terms.

In this exercise, we consider a set of non-BH injections similar to the ones considered in the Bayes factor studies above. For all the injections, we compute $\mathsf{FF}(\overrightarrow{\theta}_{\rm NBH})$ using Eq. (4.9) for a binary system of masses (10, 5)$M_\odot$. Note that in our case the BH parameter space ($\overrightarrow{\theta}_{\rm BH}$) over which the maximization is done has only one free parameter which is the effective spin $\chi_{\rm eff}$, while all other parameters are fixed to their injected values as our goal is to understand the ability of $\chi_{\rm eff}$ to mimic non-BH signals.

The results are shown in the right panel of Fig. 4.3 where $1 - \mathsf{FF}(\overrightarrow{\theta}_{\rm NBH})^2$ (which explicitly appears in Eq. i(4.10)) is plotted as a function of the injected $\delta\kappa_s$. We find similar features as seen in the Bayes factor plot (left panel). For example, for non-BH injections with $\delta\kappa_s > 0$, the value of $(1-\mathsf{FF}^2)$ is higher for anti-aligned cases (or negative $\chi_{\rm eff}$ cases) while it is the opposite for those injections which have $\delta\kappa_s < 0$. That means the results independently obtained from the Bayes factor and the *fitting factor* analyses are complementary to each other. We emphasize again that this agreement holds despite restricting the BH parameter space to just one parameter, $\chi_{\rm eff}$.

Thus, the *fitting factor* analysis further underscores the key role played by the $\chi_{\rm eff}$-$\delta\kappa_s$ degeneracy in distinguishing non-BH binaries from BH binaries.

Notice that when the non-BH signals are mimicked by the BH waveforms, it happens at the cost of offsets in the estimated BH parameters from their true values. In realistic cases, this will result in systematic biases in the estimated BH parameters, if BH waveforms are used for the analysis while the true signal was of a non-BH binary. It is worth mentioning the two contexts in which this can happen. 1) if one presumes the signal to be of BH nature and hence ignore the possibility of any potential non-BH nature. 2) one does not assume BH nature a priori, however, given the SNR of the signal, the non-BH component in the signal is mild enough to be reabsorbed into the BH waveform by varying the parameters. Though both the biases are fundamental in nature [89, 319], the former is also the result of our prior assumption while the latter is the result of our waveform models being insufficient to account for the underlying non-BH effects or/and the non-BH effects being buried in noise. In a follow-up work, these effects will be investigated in detail.

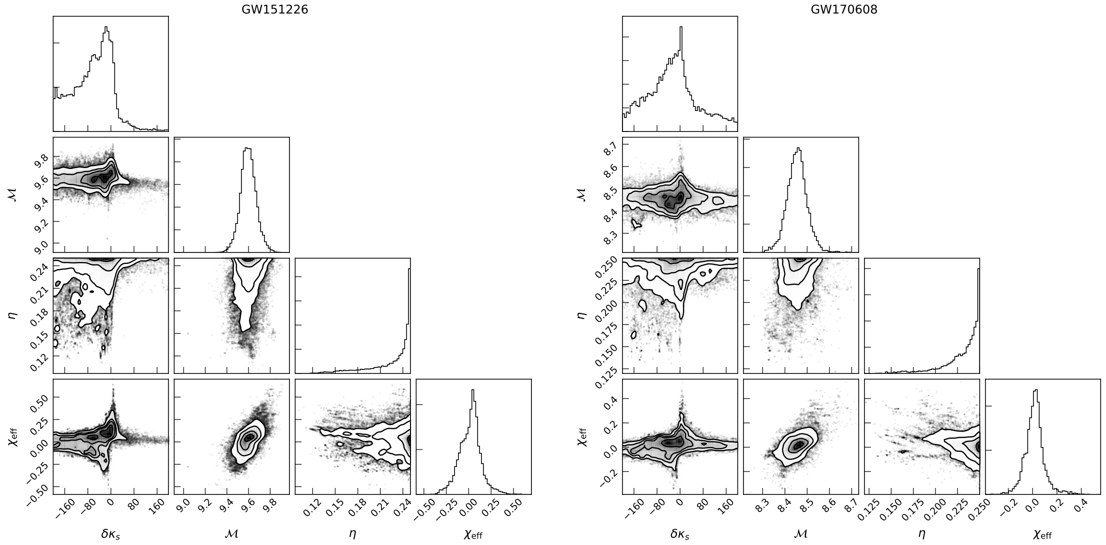

FIGURE 4.5: The corner plots of $\delta\kappa_s$, chirp mass (M_c), symmetric mass ratio (η) and $\chi_{\rm eff}$ from GW151226 [10] and GW170608 [11] with symmetric priors on $\delta\kappa_s$.

4.4 Testing the binary black hole nature of GW151226 and GW170608

As reported in [14], the first two observation runs (O1/O2) of Advanced LIGO and Advanced Virgo have identified ten gravitational wave signals which are consistent with binary black hole waveforms. In this section, we apply the proposed spin-induced quadrupole moment test on some of the observed events and ask how consistent they are to the binary black hole hypothesis. As discussed before, at present, our test is based on a parametrization of the inspiral part of the waveform. Therefore, we restrict the study to the two inspiral-dominated signals GW151226 [10] and GW170608 [11], where the inspiral only signal to noise ratio (obtained by considering only Fourier frequencies less than the ISCO) is ~ 10. The estimated (median) detector frame total mass of GW151226 and GW170608 are $23.55 M_\odot$ and $19.89 M_\odot$ [321] and the corresponding inspiral-to-merger transition frequencies are 155.12Hz and 184.55Hz respectively. We use

Event	**Prior on $\delta\kappa_s$**	**90% bounds on $\delta\kappa_s$**	**Bayes factor ($\log \mathcal{B}_{BH}^{generic}$)**
GW151226	[-200,200]	[-191.78, 13.45]	-0.94
	[0,200]	$\leq$ 98.67	-2.26
GW170608	[-200,200]	[-177.36, 122.98]	-0.15
	[0,200]	$\leq$ 125.69	-1.15

Table 4.1: Summary of the tests of binary black hole nature of the real gravitational wave events GW151226 and GW170608 by measuring the spin-induced quadrupole moment parameters $\delta\kappa_s$. The results are shown for two different physically motivated priors on $\delta\kappa_s$: [-200, 200] (symmetric) and [0,200] (one-sided) as shown in the second column. The third and fourth columns respectively show the 90% credible intervals (upper bounds in case of one-sided priors) on $\delta\kappa_s$ and the Bayes factors between non-BH and BH models.

these as the upper cut-off frequencies ($f_{\rm upper}$) of the analyses along with `IMRPhenomPv2` as the waveform approximant.

Here we briefly summarize the results from the tests of binary black hole nature of the observed GW signals GW151226 [10] and GW170608 [15]. Among all the ten binary black hole events detected in O1/O2, we have restricted the analysis for these two events. This is because, with the currently available waveform models, our test is applicable only on the inspiral part of the signal and GW151226 and GW170608 are the only two inspiral dominated events.

Figure 4.4 shows the bounds obtained from GW151226 [10] (red) and GW170608 [11] (green). We show the posterior probability distribution for $\delta\kappa_s$, the parametrized deformations in the κ_s parameter, which is the symmetric combination of spin-induced quadrupole moment coefficients of the individual compact objects (κ_1 and κ_2).In the left panel, we used a generic prior on $\delta\kappa_s$, as uniform in [-200,200], which leads to constraints on generic BH mimicker models which has positive or negative values for $\delta\kappa_s$. Under this prior assumption, we find that the deformation parameter $\delta\kappa_s$ is constrained to a 90% credible interval of [-191.78, 13.45] for GW151226 and [-177.36, 122.98] for GW170608. In the right panel, we have obtained the bounds on $\delta\kappa_s$ for a restricted one-sided prior of [0, 200]. Unlike the generic prior, this one-sided prior leads to constraints on specific black hole mimicker models such as boson stars for which $\delta\kappa_s$ is predicted to be positive always. Under this prior assumption, we obtain 90% credible upper bounds to be $\delta\kappa_s \leq 98.67$ for GW151226 and $\delta\kappa_s \leq 125.69$ for GW170608. All the bounds are listed in Table 4.1. In all the cases, it is noted that the BH limits ($\delta\kappa_s = 0$) are well within the 90% credible intervals which means that the posteriors do not indicate the presence of any non-BH nature in these events. However, one may also note that the posteriors are not very sharply peaked at zero implying weaker constraints on the non-BH nature of the compact objects involved.

In addition to the bounds reported above, we performed Bayesian model selection between BH mimicker models and BH models by calculating the Bayes factor between them (defined in Sec. 4.2.3). The estimated Bayes factors for both the events are given in Table 4.1. For these events, we find that the Bayes factors in the logarithmic scale are -0.94 (for GW151226) and -0.15 (for GW170608) which implies that Bayes factors do not show strong evidence in favor of any of the models (neither BH nor non-BH models). These results are in agreement with our conclusions from the posteriors discussed above. Only more sensitive measurements in the future may help us quantify this better.

The main results are shown in Fig. 4.4 where the posteriors on $\delta\kappa_s$ parameter are discussed We consider two different priors on $\delta\kappa_s$: a symmetric prior $[-200, 200]$ (left panel) and a one-sided prior $[0, 200]$ (right panel). The symmetric prior [-200,200] represents a most generic test which accounts for BH mimicker models including those of both oblate ($\delta\kappa_s > 0$) and prolate ($\delta\kappa_s < 0$) spin-induced deformations. The one-sided prior [0,200] is a restricted case which accounts only for oblate spin-induced deformations. In other words, the symmetric prior leads to generic constraints on BH mimicker models including boson stars, gravastars *etc.* whereas the one-sided prior is motivated by specific models such as boson star models for which $\delta\kappa_s$ is always positive and hence meant to provide specific constraints on such models. The prior is restricted to $|\delta\kappa_s| \leq 200$ because the parametrized waveforms we construct are found not to be well-behaved beyond this range and hence cannot meaningfully represent the corresponding physics. The 90% credible intervals (highest density intervals) on $\delta\kappa_s$ are given in Table 4.1. For all the cases, it is found that the 90% credible intervals or the upper bounds (in case of one-sided prior) are consistent with $\delta\kappa_s$ being equal to zero and hence consistent with GW151226 and GW170608 being binary black holes.

Detailed corner plots are presented in Fig. 4.5 which will help us to gain further insights about the underlying degeneracies and correlations. As we discussed earlier, the $\delta\kappa_s$ parameter is found to be highly degenerate with $\chi_{\rm eff}$. Again, we note that the posteriors of $\delta\kappa_s$ are asymmetric about their most probable values and both the events have got more posterior support for negative values of $\delta\kappa_s$ than positive values. We recall from Fig. 4.1 and 4.2 that the similar posterior features were observed for cases in which positive values of $\chi_{\rm eff}$ were injected. As seen in the corner plots, the estimated (median) χ_{eff} values are positive for both these events and hence the results from these two events are completely consistent with our findings from simulation studies. It is also found that the $\delta\kappa_s$ posteriors are railing against the prior boundaries for both the events. This may improve in future if there are events which have larger spins or lower masses, similar to the ones considered in the simulations earlier.

We also performed Bayes factor studies on both the events whose results are also shown in Table 4.1. With the symmetric and the one-sided priors on $\delta\kappa_s$, we computed Bayes factors ($\mathcal{B}_1^2$) between the non-BH and BH models ($\mathcal{H}_{non-BH}$ and $\mathcal{H}_{BH}$ respectively). We find that the log of the Bayes factors ($\log \mathcal{B}_1^2$) are in the range $-2.3 < \log \mathcal{B}_1^2 < 0$ for all the cases. These values are too small to be considered as evidence for favoring or rejecting any of the models which are tested. The slightly negative values obtained in all the cases may be interpreted as weak evidence in favor of BH models over non-BH models. We notice that these features are consistent with those observed in the posteriors in Fig. 4.4 that the posteriors are spread over a wider range of values of $\delta\kappa_s$ with significant weights over non-BH (*i.e.* non-zero) values.

4.5 Conclusions

Here, we have developed a Bayesian framework to test the binary black hole nature of gravitational wave signals using the measurements of spin-induced quadrupole moment parameters of the compact binaries as proposed in Ref. [302]. We carried out detailed studies using simulated gravitational wave signals to test the applicability of our method. The waveform models which are used for this test currently includes spin-induced deformation terms only in the inspiral part and hence its applicability is limited to the inspiral regime.

We applied the method on the two inspiral-dominated events from O1/O2, GW151226 and GW170608, and obtained bounds on their binary blackhole natures. These are the first constraints on the black hole nature of the compact binaries detected by Advanced LIGO and Advanced Virgo. With more gravitational wave detections with inspiral-dominated signals, especially of higher spins, there will be increased opportunity to perform the tests of BH nature using spin-induced quadrupole moment parameter measurements. The bounds obtained from this analysis on the spin-induced quadrupole moment parameter can be translated to constraints on the parameter space of certain black hole mimicker models such as the boson star model in Ref. [193].

In the next chapter (Sec. 5.2), we extend the analysis given in chapter 3 to demonstrate the capabilities of third-generation (3G) gravitational wave detectors such as Einstein telescope [322] and Cosmic Explorer [322–325], to test the binary black hole nature by measuring the spin-induced *multipole* moment parameters. Further, in certain regions of binary black hole parameter space, it gives the ability to measure the spin-induced quadrupole moment parameters of the individual constituents of the binary, rather than measuring the symmetric combination defined above. This study is further extended to the case of space-based detectors LISA and DECIGO and described in Sec. 5.3 and it is found that they offer unprecedented opportunity to test the black hole nature of compact binaries in the intermediate-mass and super-massive mass regimes.

Chapter 5

Measurements of spin-induced multipole moments and implications to future gravitational wave detectors

5.1 Introduction

In chapter 3, we explored the possibility of probing the binary black hole nature of coalescing compact binaries, by measuring their spin-induced multipole moments, observed in advanced LIGO detectors. Coefficients characterizing the spin-induced multipole moments of Kerr black holes are predicted by the "no-hair" conjecture and appear in the gravitational waveforms through quadratic and higher order spin interactions and hence can be directly measured from gravitational wave observations. In this chapter, we assess the capabilities of future third-generation ground-based detectors such as Cosmic Explorer and Einstein Telescope as well as the space-based detectors LISA and DECIGO. Third generation ground-based detectors would be able to constrain the black hole nature of stellar mass compact binaries ($\sim 10 - 100 M_{\odot}$), whereas the space-based DECIGO mission will be sensitive to intermediate mass BHs ($\sim 10^5 - 10^7 M_{\odot}$). The LISA mission will be able to put stringent constraints on the black hole nature fo supermassive compact binaries.

In the first section of this chapter, by employing a non-precessing post-Newtonian (PN) waveform model, we assess the capabilities of the third-generation gravitational wave interferometers such as Cosmic Explorer and Einstein Telescope in carrying out such measurements and use them to test the binary black hole nature of observed binaries. More than this, we extend the investigations given in Chap. 3, limited to measuring the binary's spin-induced quadrupole moment using their observation in *second* generation detectors, by proposing to measure (a) spin-induced *quadrupole* effects using *third* generation detectors, (b) *simultaneous* measurements of spin-induced *quadrupole* and *octupole* effects, again in the context of the third-generation detectors. We study how precision of these measurements as a function of total mass, mass ratio, spin magnitudes, and spin alignments. Further, we consider two different binary black hole populations, as proxies of the population that will be observed by the third generation detectors, and obtain the resulting distribution of the spin-induced quadrupole coefficient. This helps us assess how common are those cases where this test would provide very stringent constraints on the black hole nature. These error bars provide us upper limits on the values of the coefficients that characterize the spin-induced multipoles. We find that, using third-generation detectors the symmetric combination of coefficients associated with the spin-induced quadrupole moment of each binary component may be constrained to a value ≤ 1.1 while a similar combination of coefficients for spin-induced octupole moment may be constrained to ≤ 2, where both combinations take the value of 1 for a binary black hole system. These estimates suggest that third-generation detectors can accurately measure the first four multipole moments of the compact objects (mass, spin, quadrupole, and octupole) facilitating a thorough probe of their black hole nature.

In the second part of this chapter, we apply the idea proposed in Chapter 3 (Ref. [302]) to binary systems composed of supermassive and intermediate-mass black holes and derive the expected bounds on their Kerr nature using future space-based gravitational wave detectors. Using astrophysical models of binary black hole population, we study the measurability of the spin-induced quadrupole and octupole moment coefficients using LISA and DECIGO. The errors on spin-induced quadrupole moment parameter of the binary system is found to be ≤ 1 for almost 40% of the total supermassive binary black hole population which is detectable by LISA whereas it is $\sim 92\%$ for the intermediate-mass black hole binaries observable by DECIGO at its design sensitivity. We find that *both* the quadrupole and octupole moment parameters can be estimated to a precision of ≤ 1 for $\sim 2\%$ and $\sim 50\%$ respectively for LISA and DECIGO detectors. Our findings show that there exists a subpopulation of binary black hole events detectable by DECIGO which could permit tests of black hole nature to 1% precision.

5.2 Details of the analysis

5.2.1 Spin-induced quadrupole and octupole moment parameters in the post-Newtonian waveform

The waveform we use for our analyses contain only the leading (second) harmonic (quadrupolar mode) and its PN corrections in the amplitude, while the presence of higher modes in the waveform is neglected, and schematically reads as,

$$\tilde{h}(f) = \frac{M^2}{D_L}\sqrt{\frac{5\,\pi\,\nu}{48}}\sum_{n=0}^{4} V_2^{n-7/2}\, C_2^{(n)}\, \mathrm{e}^{\mathrm{i}\left(2\,\Psi_{\mathrm{SPA}}(f/2)-\pi/4\right)}\,, \tag{5.1}$$

where M, ν and D_L denote the total mass, symmetric mass-ratio and the luminosity distance to the binary system respectively as described after Eq 15. Coefficients $C_2^{(n)}$ represent the amplitude corrections to the quadrupolar harmonic at (n/2) PN order [304]. The pre-factor V_2 related to the gravitational wave frequency (f) and the total mass of the binary system as, $V_2 = (\pi\, M\, f)^{1/3}$. Here $\Psi_{\mathrm{SPA}}(f)$ represents the phase of the waveform. Each of these $C_2^{(n)}$ and the phasing, with explicit dependence on spin-induced quadrupole (through κ_s and κ_a) and octupole (through λ_s and λ_a) moment parameters at respective PN orders are given in Appendix A.

5.2.2 Parameter estimation and detector configurations

In this section, we present the necessary details of the parameter estimation scheme and the analysis (more details can be found in the introduction of the thesis 1.3.2). Our aim here is to obtain the projected bounds on the spin-induced multipole moment parameters using the semi-analytical parameter estimation technique called the Fisher information matrix [58]. As we discussed in Sec. 1.4, the Fisher information matrix [310, 326, 327] approach is a semi-analytical parameter estimation technique which can be used to compute the 1σ error bars on parameters characterizing the gravitational wave signal. The elements of the matrix are defined as follows,

$$\Gamma_{ij} = 2\int_{f_{\mathrm{lower}}}^{f_{\mathrm{upper}}} \left(\partial_i\tilde{h}(f)\,\partial_j\tilde{h}^*(f) + \partial_i\tilde{h}^*(f)\,\partial_j\tilde{h}(f)\right)\frac{df}{S_n(f)}\,, \tag{5.2}$$

where we denote the frequency domain gravitational waveform as $\tilde{h}(f)$ and its partial derivative with respect to the i^{th} parameter characterising the binary system as $\partial_i\tilde{h}(f)$

(here, $\partial_i\tilde{h}^*(f)$ is the conjugate of $\partial_i\tilde{h}(f)$). The $1-\sigma$ error bars on each parameter are computed as $\Delta\overrightarrow{\theta} = \sqrt{\Gamma_{ii}^{-1}}$, under the assumption that the noise in the detector is stationary and Gaussian, and also in the high signal-to-noise ratio limit [326].

In Sec. 5.3, we intend to explore the parameter estimation analysis for two different third-generation gravitational wave detector configurations: Cosmic Explorer (CE) [4, 5] and Einstein Telescope (ET-D) [5]. We choose to terminate the integral of Eq. ((5.2)) at twice the orbital frequency of the inner most stable circular orbit ($f_{\rm ISCO}$) for a *spinning* compact binary and use the fits obtained in [13, 296][1]. The lower frequency cut-off in the integral of Eq. ((5.2)) is fixed by the sensitivity of the detector given by the function $S_n(f)$. Since the two have comparable sensitivities and we choose one of them (in our case CE noise PSD) for the most part of the analysis here. However, we compare the performance of CE and ET-D for a few representative cases. The low frequency cut-off for CE (ET-D) configuration is chosen to be 5Hz (1Hz) which defines the $f_{\rm low}$ value we use in the integral given in Eq. ((1.10)). We also discuss the improvements one expect due to the use of third-generation detector sensitivities over advanced LIGO and choose low frequency cut-off as 20 Hz for advanced LIGO.

We investigate the measurability of spin-induced quadrupole and octupole moment parameters of supermassive and intermediate-mass binary black holes in Sec. 5.4 using LISA and DECIGO detector configurations. The noise spectral density used for LISA is given by [8],

$$S_n(f) = \frac{20}{3\,L^2}\left(4\,S_n^{acc}(f) + 2\,S_n^{loc} + S_n^{sn} + S_n^{omn}\right)\left[1 + \left(\frac{2\,L\,f}{0.41c}\right)^2\right] + S_n^{gal}, \tag{5.3}$$

where,

$$S_n^{acc} = \left\{9\times10^{-30} + 3.24\times10^{-28}\left[\left(\frac{3\times10^{-5}\,\mathrm{Hz}}{f}\right)^{10} + \left(\frac{10^{-4}\,\mathrm{Hz}}{f}\right)^2\right]\right\}\frac{1}{(2\,\pi\,f)^4}\,\mathrm{m}^2\,\mathrm{Hz}^{-1},$$

$$S_n^{loc} = 2.89\times10^{-24}\,\mathrm{m}^2\,\mathrm{Hz}^{-1},$$

$$S_n^{sn} = 7.92\times10^{-23}\,\mathrm{m}^2\,\mathrm{Hz}^{-1},$$

---

[1] Here we only consider contributions from the second harmonic as discussed in Sec. 5.2.

$$S_n^{omn} = 4.00 \times 10^{-24}\,\mathrm{m}^2\,\mathrm{Hz}^{-1},$$

$$S_n^{gal} = 1.633 \times 10^{-44} \left(\frac{f}{1\,\mathrm{Hz}}\right)^{-7/3} \exp\left(-\left(\frac{f}{1.426\,\mathrm{mHz}}\right)^{1.183}\right) \left(1 + \tanh\left(-\frac{f - 2.412\,\mathrm{mHz}}{4.835\,\mathrm{mHz}}\right)\right)\,\mathrm{Hz}^{-1},$$

are due to low-frequency acceleration, local interferometer noise, shot noise, other measurement noise and galactic confusion noise, respectively. The detector arm length is fixed to be $L = 2.5 \times 10^9\, m$ and c is the speed of light in meters per second. Noise spectral densities used for DECIGO [6] and DECIGO-B [7] are,

$$\begin{aligned} S_n(f) \;&=\; 7.05 \times 10^{-48}\left(1 + \left(\frac{f}{7.36\,\mathrm{Hz}}\right)^2\right) + 4.8 \times 10^{-51}\left(\frac{f}{1\,\mathrm{Hz}}\right)^{-4}\left(1 + \left(\frac{f}{7.36\,\mathrm{Hz}}\right)^2\right)^{-1} \\ &+\; 5.33 \times 10^{-52}\left(\frac{f}{1\,\mathrm{Hz}}\right)^{-4}\,\mathrm{Hz}^{-1}, \end{aligned} \tag{5.4}$$

and

$$S_n(f) = 3.03 \times 10^{-46}\left(1 + 1.584 \times 10^{-2}\left(\frac{f}{1\,\mathrm{Hz}}\right)^{-4} + 1.584 \times 10^{-3}\left(\frac{f}{1\,\mathrm{Hz}}\right)^2\right)\,\mathrm{Hz}^{-1} \tag{5.5}$$

respectively.

The lower and upper cut-off frequencies (see Eq. (5.2)) for the analysis are fixed using the following relations,

$$\begin{aligned} f_{\mathrm{upper}} &= \min\left(\mathrm{f}_{\mathrm{max}},\, \mathrm{f}_{\mathrm{ISCO}}\right) \\ f_{\mathrm{lower}} &= \max\left(\mathrm{f}_{\mathrm{min}},\, \mathrm{f}_{4\,\mathrm{yr}}\right). \end{aligned}$$

For LISA, we fix f_{max} as 0.1 Hz and f_{min} to be 10^{-4} Hz and for DECIGO the upper cut-off frequency is kept to be 10 Hz throughout the study. To examine the effect of the lower cut-off frequency on different DECIGO configurations, we consider two different scenarios, basic DECIGO or DECIGO-B [7, 134] with a conservative low-frequency cut-off of 10^{-1}Hz(f_1) and DECIGO [6] at its designed sensitivity (which we refer to as DECIGO) with a low-frequency cut-off of 10^{-2}Hz(f_2). As expected, due to the improved sensitivity, bounds obtained from DECIGO are much better than DECIGO-B in general.

To obtain the value of $f_{\rm ISCO}$, which corresponds to the innermost stable circular orbit (ISCO) frequency of Kerr BHs, we use a fitting formula where we provide the mass and spin parameters of the initial configuration (constituents of the binary) and calculate ISCO frequency of the remnant BH in terms of its mass and spin [13, 296, 302, 310]. Our choice of lower cut-off frequency accounts for the fact that the compact binary system spends four years in each of the detector bands. In order to achieve this, we take $f_{4\,\rm yr} = f_{\rm upper}\left(1 + \frac{m_1\, m_2}{(m_1+m_2)^3}\, 6.6 \times 10^4\, \mathsf{T}^{-1}\right)^{-\frac{3}{8}}$, where T is fixed to be $4\,\mathsf{yrs}$ [328].

Left panel of Fig. 1.4 shows the noise PSDs of Adv. LIGO, CE, ET-D, LISA and DECIGO configurations, whereas the right panel shows the variation of signal-to-noise ratios with the total mass of the compact binaries in the respective frequency bands.

5.3 Spin-induced deformations and tests of binary black hole nature using third-generation detectors

It was argued in the previous two Chapters 3 and 4 that it would not be possible to accurately measure the deformability coefficients associated with each binary constituents (κ_1, κ_2) simultaneously due to the inherent degeneracies between them. However, the symmetric combination of the two, $\kappa_s = (\kappa_1 + \kappa_2)/2$, can be measured accurately assuming the anti-symmetric combination is zero (which would mean that we work with the condition $\kappa_1 = \kappa_2$). Since $\kappa_1 = \kappa_2 = 1$ for a Kerr black hole (and hence $\kappa_s = 1$ for a binary black hole), an accurate measurement of κ_s is an excellent test of the binary black hole nature of the observed compact binary. If the binary system comprises of exotic compact objects, the measurement of the symmetric combination κ_s should be sensitive to such a deviation from binary black hole nature even if $\kappa_1 \neq \kappa_2$. However, a further analysis, where both κ_1 and κ_2 are simultaneously measured, will be necessary to further understand the composition of the binary and detailed nature of the binary constituents. This possibility is further discussed in Sec. 5.3.1.4. The error bars associated with the measurement provides the upper limit on the value of κ_s allowed by the data for black hole mimicker models. These bounds, therefore, can be mapped on the parameter space of various black hole mimicker models. A statistically significant detection of $\kappa_s \neq 1$ could be an indication of the presence of exotic physics in play and may be followed up.

In this chapter, we extend the idea explained in Chapters 3 and 5, in *three* ways by utilizing the enhanced sensitivity of third-generation detectors [322, 329]. Firstly, we estimate the errors on κ_s assuming a third-generation noise sensitivity and find that the enhanced sensitivity of third-generation detectors over second-generation detectors improve the κ_s estimates, roughly, by an order of magnitude (see Fig. 5.3). Secondly, we investigate the ability of third-generation detectors to simultaneously measure κ_s and λ_s (symmetric combination of coefficients associated with spin-induced octupole of each binary component (λ_1, λ_2)) while we set the anti-symmetric combinations of each pair of coefficients, (κ_1, κ_2) and (λ_1, λ_2) to zero. This would allow simultaneous measurement of the mass, spin, quadrupole and octupole moments of the source thereby permitting consistency tests between them as tests of the binary black hole nature. Thirdly, we obtain the projected bounds on κ_1 and κ_2 simultaneously using third-generation detectors (keeping the octupole moment coefficients to their BH values). These bounds can straightforwardly be mapped to the black hole nature of the compact object constituting the binary system leading to a much stronger test compared to the one proposed in [302]. In the next section, Sec. 5.3.1, we report the results in detail.

5.3.1 Results and discussions

We perform the parameter estimation analysis for a set of prototypical (stellar mass) compact binary systems with the assumption that the binaries are optimally oriented and are located at a *fiducial* distance of 400 Mpc. The component spin magnitudes are represented by the dimensionless spin parameter, $\chi_{1,2}$, where subscripts 1(2) represents the primary (secondary) binary component. We also follow the convention to assign higher mass and spin values to the primary component. In addition to this, we also obtain a distribution of errors of the spin-induced multipole moment parameters for a simulated population of binary black holes, which act as proxies for the binary black hole population third generation detectors would observe.

As discussed above, we choose to work with the Cosmic Explorer noise PSD as a representative noise sensitivity of a third-generation detector configuration [323–325]. The lower (upper) frequency cut-offs appearing in Eq. ((1.10)) are chosen to be 5Hz ($2 \times f_{\rm ISCO}$ for *spinning* binary black holes [13, 296]). These results are compared with the corresponding ones for advanced LIGO and Einstein Telescope for a selected set of binary configurations.

A summary of our analysis is shown in Fig. 5.1, where the projected errors on the measurement of the spin-induced multipole moments for the three scenarios discussed above are shown as a function of total mass for a fixed mass-ratio of 1.2 and dimensionless

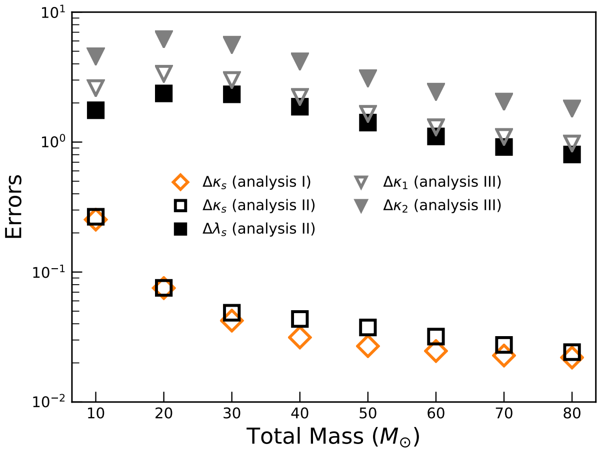

FIGURE 5.1: Figure displays variation of 1-σ errors in the measurement of parameters characterizing spin-induced multipole moments as a function of the total mass of the binary for the three different analyses. **Analysis I** represents the case where $\kappa_s = (\kappa_1 + \kappa_2)/2$ is treated as an independent parameter (here $\kappa_{1,2}$ are parameters characterizing the spin-induced quadrupole moment of each binary component) while the antisymmetric combination of κ_1 and κ_2 as well as the symmetric and antisymmetric combination of parameters characterizing the spin-induced octupole moment, (λ_1, λ_2), are set to their binary black hole values of $(0, 1, 0)$, respectively. In **Analysis II**, both κ_s and $\lambda_s = (\lambda_1 + \lambda_2)/2$ are measured simultaneously while the antisymmetric combination $\kappa_a = (\kappa_1 - \kappa_2)/2$ and $\lambda_a = (\lambda_1 - \lambda_2)/2$ are set to their binary black hole values of 0. Finally in **Analysis III**, we obtain errors on κ_1 and κ_2 while keeping λ_1 and λ_2 to their BH values of 1. The binary is assumed to be at a distance of 400Mpc and is optimally oriented. The binary's mass-ratio is 1.2 and posses spins of 0.9 and 0.8 respectively for heavier and lighter components, respectively.

spin parameters $(0.9, 0.8)$. The binary is assumed to be optimally oriented at a luminosity distance of 400Mpc. The projected bounds on the binary black hole nature range from 1 to about 8 for the choice of mass-ratio and spin values depending on the type of test performed. We see in Fig. 5.1 that κ_s, whether measured alone (Analysis I) or together with λ_s (Analysis II) is measured with the smallest errors. We also note that the addition of λ_s to the parameter space does not affect the errors on κ_s as they are relatively less correlated because of the different PN orders at which they appear unlike κ_1 and κ_2 which are strongly correlated as they occur together in the phasing.

5.3.1.1 Bounds on binary's spin-induced quadrupole moment parameter

If we assume the two objects in the binary system suffer equal deformation due to their individual spins (*i.e.*, $\kappa_1 = \kappa_2$), the symmetric combination of the coefficient of spin-induced quadrupole moments, κ_s, will be the suitable parameter to constrain

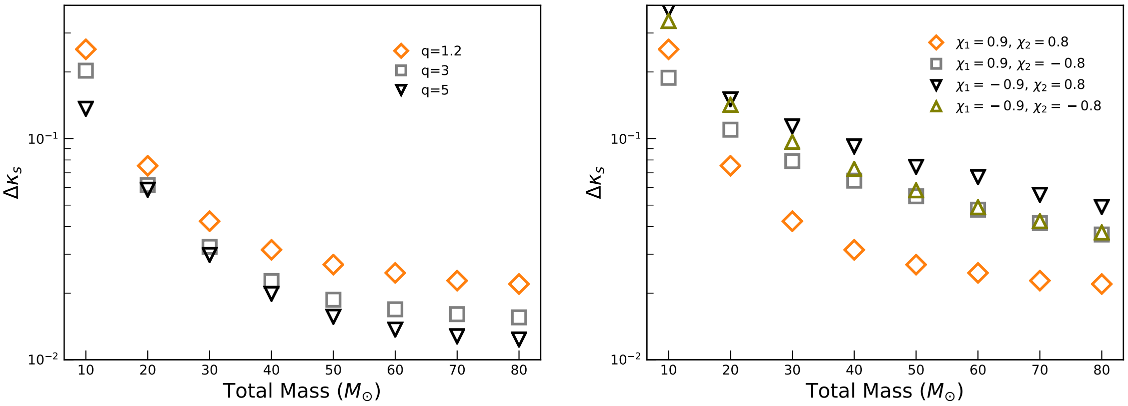

FIGURE 5.2: Figure displays variation of $1-\sigma$ errors on $\kappa_s = (\kappa_1 + \kappa_2)/2$ (where $\kappa_{1,2}$ are parameters characterizing the spin-induced quadrupole moment of each binary component) as a function of the binary's total mass for three representative mass-ratio cases with fixed component spins (χ_1, χ_2) of $(0.9, 0.8)$ (top panel) and four representative spin configurations with fixed mass-ratio (q) of 1.2 (bottom panel).

the binary black hole nature [302]. Any deviation from the binary black hole value of $\kappa_s = 1$ can be interpreted as a possible constraint on the binary black hole nature of the compact binary system. The parameter space considered here is the following,

$$\theta_i = \{\, t_c,\ \phi_c, M_c,\ \eta,\ \chi_1,\ \chi_2,\ \kappa_s\}, \tag{5.6}$$

where t_c and ϕ_c are the time and phase at coalescence, M_c ($M_c = M\,\eta^{3/5}$) is the chirp mass, $\eta = \frac{m_1\, m_2}{(m_1+m_2)^2}$ is the symmetric mass-ratio, $M = m_1 + m_2$ is the total mass and m_1, m_2 and χ_1, χ_2 are the masses and dimensionless spin parameters of the binary constituents. Note that, here κ_s is the only spin-induced parameter that is considered *free* in the analysis; other combinations, (κ_a, λ_s, λ_a), are set to their binary black hole values of $\kappa_a = 0$, $\lambda_s = 1$ and $\lambda_a = 0$.

Figure 5.2 shows the variation of the errors in the measurement of the parameter κ_s, as a function of the total mass of the binary. These errors also provide us $1-\sigma$ upper bounds on the value of κ_s. Three different set of markers in the *top* panel plot correspond to three different mass-ratios (q=1.2, 3, 5) while the component spins are fixed to the values of $\chi_1 = 0.9$, $\chi_2 = 0.8$. On the other hand, the *bottom* panel assumes a binary with fixed mass-ratio ($q = 1.2$) and displays the errors for four different spin configurations. Each set of markers in both panels suggest that errors decrease as the binary's mass increases. This is largely due to larger signal-to-noise ratios associated with heavier binaries with fixed mass-ratio and component spins. In addition, the trends displayed in the *top* panel suggest improved κ_s estimates for larger mass-ratio cases (though the improvement is very minor) while those in the *bottom* panel show that the best κ_s estimates correspond to the case when the two objects have component spins aligned to the orbital angular momentum. The improved κ_s estimates with respect to the mass ratio may be attributed to the larger number of gravitational wave cycles for asymmetric systems in the detector band. Similarly, as the upper cut-off frequency for aligned spin configuration is larger, leading to larger number of gravitational wave cycles, the error estimates for aligned spin configurations are the best.

Figure 5.3 explores κ_s error estimates in component spin parameter space for a binary with total mass of $30 M_\odot$ and mass-ratios of 1.2 (top panel) and 3 (bottom panel). Solid (dashed) contours represent errors on κ_s in the context of CE (advanced LIGO) detector. We can compare the performance of advanced LIGO and CE at those points where their contours intersect. It is obvious from the figure that the typical improvements in the estimation of κ_s due to CE is by a factor of $\sim 40 - 50$. This improvement is correlated with the increased signal-to-noise ratio of the sources in the CE band compared to advanced LIGO. It is worth noting that, even though the overall improvement in sensitivity of CE over advanced LIGO is roughly a factor of 10, due to the larger band width of CE, the signal-to-noise ratios are higher than advanced LIGO roughly by $\sim 40 - 50$ which explains the overall improvement in the parameter estimation of CE with respect to advanced LIGO.

Another striking feature in Fig. 5.3 is the shape of the contours in the component spin plane. For nearly equal mass systems ($q = 1.2$), both advanced LIGO and CE contours are nearly circular, whereas for $q = 3$ they are ellipses. This feature may be explained by a close inspection of the structure of the leading order spin-spin dependence in the phasing which is proportional to the κ_s parameter. The term schematically reads as $\Psi_{\rm spin-spin} \sim \kappa_s \, \zeta(\eta,\, \chi_1,\, \chi_2)$, where

$$\zeta(\eta, \chi_1, \chi_2) = \alpha(\eta)\, \chi_1^2 + \beta(\eta)\, \chi_2^2. \tag{5.7}$$

Here

$$\alpha(\eta) = \left(1 + \sqrt{1 - 4\,\eta} - 2\,\eta\right) \tag{5.8a}$$

and

$$\beta(\eta) = \left(1 - \sqrt{1 - 4\,\eta} - 2\,\eta\right). \tag{5.8b}$$

The derivative of the waveform with respect to κ_s now will scale as $\sim \zeta$ and the corresponding Fisher information matrix element will scale as $\Gamma_{\kappa_s\kappa_s} \sim \zeta^2$. Intuitively, as the error on κ_s is proportional to the square root of the inverse of the Fisher matrix, we find $\Delta\kappa_s \sim \zeta^{-1}$. Now the contours of constant errors in the component spin plane have the form,

$$\chi_1^2\,(\alpha\,\Delta\kappa_s) + \chi_2^2\,(\beta\,\Delta\kappa_s) = 1. \tag{5.9}$$

It is now obvious that for equal mass systems for which $\alpha = \beta$, the contours of constant errors should be circles whereas for unequal mass systems the contours will be ellipses. From Eq. (5.8), as $\frac{1}{\sqrt{\alpha}} \leq \frac{1}{\sqrt{\beta}}$, these ellipses will have their semi-major axis along χ_2 direction as seen in the bottom panel of Fig. 5.3. Though this scaling completely neglects the correlation of κ_s with other parameters, this does give us a qualitative picture about the shape and orientation of the contours. In the following section we will discuss bounds obtained on the spin-induced quadrupole moment parameters from an astrophysical population of compact binary systems.

Finally, Fig. 5.4 compares κ_s estimates obtained using two different third-generation detector configurations, Cosmic Explorer (CE) and Einstein Telescope (ET-D). In this case, errors on κ_s as a function of total mass for a fixed mass-ratio of 1.2 is shown. We consider two spin orientations here, both the black holes aligned and both the black holes anti-aligned to the orbital angular momentum axis. As we expect, the performance of CE and ET-D detectors are comparable. However, the Cosmic Explorer error estimates are marginally better than ET-D for all cases except at low masses when component spins are aligned with respect to the orbital angular momentum. This should be a reflection of the improved low frequency sensitivity of ET-D at frequencies less than 5 Hz.

5.3.1.2 Bounds on the spin-induced quadrupole moment parameter from an astrophysical population of binary systems

We also explore the performance of the proposed test on an astrophysical population of binary black holes that the third-generation detectors may see by simulating two populations of binary black holes which correspond to different models for the component mass distribution. In the first model, we distribute the *source frame* component masses $m_{1,2}$ (here $m_1 > m_2$) uniformly between $5M_\odot$ and $20M_\odot$. The second model assumes a power-law distribution with an index $\alpha = 2.3$ [14, 15] for the primary and uniform distribution for the secondary, again, with masses between $5M_\odot$ to $20M_\odot$. For both these cases, we distribute sources with constant comoving number density up to a redshift of $z = 1$. The source locations and orientations are uniform on the sky and the polarization spheres, respectively. In order to account for the cosmological redshift on the gravitational signal we rescale the source frame masses (m_s) to redshifted masses (m_d) as, $m_d = m_s(1 + z)$ in the gravitational wave signal while performing parameter estimation using Fisher matrix. This means that the maximum and minimum component masses in the detector frame will be $5M_\odot$ and $40M_\odot$, respectively. We randomly draw 2000 sources from this population and perform the Fisher analysis to obtain the errors on various parameters including κ_s. Figure 5.5 shows the resulting distribution of errors on κ_s for the two populations described above using Einstein Telescope and Cosmic Explorer. As can be seen in the inset of Fig. 5.5, use of the uniform over power-law distribution leads to nearly 20% increase in the population of binaries observed with $\Delta\kappa_s \leq 5$ for Cosmic Explorer whereas the errors we get using Einstein Telescope are largely independent of the mass distribution. Furthermore, we find that errors on κ_s are less than 10 for 52% (68%) of the sources for the power-law (uniform) distribution model if we assume CE sensitivity. The numbers change to 41% and 45% respectively for power-law and uniform distributions when we consider Einstein Telescope. These trends can be understood as follows: the mass ratio distribution with primary's mass distributed using the power-law leads to *fewer* sources with larger mass ratios compared to the case where we assume uniform distribution for component masses. In addition, the proposed test is more effective when the mass ratios are higher (see Fig. 5.2). These two factors improve the overall performance of the test for the uniform mass distribution as can be seen in Fig. 5.5.

5.3.1.3 Simultaneous bounds on binary's spin-induced quadrupole and octupole moment parameters

Below we discuss the measurability of both the quadrupolar and octupolar spin-induced deformations due to individual BH spins, simultaneously. This time we intend to measure a symmetric combination of coefficients characterizing the spin-induced octupole moment of the compact binary system: $\lambda_s = (\lambda_1 + \lambda_2)/2$ along with the parameter κ_s. Again the anti-symmetric combinations κ_a and λ_a are set to their binary black hole value of zero. Formally, simultaneous bounds on κ_s and λ_s are more stringent than the κ_s alone as we are sensitive to two of the leading spin-induced multipoles instead of one. The

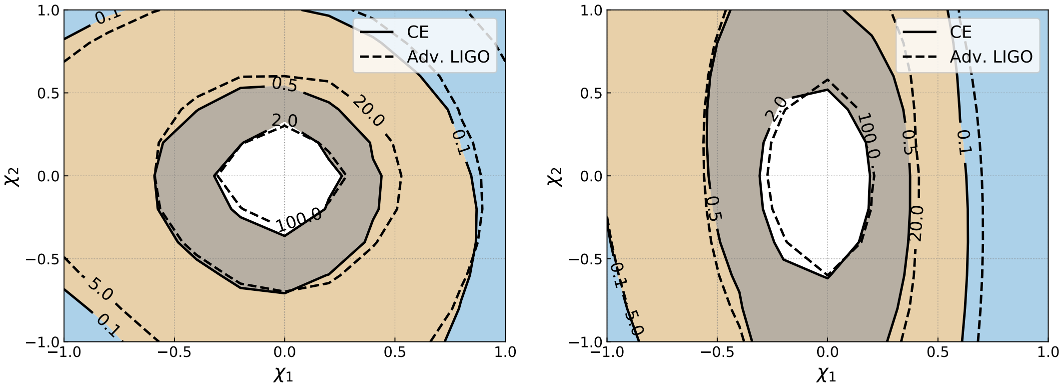

FIGURE 5.3: The errors on κ_s, the symmetric combination of κ_1 and κ_2, in the dimensionless spin parameter plane for the binary system with total mass of $30M_\odot$ and mass-ratios of $q = 1.2$ (top panel) and $q = 3$ (bottom panel). We assume the binary to be optimally oriented at a luminosity distance of 400Mpc. In both panels, the solid curve corresponds to the errors using Cosmic Explorer noise PSD and the errors using advanced LIGO noise PSD is denoted by dashed contours. As can be seen from the plots, parameter space explored in the χ_1-χ_2 plane is much larger for Cosmic Explorer compared to advanced LIGO.

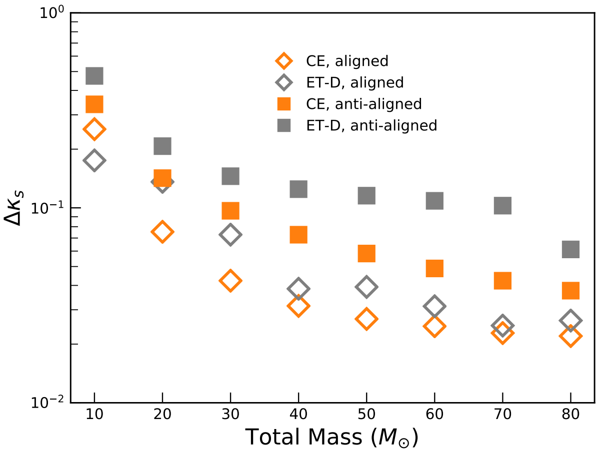

FIGURE 5.4: Errors on the κ_s as a function of the total mass of the binary system for two representative 3rd generation detectors, Cosmic Explorer (CE noise PSD) and Einstein Telescope (ET-D noise PSD). The binary is assumed to be at a distance of 400Mpc and is optimally oriented. The binary's mass-ratio is 1.2 and spin magnitudes of 0.9 and 0.8 for heavier and lighter components, respectively. Filled- (empty-) markers represent spin orientations of each component aligned (anti-aligned) to the orbital angular momentum while squares (diamonds) represent error estimates for Cosmic Explorer (Einstein Telescope, ET-D).

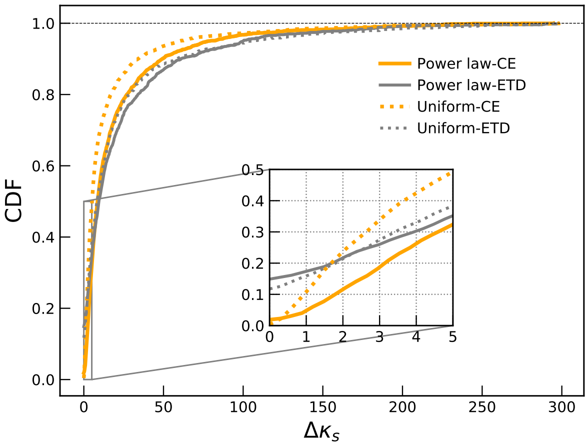

FIGURE 5.5: The cumulative distribution function of errors on κ_s for two prototypical astrophysical populations of binary black holes corresponding to two different models for the binary's mass distribution. In the first model we assume both component masses to be uniformly distributed between $5M_\odot$ to $20M_\odot$ while the second model assumes the primary mass to follow a power-law distribution with an index $\alpha = 2.3$ [14, 15] and uniform distribution for the secondary. In both the models the masses are defined with respect to the source frame and the sources are distributed uniformly in the comoving volume up to a redshift of 1.

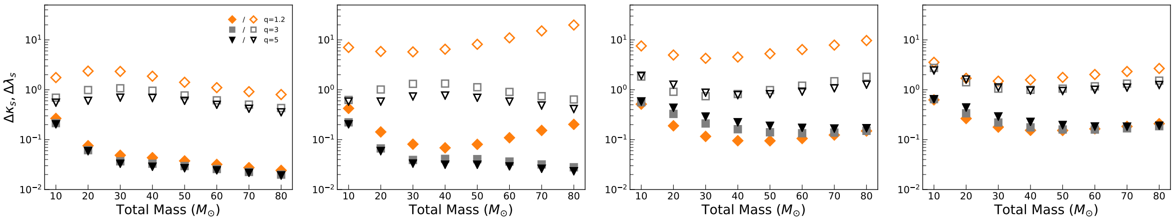

FIGURE 5.6: Figure displays variation of $1-\sigma$ errors on κ_s (filled markers) and λ_s (unfilled markers) as a function of the binary's total mass for three representative mass-ratio cases and four representative spin-orientations with fixed component spin magnitudes (χ_1, χ_2) of $(0.9, 0.8)$. The four panels (left to right) represent binaries where spins of the two BHs are aligned, heavier one aligned and the other anti-aligned, heavier one anti-aligned and the other aligned and both the spins are anti-aligned to the orbital angular momentum axis. We assume the binary to be optimally oriented at a luminosity distance of 400Mpc.

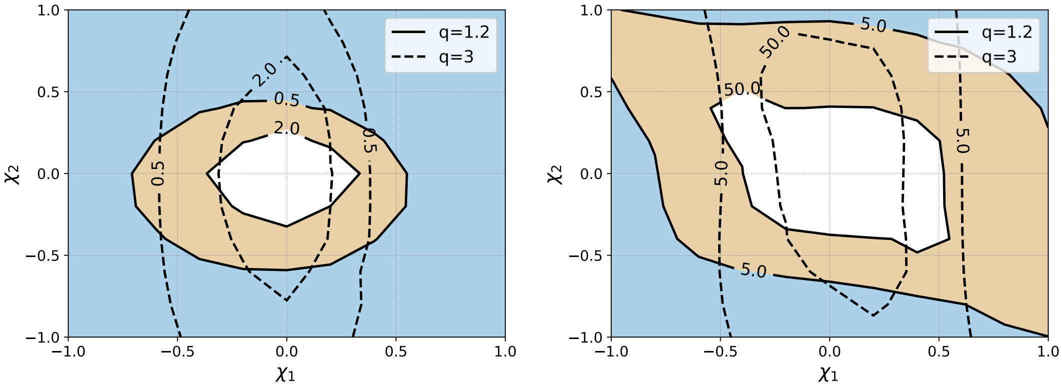

FIGURE 5.7: Errors on spin-induced quadrupole and octupole moment parameters of the binary– κ_s (*top panel*) and λ_s (*bottom panel*) in the χ_1-χ_2 plane for a binary system with total mass $30M_\odot$. Solid contours represent mass-ratio of 1.2 and dashed ones represent mass-ratio 3. Binary system is assumed to be optimally oriented at a luminosity distance of 400Mpc.

parameter space considered for this analysis is,

$$\theta_i = \{\, t_c,\ \phi_c,\ M_c,\ \eta,\ \chi_1,\ \chi_2,\ \kappa_s,\ \lambda_s\}, \tag{5.10}$$

where all the parameters have their usual meaning.

Figure 5.6 shows variations in estimating bounds on κ_s (filled markers) and λ_s (unfilled markers) as a function of the total mass of the binary for three different mass-ratios ($q = 1.2, 3, 5$) and for fixed spin magnitudes of 0.9 and 0.8. Spin orientations chosen are those where both the black hole spins aligned, heavier black hole spin aligned and other anti-aligned, heavier black hole spin anti-aligned other aligned and both the spins anti-aligned to the orbital angular momentum axis, respectively from left to right of Fig. 5.6.

As discussed in Sec. 2.1, spin-induced octupole moment terms start to appear at 3.5 PN order in the PN phasing formula, while the leading spin-induced quadrupole moment contributes at the 2PN order and hence is a dominant effect in the PN dynamics. Hence, among κ_s and λ_s the better constrained parameter is always κ_s. From Fig. 5.6, it is clear that the κ_s errors are almost an order of magnitude better estimated compared to λ_s errors and it is evident from the same figure that, for most of the parameter space, the errors on κ_s is unaffected due to the inclusion of λ_s in the problem.

Figure 5.6 also shows that the bounds on both κ_s and λ_s are tightly constrained for cases where the spin of the heavier black hole aligned to the orbital angular momentum

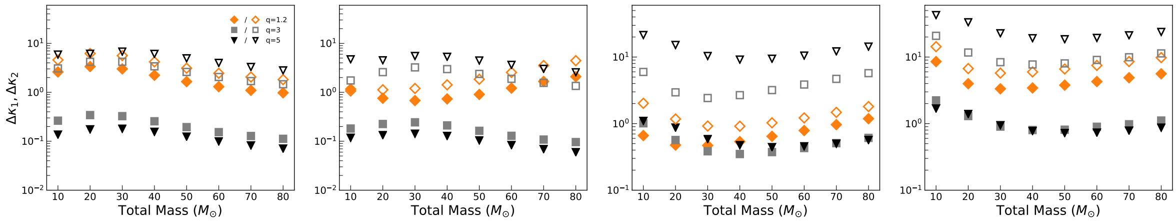

FIGURE 5.8: Figure displays variation of $1-\sigma$ errors on κ_1 (filled markers) and κ_2 (unfilled markers) as a function of the total mass of the binary system for *three* representative mass-ratio cases and *four* representative spin-orientations with fixed component spin magnitudes (χ_1, χ_2) of $(0.9, 0.8)$. The *four* panels (left to right) represent binaries where spins of the two BH are aligned, heavier one aligned and the other anti-aligned, heavier one anti-aligned and the other aligned and both the spins are anti-aligned to the orbital angular momentum axis. Also, note the (up-scaled) y-axes in last two panels.

axis and if the binary is more asymmetric. When both spins are aligned with respect to the orbital angular momentum, the effect of mass-ratio is marginal (similar to the case presented in Sec. 5.3.1.1 where only κ_s is measured). On the other hand, having the lighter component anti-aligned with respect to the orbital angular momentum vector only marginally affects the measurements, with the most affected cases being the symmetric systems. We also note that the trends are not clear when we deal with cases where heavier or both components are anti-aligned. In any case, we do not expect the best results when heavier or both components are anti-aligned.

The effect of spin magnitudes on the error estimates for simultaneous κ_s (top panel) and λ_s (bottom panel) measurements are shown in Fig. 5.7. We choose a total mass of $30M_\odot$ and mass ratios of $q = 1.2$ (solid contours) and $q = 3$ (dotted contours) for this case. Broadly the features seen here resemble those of Fig. 5.3 where only κ_s was estimated. For nearly equal mass systems, we see that the contours are less circular when λ_s is included as a parameter. This may be due to the degeneracies brought in by the estimation of λ_s. Regarding the contours of constant error on λ_s (bottom panel of Fig. 5.7), following a line of argument similar to the one in Sec. 5.3.1.1, it can be shown that the equations of the contours should schematically read as $a\,\chi_1^3 + b\,\chi_2^3 = 1$, where a, b are functions of mass-ratio which decide shape and orientation of the contours.

We performed an analysis, similar to the one reported in Sec. 5.3.1.1, where we simulated two populations of binary black holes following a uniform and power-law distributions for the mass of the binary's primary (heavier) component in the source frame, keeping the secondary component mass to be uniformly distributed such that the total mass is less than or equal to $40M_\odot$. We then compute the distribution of the bounds expected from the resulting population. Our analysis show that when κ_s and λ_s are measured simultaneously, errors on λ_s are less than 10 for about $\sim 6\%(4\%)$ sources when we use power-law (uniform) distribution on component masses for Cosmic Explorer. As observed earlier κ_s estimates are marginally affected compared to the case when κ_s alone is measured. We find that for nearly $42\%(51\%)$ sources $\Delta\kappa_s \leq 10$ with power-law (uniform) distribution when measured along with λ_s. Again the error distribution for κ_s is similar to those in Fig. 5.5.

5.3.1.4 Bounding the black hole nature of the compact binary constituents

In this subsection, we turn to our third and final analysis item – measuring both κ_1, κ_2 that characterize the spin-induced quadrupole moment coefficients of the binary components. Recall that simultaneous measurement of both κ_1, κ_2 provides a much stronger test compared to earlier cases where we assumed the spin-induced multipole coefficients to be the same for both the components of the binary ($\kappa_1 = \kappa_2$, $\lambda_1 = \lambda_2$). The parameter space explored in this case is as follows,

$$\theta_i = \{\, t_c,\, \phi_c, M_c,\, \eta,\, \chi_1,\, \chi_2,\, \kappa_1,\, \kappa_2\}, \tag{5.11}$$

where the parameters have usual meaning.

Figure 5.8 shows variations in errors on κ_1 (filled markers) and κ_2 (empty markers) as a function of total mass of the binary for three different mass ratios ($q = 1.2, 3, 5$) and four different spin configurations (each with fixed spin magnitudes of 0.9 and 0.8 for the heavier and lighter component, respectively). Here again, the spin orientations chosen are those where both the black hole spins aligned, heavier component aligned and other anti-aligned, heavier component anti-aligned other aligned and both the spins anti-aligned to the orbital angular momentum axis, respectively from left to right of Fig. 5.8. One of the first things we observe is that estimates of κ_1 (which characterizes spin-induced deformations of the *heavier* BH) is consistently better than those of κ_2 (which characterizes spin-induced deformations of the *lighter* BH) for all mass-ratios and spin configurations. We also note that κ_1 is measured with smaller errors for systems which are more asymmetric and if the heavier BH is aligned with the orbital angular momentum axis.

These trends can be understood from the leading order spin-induced quadrupole moment term in the gravitational wave phasing formula which is proportional to

$\kappa_1\,\alpha(\eta)\,\chi_1^2+\kappa_2\,\beta(\eta)\,\chi_2^2$ as we explained in Sec. 5.3.1.1. As $\alpha(\eta)\geq\beta(\eta)$ and as we assign larger spin values to the more massive component, for any given spin configuration the pre-factor of κ_1 is always higher than that of κ_2. This explains why κ_1 estimates are better than κ_2. Further, as $\alpha(\eta)$ increases with mass-ratio, the error on κ_1 improves with mass asymmetry. Similarly, the errors on κ_2 worsens with increase in the mass-ratio, since $\beta(\eta)$ is a decreasing function of the mass-ratio.

5.4 Testing the Kerr nature of supermassive and intermediate-mass black hole binaries using spin-induced multipole moment measurements

In this section, we investigate the measurability of spin-induced quadrupole and octupole moment parameters of supermassive and intermediate-mass binary black holes using LISA and DECIGO detector configurations, respectively. Further, we show that the proposed LISA and DECIGO detectors will allow us to measure both spin-induced quadrupole and octupole moment parameters with reasonably good statistical errors and hence are excellent probes for the tests of Kerr nature of the compact binary systems composed of supermassive and intermediate-mass binary black holes, by considering an astrophysical population of binary black holes. We show our main results in Table 5.1. The numbers in Table 5.1 correspond to the percentage of sources that satisfy the detection threshold of LISA and DECIGO and errors on spin-induced multipole moment parameters less than a certain value (see Sec. 5.4.1 for more details). From Table 5.1, it is evident that the gravitational wave observations of spin-induced multipole moment parameters can give stringent constraints on the allowed parameter space of black hole mimickers such as the spinning boson star models in Ref. [193].

To study how well one can constrain the spin-induced quadrupole and octupole moment coefficients using space-based detectors, we perform Fisher information matrix analysis on compact binaries with different masses and spins, see Sec. 5.2.

Detector	$\Delta\kappa_s \leq 1$	$\Delta\kappa_s \leq 0.1$	$\Delta\kappa_s \leq 0.01$	$\Delta\kappa_s \leq 1$ and $\Delta\lambda_s \leq 1$
LISA (Q3-nod)	38.4	1.10	-	1.29
DECIGO (model-1)	91.3	40.01	5.2	49.9

TABLE 5.1: The percentage of total population crossing the detection criteria for for LISA and DECIGO detectors and giving errors on spin-induced quadrupole moment parameters better than a certain value. Among the population models for supermassive and intermediate-mass black holes (described in Sec. 5.4.1) we choose Q3-nod for LISA and model-1 for DECIGO as a representative case here. The DECIGO numbers are given in brackets.

5.4.1 Testing the nature of intermediate-mass and supermassive binary black holes

In this section, we mainly focus on analysis II described in 5.3 that both the constituents of the binary have the same multipole coefficient, *i.e.*, $\kappa_1 = \kappa_2$ and $\lambda_1 = \lambda_2$. This implies that the binary constituents are of the same type, for example, a binary system consisting of two boson stars with a given value of spin-induced multipole moment coefficients. The waveform model we employ is the same as that of 5.2.1. We consider two scenarios to demonstrate the method of testing the binary black hole nature of intermediate-mass and supermassive binary black holes. Firstly, we obtain the errors on spin-induced quadrupole and octupole moment parameters of the compact binary as a function of the total mass of the system keeping the spin magnitudes, mass ratio, location and orientation fixed. Secondly, we investigate the applicability of this test for an astrophysical population of supermassive and intermediate-mass binary black holes assuming certain distributions for the source parameters. In our case the set of parameters in the signal manifold which characterise the compact binary consists of,

$$\vec{\theta} = \Big\{\mathcal{M},\, \delta,\, \chi_1,\, \chi_2,\, \kappa_s,\, \lambda_s,\, t_c,\, \phi_c\Big\}, \tag{5.12}$$

where t_c, ϕ_c are the time and phase at coalescence and $\mathcal{M}$ and δ are the chirp mass and the asymmetric mass ratio of the system [2] and χ_1, χ_2 are the magnitudes of dimensionless

---

[2] These mass parameters related to individual masses of the compact binary system through the following relations: $\mathcal{M} = (m_1 + m_2) \times \left(\frac{m_1 \times m_2}{m_1+m_2}\right)^{3/5}$ and $\delta = \frac{m_1 - m_2}{(m_1+m_2)}$.

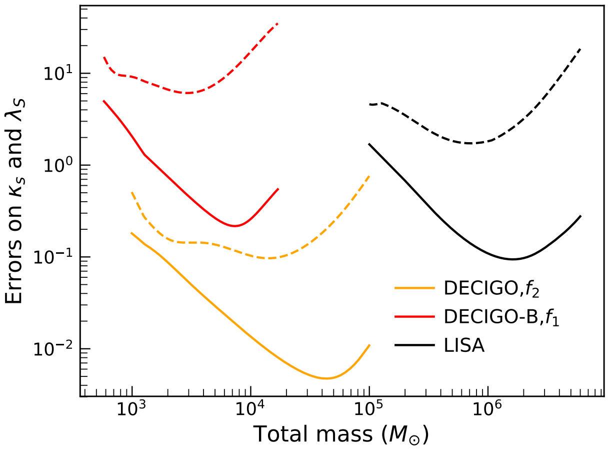

FIGURE 5.9: Errors on spin-induced quadrupole moment parameter ($\Delta\kappa_s$, solid curves) and octupole moment parameter ($\Delta\lambda_s$, dashed curves) as a function of total mass of the binary system which is assumed to be located at a luminosity distance of 1 Gpc and oriented at a particular point in the sky with spin magnitudes (0.6, 0.3) and mass ratio of 1.1. Black, orange and red curves respectively show the results obtained when we consider LISA, DECIGO and DECIGO-B configurations. We assume 4 yr of observation time for all the three detector configurations.

spin parameters [3]. Spin-induced quadrupole and octupole moment parameters of the binary system are κ_s and λ_s, respectively as defined in Sec. 5.3. Notice that while estimating the errors on the symmetric combination of the spin-induced quadrupole (κ_s) and octupole (λ_s) moment parameters, we set the anti-symmetric combination to be zero, *i.e.*, $\kappa_a = \lambda_a = 0$.

5.4.1.1 Errors as a function of total mass of the binary system

In Fig. 5.9, we show the errors on spin-induced quadrupole (solid curve) and octupole moment (dashed curve) parameters as a function of the total mass of the system, where we fix the mass ratio (m_1/m_2) to be 1.1 and the dimensionless component spins (χ_1, χ_2) to be (0.6, 0.3). Black curves in Fig. 5.9 correspond to supermassive black holes (which LISA is more sensitive to) and, orange and red curves show the errors corresponding to intermediate-mass black holes (which DECIGO and DECIGO-B are more sensitive to). As we can see from the figure, errors on both the parameters decrease as a function of total mass initially (irrespective of the detector configuration assumed) and then increase. This is because of the combined effect of the signal-to-noise ratio and the

---

[3] $\tilde{\chi}_i$ is related to the spin angular momentum as $\tilde{\chi}_i$=$|\tilde{S}_i|/m_i^2$, where $|\tilde{S}_i|$ is the spin angular momentum vector and m_i is the mass of the compact object.

inspiral truncation frequency of the analysis. As the total mass increases, signal strength for a binary system with fixed location and orientation in the sky increases, but the number of cycles in the detector band decreases as the upper cut-off frequency decreases, which is inversely related to the total mass.

5.4.1.2 Errors from an astrophysical population of binary systems

The results shown in Fig. 5.9 are not enough to completely assess the capabilities of LISA and DECIGO to carry out the test of Kerr nature of the binary black hole system, as they correspond to certain representative binary configurations. We repeat the analysis for a simulated population of binary black holes, that may be detected by LISA and DECIGO, and obtain the fraction of the total population this test would yield good constraints for. The simulated population in our case assumes that the binary black hole merger rate per redshift bin in the observer frame follows the relation,

$$\frac{\mathsf{d\,R(z)}}{\mathsf{d\,z}} = \mathcal{R}(\mathsf{z})\,\frac{\mathsf{d\,V_c(z)}}{\mathsf{d\,z}}, \tag{5.13}$$

where $\mathsf{R(z)}$ is the number of binary coalescence per observation time, $\mathcal{R}(\mathsf{z})$ is the merger rate density in the detector frame and $\mathsf{V_c(z)}$ denotes the comoving volume.

For LISA sources, we assume the massive black hole rate evolution follows the models given in Klein et al. [16]. These semi-analytical massive black hole-galaxy coevolution models assume two different birth mechanisms for massive black holes and also account for the time delay between massive black hole merger and galaxy merger [330–337]. Following the $\mathsf{R(z)}$ and detector frame total mass distributions given in Fig. [3] of Ref. [16], we populate binary black holes keeping the component masses nearly equal for three different formation mechanisms described in [16][4]. Among all the three models, Model popIII, Model Q3-d and Model Q3-nod, we observe that very few sources cross the detection threshold (SNR≥200) for Model popIII and hence we only show the results obtained from Model Q3-d and Model Q3-nod here.

---

[4] For Q3-nod (Q3-d) we populate up to a redshift of $z = 19(10)$ with total masses range between $8 \times 10^3 - 10^8 M_\odot (2.21 \times 10^4 - 10^8 M_\odot)$.

In order to populate intermediate-mass black holes, which are interesting sources for the DECIGO configurations, we start with the following the relation [167],

$$\mathcal{R}(z) = \mathcal{R}_0\ (1+z)^{\lambda}\ \frac{T_{\rm obs}}{1+z}, \tag{5.14}$$

where $\mathcal{R}(z)$ is the rate of binary mergers that occur over the total observation time $T_{\rm obs}$ measured in the detector frame. Here, $\mathcal{R}_0$ is a constant which gives the rate density corresponding to a particular value of redshift and we fix it to be 40 $\mathrm{Gpc}^{-3}\mathrm{yr}^{-1}$. We distribute sources upto a redshift of 20 assuming two different population models for DECIGO configurations, model-1 and model-2. For model-1, we fix $\lambda = 0$ (rate density is assumed to be a constant with respect to the redshift) and the component masses to be uniformly distributed in the range $10^2 - 10^4 M_\odot$. For model-2, we fix $\lambda = 6.5$ [167] and the primary mass (m_1) is drawn from a power law distribution with index 1.6, in the range $10^2 - 10^4 M_\odot$ and secondary mass (m_2) is drawn from a uniform distribution. The dimensionless spin parameters χ_1 and χ_2 are distributed uniformly between -1 to 1 for both LISA and DECIGO sources. Notice that, among the total populated sources positioned isotropically in orientation and polarisation sky, we choose only those sources which satisfy a detection criteria set by signal-to-noise ratio of 200 for LISA and 100 for DECIGO/DECIGO-B. The cumulative distribution functions of errors obtained on spin-induced quadrupole and octupole moment coefficients for an astrophysical population of binary black hole system are shown in Figs. 5.10 and 5.11.

From Figs. 5.10 and 5.11 we find that the errors on the spin-induced quadrupole moment coefficient are consistently smaller than that of the octupole coefficient for the entire population and all three detector configurations. This is expected as octupole is sub-leading with respect to the quadrupole. Among the simulated binaries which cross the LISA detection threshold, we find that 1.55% (1.29%) of the population has both $\Delta\kappa_s$ and $\Delta\lambda_s$ $\leq$1 if we assume Model Q3-d (Model Q3-nod) [5]. This percentage will increase to 40% when we consider the case where only the spin-induced quadrupole moment parameter is measured with a measurement precision $\leq$1. From the total population of intermediate-mass BHs detectable by DECIGO configuration with a lower cut-off frequency of 10^{-2}Hz(f_2), 49.97% (1.39%) of the sources give errors on both the spin-induced multipole moments $\leq$1 when we assume model-1 (model-2). Assuming model-1 with a lower cut-off frequency of 10^{-2}Hz, we find that 40% (5%) of the DECIGO sources give errors on spin-induced quadrupole moment parameter with

---

[5] $\Delta\kappa_s$ and $\Delta\lambda_s$ =1 corresponds 100% errors on these parameters.

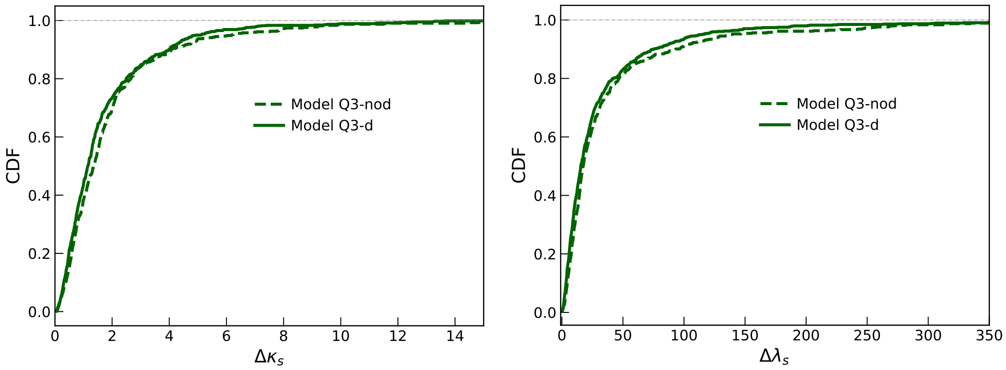

FIGURE 5.10: Cumulative distributions of errors on the spin-induced quadrupole and octupole moment coefficients for an astrophysical population of compact binary systems following Ref. [16]. We choose to show results from two models (Model Q3-d and Model Q3-nod) among the three models given in [16], as from the third model (Model popIII) we do not have enough sources crossing our detection criteria.

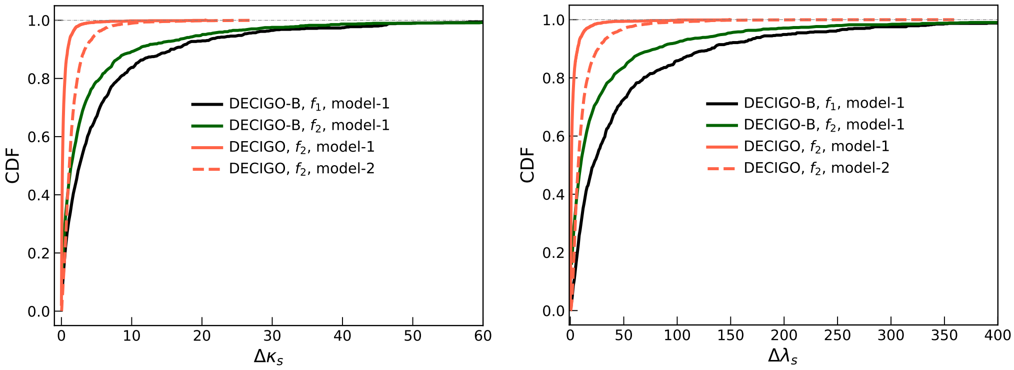

FIGURE 5.11: Cumulative distributions of errors on the spin-induced quadrupole and octupole moment coefficients for an astrophysical population of compact binary systems (see Sec. 5.4 for more details). Two detector configurations of DECIGO, DECIGO-B and DECIGO are considered. We choose two different lower cut-off frequencies for DECIGO-B, 10^{-1}Hz (f_1) and 10^{-2}Hz (f_2) respectively.

$10\%(1\%)$ precison. We see that assuming model-1, 1.04% of the simulated population has errors on both the spin-induced multipole moments $\leq$1 for DECIGO-B with a lower cut-off frequency of 10^{-1}Hz (f_1). This percentage increases to 4.8% with the lower cut-off frequency changing to 10^{-2}Hz (f_2). We conclude by noting that the spin-induced multipole moment coefficients of supermassive and intermediate-mass binary black holes, can be constrained well for a subpopulation of binary systems using LISA, DECIGO and DECIGO-B detectors, respectively.

5.5 Conclusions

In *three* different sets of numerical experiments discussed above, we find that improved sensitivities of third-generation detectors (Cosmic Explorer or Einstein Telescope) over the current advanced LIGO detectors not only allow us to significantly constrain the leading spin-induced effects in gravitational waveforms but also enable us to explore a much wider mass and spin parameter space (Sec. 5.3.1.1). Assuming an astrophysical population of binary black holes, we show that the errors on spin-induced quadrupole moment parameter is ≤ 5 for 30% of the total population if we assume the *primary* component masses follow the power-law distribution when CE configuration is used. This fraction is roughly 20% larger if the component masses are uniformly distributed while the errors with Einstein Telescope are largely independent of the mass distribution as can be seen from Fig. 5.5. As expected, estimated bounds using the two third-generation detectors (Cosmic Explorer or Einstein Telescope) are comparable with a slight favor towards Cosmic Explorer configuration for high mass systems whereas the low mass, aligned spins systems benefit the most from the improved low frequency sensitivity of ET-D. We also showed that at least for a narrower parameter space it would be possible to put stringent bounds on the first two spin-induced multipole moments (quadrupolar and octupolar) simultaneously to assess the nature of the involved compact binary (see Sec. 5.3.1.3 above). This also means one would be able to constrain *four* multipole moments of the compact binary system facilitating a thorough probe of their binary black hole nature. Finally, the possibility of bounding the leading spin-induced moment for each binary component was explored in Sec. 5.3.1.4. Results of Fig. 5.8 suggest a set of possible binary configurations for which at least the nature of the heavier component can be confirmed. Due to the dependencies of the bounds on component spins, mass ratios, and masses, it is somewhat difficult to predict the magnitude of the constraints these measurements will place on the parameter space of BH mimickers. For example, considering boson star models of Ryan [193], the theoretically allowed lower limit on the quadrupole parameter is ~ 10 (see Fig. 4 of [193]) and lower limit on the octupole parameter is ~ 20 (Fig. 5 of [193]). These values do depend on parameters such as the mass of the boson which constitute the boson stars. Figure 5.3 above shows that, unless component spin values are less than 0.1, the expected bounds on κ_s will rule out boson star models which predict $\kappa_s \sim 10$. Similarly, as can be seen from Fig. 5.7, detecting moderate to highly spinning systems ($\chi \sim 0.4 - 0.9$) can help you rule out $\lambda_s \sim 20$. However, it has to be borne in mind that the constraints from individual events can rule out a BH mimicker association only for that system and not a generic constrain on the parameter space of BH mimickers. The constraints on gravastars, however, are likely to be weaker as the spin-induced quadrupole moment parameter of this class of objects spans a small range of values around the BH value (~ -0.17 to ~ 1.8) as can be seen from Fig. 7 of [273].

We find that the future space-based gravitational wave detectors are excellent probe for the black hole nature of the compact binary system. We demonstrate this using an astrophysical population of super massive and intermediate massive binary black holes.

Appendix A

List of amplitude/phase coefficients with spin-induced multipole moment dependence

Here we provide expressions for coefficients that contain explicit dependence on κ_s and κ_a. Below we list the amplitude/phase coefficients that do contain explicit dependence on κ_s and κ_a and can be combined to those listed in Ref. [30, 284] to write the final waveform expression given in the following Eq. (15),

$$\tilde{h}(f) = \frac{M^2}{D_L}\sqrt{\frac{5\,\pi\,\nu}{48}}\sum_{n=0}^{4}\sum_{k=1}^{6} V_k^{n-7/2}\, C_k^{(n)}\, e^{\mathrm{i}(k\,\Psi_{\mathrm{SPA}}(f/k)-\pi/4)}\,. \tag{15}$$

$$\begin{aligned}
\mathcal{C}_2^{(4)} \;=\;& \frac{F_+}{\sqrt{2}}\left(\frac{113419241}{40642560}+\frac{152987}{16128}\,\nu-\frac{11099}{1152}\,\nu^2\right)\\
&+c_\iota^6\left(\frac{-1}{24}+\frac{5}{24}\,\nu-\frac{5}{24}\,\nu^2\right)\\
&+c_\iota^4\left(\frac{1693}{2016}-\frac{5723}{2016}\,\nu+\frac{13}{12}\nu^2\right)\\
&+(\boldsymbol{\chi}_1\cdot\hat{L}_{\rm N})^2\left(\frac{1}{64}-\frac{\nu}{32}+\delta\,\left(\frac{1}{64}+\frac{3}{4}\,\kappa_a+\frac{3}{4}\,\kappa_s\right)\right)\\
&+(\boldsymbol{\chi}_1\cdot\hat{L}_{\rm N})^2\left(\kappa_a\left(\frac{3}{4}-\frac{3}{2}\,\nu\right)+\kappa_s\left(\frac{3}{4}-\frac{3}{2}\,\nu\right)\right)+\frac{47\,\nu}{16}(\boldsymbol{\chi}_1\cdot\hat{L}_{\rm N})(\boldsymbol{\chi}_2\cdot\hat{L}_{\rm N})\\
&+(\boldsymbol{\chi}_2\cdot\hat{L}_{\rm N})^2\left(\frac{1}{64}-\frac{\nu}{32}+\delta\,\left(-\frac{1}{64}+\frac{3}{4}\,\kappa_a-\frac{3}{4}\,\kappa_s\right)\right)\\
&+(\boldsymbol{\chi}_1\cdot\hat{L}_{\rm N})^2\left(\kappa_a\left(-\frac{3}{4}+\frac{3}{2}\,\nu\right)+\kappa_s\left(\frac{3}{4}+\frac{3}{2}\,\nu\right)\right)\\
&+c_\iota^2\left(\frac{165194153}{40642560}-\frac{149}{1792}\,\nu+\frac{6709}{1152}\,\nu^2\right)\\
&+(\boldsymbol{\chi}_1\cdot\hat{L}_{\rm N})^2\,c_\iota^2\,\left(\frac{1}{64}-\frac{\nu}{32}+\delta\,\left(\frac{1}{64}+\frac{3}{4}\,\kappa_a+\frac{3}{4}\,\kappa_s\right)\right)\\
&+(\boldsymbol{\chi}_1\cdot\hat{L}_{\rm N})^2\,c_\iota^2\left(\kappa_a\left(\frac{3}{4}-\frac{3}{2}\,\nu\right)+\kappa_s\left(\frac{3}{4}-\frac{3}{2}\,\nu\right)\right)\\
&+\frac{47\,\nu}{16}\,c_\iota^2(\boldsymbol{\chi}_1\cdot\hat{L}_{\rm N})(\boldsymbol{\chi}_2\cdot\hat{L}_{\rm N})\\
&+(\boldsymbol{\chi}_2\cdot\hat{L}_{\rm N})^2\,c_\iota^2\left(\frac{1}{64}-\frac{\nu}{32}+\delta\,\left(-\frac{1}{64}+\frac{3}{4}\,\kappa_a-\frac{3}{4}\,\kappa_s\right)\right)\\
&+(\boldsymbol{\chi}_1\cdot\hat{L}_{\rm N})^2\,c_\iota^2\left(\kappa_a\left(-\frac{3}{4}+\frac{3}{2}\,\nu\right)+\kappa_s\left(\frac{3}{4}+\frac{3}{2}\,\nu\right)\right)\\
&+\frac{i\,F_\times}{\sqrt{2}}\left(c_\iota^5\left(-\frac{1}{4}+\frac{5}{4}\nu-\frac{5}{4}\,\nu^2\right)+c_\iota^3\left(\frac{5777}{2520}-\frac{5555}{504}\,\nu+\frac{34}{3}\,\nu^2\right)\right)\\
&+c_\iota\left(\frac{114020009}{20321280}+\frac{133411}{8064}\,\nu-\frac{7499}{576}\,\nu^2\right)\\
&+c_\iota(\boldsymbol{\chi}_1\cdot\hat{L}_{\rm N})^2\left(\frac{1}{32}-\frac{\nu}{16}+\delta\,\frac{1}{32}+\frac{3}{2}\kappa_a+\frac{3}{2}\,\kappa_s\right)+\\
&+c_\iota(\boldsymbol{\chi}_1\cdot\hat{L}_{\rm N})^2\left(\kappa_a\left(\frac{3}{2}-3\,\nu\right)+\kappa_s\left(\frac{3}{2}-3\,\nu\right)\right)\\
&+\frac{47}{8}\,\nu\,(\boldsymbol{\chi}_1\cdot\hat{L}_{\rm N})(\boldsymbol{\chi}_2\cdot\hat{L}_{\rm N})\\
&+c_\iota(\boldsymbol{\chi}_2\cdot\hat{L}_{\rm N})^2\left(\frac{1}{32}-\frac{\nu}{16}+\delta\,\frac{1}{32}+\frac{3}{2}\kappa_a+\frac{3}{2}\,\kappa_s\right)+\\
&+c_\iota(\boldsymbol{\chi}_2\cdot\hat{L}_{\rm N})^2\left(\kappa_a\left(\frac{3}{2}-3\,\nu\right)+\kappa_s\left(\frac{3}{2}-3\,\nu\right)\right)
\end{aligned}\tag{16}$$

The explicit expression for 4PN accurate phase $\Psi_{\mathsf{SPA}}(f)$ is given in Eq. 17, where, α_n are $(n/2)^{th}$ PN coefficients and $v = V_k(f)$ is the post-Newtonian parameter defined as $v = (2\,\pi\,M\,f/k)^{1/3}$ for the kth harmonic [6].

$$\Psi_{\mathsf{SPA}}(f) \;=\; \frac{3}{256\,\nu}\sum_{n=0}^{8}\alpha_n\,v^n, \tag{17}$$

$$\begin{aligned}
\alpha_0 &= 1\\
\alpha_1 &= 0\\
\alpha_2 &= \left(\frac{55\,\nu}{9}+\frac{3715}{756}\right)\\
\alpha_3 &= -16\pi+\left(\boldsymbol{\chi}_1\cdot\hat{L}_{\mathsf{N}}\right)\left(\frac{113\,\delta}{6}-\frac{38\,\nu}{3}+\frac{113}{6}\right)+\left(\boldsymbol{\chi}_2\cdot\hat{L}_{\mathsf{N}}\right)\left(-\frac{113\,\delta}{6}-\frac{38\,\nu}{3}+\frac{113}{6}\right)
\end{aligned}$$

$$\begin{aligned}
\alpha_4 &= \frac{15293365}{508032}+\frac{27145\,\nu}{504}+\frac{3085\,\nu^2}{72}+\frac{395\,\nu}{4}(\boldsymbol{\chi}_1\cdot\hat{L}_{\mathsf{N}})\,(\boldsymbol{\chi}_2\cdot\hat{L}_{\mathsf{N}})\\
&+\left(-\frac{5}{16}-\frac{5\,\delta}{16}+\kappa_{\mathsf{a}}\,(-25-25\,\delta+50\,\nu)+\kappa_{\mathsf{s}}\,(-25-25\,\delta+50\,\nu)\right)\,(\boldsymbol{\chi}_1\cdot\hat{L}_{\mathsf{N}})^2\\
&+\left(-\frac{5}{16}+\frac{5\,\delta}{16}+\kappa_{\mathsf{a}}\,(25-25\,\delta-50\,\nu)+\kappa_{\mathsf{s}}\,(-25+25\,\delta+50\,\nu)\right)\,\frac{5\nu}{8}+(\boldsymbol{\chi}_1\cdot\hat{L}_{\mathsf{N}})^2
\end{aligned}$$

---

[6] Note, here f is the gravitational wave frequency.

$$
\begin{aligned}
\alpha_5 \;=\;& \frac{38645\,\pi}{756} - \frac{65\,\pi\,\nu}{9} + \frac{38645}{252}\,\pi\,\log(v) - \frac{65}{3}\,\pi\,\nu\,\log(v) \\
&+(\boldsymbol{\chi}_1\cdot\hat{L}_{\mathrm{N}})\left(-\frac{732985}{4536} - \frac{732985\,\delta}{4536} + \frac{12130\,\nu}{81}\right) \\
&+(\boldsymbol{\chi}_1\cdot\hat{L}_{\mathrm{N}})\left(-\frac{70}{9}\,\delta\,\nu + \frac{170}{9}\,\nu^2\right) \\
&+(\boldsymbol{\chi}_1\cdot\hat{L}_{\mathrm{N}})\left(-\frac{732985}{1512}\,\log(v) - \frac{732985}{1512}\,\delta\,\log(v) + \frac{12130}{27}\nu\,\log(v)\right) \\
&(\boldsymbol{\chi}_1\cdot\hat{L}_{\mathrm{N}})\left(-\frac{70}{3}\delta\,\nu\,\log(v) + \frac{170}{3}\,\nu^2\,\log(v)\right) \\
&+(\boldsymbol{\chi}_2\cdot\hat{L}_{\mathrm{N}})\left(-\frac{732985}{4536} - \frac{732985}{4536}\,\delta + \frac{12130}{81}\,\nu + \frac{70}{9}\,\delta\,\nu + \frac{170}{9}\,\nu^2\right) \\
&+(\boldsymbol{\chi}_2\cdot\hat{L}_{\mathrm{N}})\left(-\frac{732985}{1512}\,\log(v) + \frac{732985}{1512}\,\delta\,\log(v) + \frac{12130}{27}\nu\,\log(v)\right) \\
&+(\boldsymbol{\chi}_2\cdot\hat{L}_{\mathrm{N}})\left(\frac{70}{3}\delta\,\nu\,\log(v) + \frac{170}{3}\,\nu^2\,\log(v)\right)
\end{aligned}
\tag{18}
$$

$$
\begin{aligned}
\alpha_6 \;=\;& \frac{11583231236531}{4694215680} - \frac{640}{3}\pi^2 - \frac{6848}{21}\gamma\mathrm{E} - \frac{15737765635}{3048192}\,\nu \\
&+\frac{2255}{12}\,\pi^2\,\nu + \frac{76055}{1728}\,\nu^2 - \frac{127825}{1296}\,\nu^3 \\
&+(\boldsymbol{\chi}_1\cdot\hat{L}_{\mathrm{N}})^2\Bigg(\frac{1344475}{4032}) - \frac{1344475}{4032}\,\delta + \frac{1365335}{2016}\,\nu + \frac{745}{72}\,\delta\,\nu) + \frac{1255}{36}\,\nu^2)\Bigg) \\
&+(\boldsymbol{\chi}_1\cdot\hat{L}_{\mathrm{N}})^2\,\kappa_{\mathrm{a}}\left(\frac{26015}{56} + \frac{26015}{56}\,\delta - \frac{44255}{42}\,\nu - \frac{1495}{12}\,\delta\,\nu - 120\,\nu^2\right) \\
&+(\boldsymbol{\chi}_2\cdot\hat{L}_{\mathrm{N}})^2\,\kappa_{\mathrm{s}}\left(\frac{26015}{56} + \frac{26015}{56}\,\delta - \frac{44255}{42}\,\nu - \frac{1495}{12}\,\delta\,\nu - 120\,\nu^2\right) \\
&+(\boldsymbol{\chi}_1\cdot\hat{L}_{\mathrm{N}})^2\left(-\frac{1344475}{4032} + \frac{1344475}{4032}\,\delta + \frac{1365335}{2016}\,\nu - \frac{745}{72}\,\delta\,\nu + \frac{1255}{36}\,\nu^2\right) \\
&+(\boldsymbol{\chi}_2\cdot\hat{L}_{\mathrm{N}})^2\,\kappa_{\mathrm{a}}\left(-\frac{26015}{56} + \frac{26015}{56}\,\delta + \frac{44255}{42}\,\nu - \frac{1495}{12}\,\delta\,\nu + 120\,\nu^2\right) \\
&+(\boldsymbol{\chi}_2\cdot\hat{L}_{\mathrm{N}})^2\,\kappa_{\mathrm{s}}\left(-\frac{26015}{56} - \frac{26015}{56}\,\delta - \frac{44255}{42}\,\nu - \frac{1495}{12}\,\delta\,\nu - 120\,\nu^2\right) \\
&+(\boldsymbol{\chi}_1\cdot\hat{L}_{\mathrm{N}})\left(\frac{1135}{3}\,\pi + \frac{1135}{3}\pi\,\delta - 260\,\pi\nu\right) \\
&+(\boldsymbol{\chi}_2\cdot\hat{L}_{\mathrm{N}})\left(\frac{1135}{3}\,\pi - \frac{1135}{3}\pi\,\delta - 260\,\pi\nu\right) \\
&+(\boldsymbol{\chi}_1\cdot\hat{L}_{\mathrm{N}})(\boldsymbol{\chi}_2\cdot\hat{L}_{\mathrm{N}})\left(\frac{32675}{112}\,\nu + \frac{5575}{18}\nu^2\right) - \frac{6848}{21}\,\log(4) - \frac{6848}{21}\,\log(v)
\end{aligned}
\tag{19}
$$

$$
\begin{aligned}
\alpha_7 \;=\;& \frac{77096675}{254016}\,\pi + \frac{378515}{1512}\,\pi\,\nu - \frac{74045}{756}\,\pi\,\nu^2 \\
&+(\boldsymbol{\chi}_1\cdot\hat{L}_\mathrm{N})\left(-\frac{25150083775}{6096384} - \frac{25150083775}{6096384}\,\delta + \frac{10566655595}{1524096}\,\nu\right) \\
&+(\boldsymbol{\chi}_1\cdot\hat{L}_\mathrm{N})\left(\frac{26804935}{12096}\,\delta\,\nu - \frac{1042165}{6048}\,\nu^2 - \frac{1985}{96}\delta\,\nu^2 + \frac{5345}{72}\,\nu^3\right) \\
&+(\boldsymbol{\chi}_2\cdot\hat{L}_\mathrm{N})\left(-\frac{25150083775}{6096384} + \frac{25150083775}{6096384}\,\delta + \frac{10566655595}{1524096}\,\nu\right) \\
&+(\boldsymbol{\chi}_2\cdot\hat{L}_\mathrm{N})\left(-\frac{26804935}{12096}\,\delta\,\nu - \frac{1042165}{6048}\,\nu^2 + \frac{1985}{96}\delta\,\nu^2 + \frac{5345}{72}\,\nu^3\right) \\
&+(\boldsymbol{\chi}_1\cdot\hat{L}_\mathrm{N})^2\,(\boldsymbol{\chi}_2\cdot\hat{L}_\mathrm{N})\left(\frac{49315}{48}\,\nu + \frac{49315}{48}\,\delta\,\nu - \frac{15}{2}\,\nu^2\right) \\
&+(\boldsymbol{\chi}_2\cdot\hat{L}_\mathrm{N})^2\,(\boldsymbol{\chi}_1\cdot\hat{L}_\mathrm{N})\left(\frac{49315}{48}\,\nu - \frac{49315}{48}\,\delta\,\nu - \frac{15}{2}\,\nu^2\right) \\
&+(\boldsymbol{\chi}_1\cdot\hat{L}_\mathrm{N})^2\,(\boldsymbol{\chi}_2\cdot\hat{L}_\mathrm{N})\,\kappa_\mathrm{a}\left(-\frac{445}{3}\,\nu - \frac{445}{3}\,\delta\,\nu + 10\,\nu^2\right) \\
&+(\boldsymbol{\chi}_1\cdot\hat{L}_\mathrm{N})^2\,(\boldsymbol{\chi}_2\cdot\hat{L}_\mathrm{N})\,\kappa_\mathrm{s}\left(-\frac{445}{3}\,\nu - \frac{445}{3}\,\delta\,\nu + 10\,\nu^2\right) \\
&+(\boldsymbol{\chi}_2\cdot\hat{L}_\mathrm{N})^2\,(\boldsymbol{\chi}_1\cdot\hat{L}_\mathrm{N})\,\kappa_\mathrm{a}\left(\frac{445}{3}\,\nu - \frac{445}{3}\,\delta\,\nu - 10\,\nu^2\right) \\
&+(\boldsymbol{\chi}_1\cdot\hat{L}_\mathrm{N})^2\,(\boldsymbol{\chi}_2\cdot\hat{L}_\mathrm{N})\,\kappa_\mathrm{s}\left(-\frac{445}{3}\,\nu - \frac{445}{3}\,\delta\,\nu - 10\,\nu^2\right) \\
&+(\boldsymbol{\chi}_1\cdot\hat{L}_\mathrm{N})^3\left(\frac{265}{48} + \frac{265}{48}\,\delta - \frac{895}{48}\,\nu - \frac{365}{48}\,\delta\,\nu + \frac{25}{6}\,\nu^2\right) \\
&+(\boldsymbol{\chi}_1\cdot\hat{L}_\mathrm{N})^3\kappa_\mathrm{a}\left(\frac{1555}{3} + \frac{1555}{3}\,\delta - 1560\,\nu - \frac{1570}{3}\,\delta\,\nu + 10\,\nu^2\right) \\
&+(\boldsymbol{\chi}_1\cdot\hat{L}_\mathrm{N})^3\kappa_\mathrm{s}\left(\frac{1555}{3} + \frac{1555}{3}\,\delta - 1560\,\nu - \frac{1570}{3}\,\delta\,\nu + 10\,\nu^2\right) \\
&+(\boldsymbol{\chi}_1\cdot\hat{L}_\mathrm{N})^3\lambda_\mathrm{s}\,(-220 - 220\,\delta + 660\nu + 220\delta\,\nu) \\
&+(\boldsymbol{\chi}_1\cdot\hat{L}_\mathrm{N})^3\lambda_\mathrm{a}\,(-220 - 220\,\delta + 660\nu + 220\delta\,\nu) \\
&+(\boldsymbol{\chi}_2\cdot\hat{L}_\mathrm{N})^3\kappa_\mathrm{a}\left(-\frac{1555}{3} + \frac{1555}{3}\,\delta + 1560\,\nu - \frac{1570}{3}\,\delta\,\nu - 10\,\nu^2\right) \\
&+(\boldsymbol{\chi}_1\cdot\hat{L}_\mathrm{N})^3\kappa_\mathrm{s}\left(\frac{1555}{3} - \frac{1555}{3}\,\delta - 1560\,\nu + \frac{1570}{3}\,\delta\,\nu + 10\,\nu^2\right) \\
&+(\boldsymbol{\chi}_1\cdot\hat{L}_\mathrm{N})^3\lambda_\mathrm{s}\,(-220 + 220\,\delta + 660\nu - 220\delta\,\nu) \\
&+(\boldsymbol{\chi}_1\cdot\hat{L}_\mathrm{N})^3\lambda_\mathrm{a}\,(220 - 220\,\delta - 660\nu + 220\delta\,\nu) \\
&+(\boldsymbol{\chi}_2\cdot\hat{L}_\mathrm{N})^3\left(\frac{265}{48} - \frac{265}{48}\,\delta - \frac{895}{48}\,\nu + \frac{365}{48}\,\delta\,\nu + \frac{25}{6}\,\nu^2\right) \qquad (20)
\end{aligned}
$$

$$
\begin{aligned}
\alpha_8 \;=\;& (\boldsymbol{\chi}_1\cdot\hat{\mathsf{L}}_{\mathsf{N}})\left(\frac{233915}{336}\,\pi-\frac{233915}{336}\,\pi\,\delta-\frac{3970375}{4536}\,\pi\,\nu+\frac{99185}{504}\,\pi\,\delta\,\nu\right)\\
&+(\boldsymbol{\chi}_1\cdot\hat{\mathsf{L}}_{\mathsf{N}})\left(\frac{19655}{378}\,\pi\,\nu^2-\frac{233915}{112}\,\pi\,\log(v)\right)\\
&+(\boldsymbol{\chi}_1\cdot\hat{\mathsf{L}}_{\mathsf{N}})\left(\frac{233915}{112}\,\pi\,\delta\,\log(v)\right)\\
&+(\boldsymbol{\chi}_1\cdot\hat{\mathsf{L}}_{\mathsf{N}})\left(\frac{3970375}{1512}\pi\,\nu\,\log(v)-\frac{99185}{168}\,\pi\,\delta\,\nu\,\log(v)-\frac{19655}{126}\,\pi\,\nu^2\,\log(v)\right)\\
&+(\boldsymbol{\chi}_2\cdot\hat{\mathsf{L}}_{\mathsf{N}})\left(\frac{233915}{336}\,\pi+\frac{233915}{336}\,\pi\,\delta-\frac{3970375}{4536}\,\pi\,\nu-\frac{99185}{504}\,\pi\,\delta\,\nu\right)\\
&+(\boldsymbol{\chi}_2\cdot\hat{\mathsf{L}}_{\mathsf{N}})\left(\frac{19655}{378}\,\pi\,\nu^2-\frac{233915}{112}\,\pi\,\log(v)\right)\\
&+(\boldsymbol{\chi}_1\cdot\hat{\mathsf{L}}_{\mathsf{N}})\left(-\frac{233915}{112}\,\pi\,\delta\,\log(v)+\frac{3970375}{1512}\pi\,\nu\,\log(v)+\frac{99185}{168}\,\pi\,\delta\,\nu\,\log(v)\right)\\
&+(\boldsymbol{\chi}_2\cdot\hat{\mathsf{L}}_{\mathsf{N}})\left(-\frac{19655}{126}\,\pi\,\nu^2\,\log(v)\right)
\end{aligned}
\qquad (21)
$$

Bibliography

[1] *LIGO Scientific Collaboration*, https://www.ligo.caltech.edu/gallery.

[2] B. P. Abbott et al. (Virgo, LIGO Scientific), Phys. Rev. Lett. **116**, 061102 (2016), 1602.03837.

[3] J. Aasi et al. (LIGO Scientific), Class. Quant. Grav. **32**, 074001 (2015), 1411.4547.

[4] B. P. Abbott et al. (LIGO Scientific) (2016), 1607.08697.

[5] S. Hild et al., Classical and Quantum Gravity **28**, 094013 (2011).

[6] K. Yagi and N. Seto, Phys. Rev. **D83**, 044011 (2011), [Erratum: Phys. Rev.D95,no.10,109901(2017)].

[7] S. Isoyama, H. Nakano, and T. Nakamura, PTEP **2018**, 073E01 (2018), 1802.06977.

[8] S. Babak, J. Gair, A. Sesana, E. Barausse, C. F. Sopuerta, C. P. L. Berry, E. Berti, P. Amaro-Seoane, A. Petiteau, and A. Klein, ArXiv e-prints (2017), 1703.09722.

[9] M. Vallisneri, Phys. Rev. **D86**, 082001 (2012), 1207.4759.

[10] B. P. Abbott et al. (Virgo, LIGO Scientific), Phys. Rev. Lett. **116**, 241103 (2016), 1606.04855.

[11] B. P. Abbott et al. (Virgo, LIGO Scientific), Astrophys. J. **851**, L35 (2017), 1711.05578.

[12] J. Veitch et al., Phys. Rev. **D91**, 042003 (2015), 1409.7215.

[13] S. Husa, S. Khan, M. Hannam, M. Pürrer, F. Ohme, X. Jiménez Forteza, and A. Bohé, Phys. Rev. **D93**, 044006 (2016), 1508.07250.

[14] B. P. Abbott et al. (LIGO Scientific, Virgo) (2018), 1811.12907.

[15] B. P. Abbott et al. (VIRGO, LIGO Scientific), Phys. Rev. Lett. **118**, 221101 (2017), [Erratum: Phys. Rev. Lett.121,no.12,129901(2018)], 1706.01812.

[16] A. Klein et al., Phys. Rev. **D93**, 024003 (2016), 1511.05581.

[17] A. Einstein and J. J. e. a. Stachel, *The collected papers of Albert Einstein: English translation supplement* (Princeton Univ. Press, Princeton, NJ, 1987).

[18] M. Maggiore, in *Sense of Beauty in Physics: Miniconference in Honor of Adriano Di Giacomo on his 70th Birthday Pisa, Italy, January 26-27, 2006* (2006), gr-qc/0602057.

[19] J. D. E. Creighton and W. G. Anderson, *Gravitational-wave physics and astronomy: An introduction to theory, experiment and data analysis* (2011).

[20] S. Klimenko, I. Yakushin, A. Mercer, and G. Mitselmakher, Class. Quant. Grav. **25**, 114029 (2008), 0802.3232.

[21] R. Lynch, S. Vitale, R. Essick, E. Katsavounidis, and F. Robinet, Phys. Rev. **D95**, 104046 (2017), 1511.05955.

[22] B. P. Abbott et al. (LIGO Scientific, Virgo) (2019), 1905.03457.

[23] B. P. Abbott et al. (LIGO Scientific, Virgo), Astrophys. J. **875**, 122 (2019), 1812.11656.

[24] N. Christensen, Rept. Prog. Phys. **82**, 016903 (2019), 1811.08797.

[25] B. P. Abbott et al. (LIGO Scientific, Virgo), Phys. Rev. Lett. **120**, 091101 (2018), 1710.05837.

[26] B. P. Abbott et al. (LIGO Scientific, Virgo), Phys. Rev. Lett. **116**, 131102 (2016), 1602.03847.

[27] L. Blanchet, Living Reviews in Relativity **17**, 2 (2014), 1310.1528.

[28] F. Pretorius (2007), 0710.1338.

[29] M. Sasaki and H. Tagoshi, Living Rev. Rel. **6**, 6 (2003), gr-qc/0306120.

[30] C. K. Mishra, A. Kela, K. G. Arun, and G. Faye, Phys. Rev. **D93**, 084054 (2016), 1601.05588.

[31] Y. Pan, A. Buonanno, A. Taracchini, L. E. Kidder, A. H. Mroué, H. P. Pfeiffer, M. A. Scheel, and B. Szilágyi, Phys. Rev. **D89**, 084006 (2014), 1307.6232.

[32] B. Moore and N. Yunes (2019), 1903.05203.

[33] J. Vines, E. E. Flanagan, and T. Hinderer, Phys.Rev. D **83**, 084051 (2011), 1101.1673.

[34] E. Poisson, Phys. Rev. D **57**, 5287 (1998), gr-qc/9709032.

[35] T. Abdelsalhin, Ph.D. thesis, INFN, Rome (2019), 1905.00408.

[36] Annals of Physics **29**, 304 (1964), ISSN 0003-4916.

[37] R. L. Arnowitt, S. Deser, and C. W. Misner, Gen. Rel. Grav. **40**, 1997 (2008), gr-qc/0405109.

[38] L. Smarr, in *Sources of Gravitational Radiation*, edited by L. L. Smarr (1979), pp. 245–274.

[39] F. Pretorius, Phys. Rev. Lett. **95**, 121101 (2005), gr-qc/0507014.

[40] J. G. Baker, J. Centrella, D.-I. Choi, M. Koppitz, and J. van Meter, Phys. Rev. Lett. **96**, 111102 (2006), gr-qc/0511103.

[41] M. Campanelli, C. O. Lousto, P. Marronetti, and Y. Zlochower, Phys. Rev. Lett. **96**, 111101 (2006), gr-qc/0511048.

[42] M. Boyle et al. (2019), 1904.04831.

[43] K. Jani, J. Healy, J. A. Clark, L. London, P. Laguna, and D. Shoemaker, Class. Quant. Grav. **33**, 204001 (2016), 1605.03204.

[44] J. Healy, C. O. Lousto, J. Lange, R. O'Shaughnessy, Y. Zlochower, and M. Campanelli (2019), 1901.02553.

[45] A. Buonanno and T. Damour, Phys. Rev. **D62**, 064015 (2000), gr-qc/0001013.

[46] Y. Pan, A. Buonanno, A. Taracchini, L. E. Kidder, A. H. Mroué, H. P. Pfeiffer, M. A. Scheel, and B. Szilágyi, Phys. Rev. **D89**, 084006 (2014), 1307.6232.

[47] A. Taracchini et al., Phys. Rev. **D89**, 061502 (2014), 1311.2544.

[48] A. Nagar et al., Phys. Rev. **D98**, 104052 (2018), 1806.01772.

[49] P. Ajith and Babak, Class. Quantum Grav. **24**, 689 (2007), 0704.3764.

[50] P. Ajith, S. Babak, Chen, et al., Phys. Rev. D **77**, 104017 (2008), 0710.2335.

[51] P. Ajith, M. Hannam, S. Husa, Y. Chen, B. Bruegmann, et al., Phys.Rev.Lett. **106**, 241101 (2011), arXiv:0909.2867.

[52] P. Ajith, Phys.Rev. **D84**, 084037 (2011), 1107.1267.

[53] M. Hannam, Gen. Rel. Grav. **46**, 1767 (2014), 1312.3641.

[54] T. Dietrich, A. Samajdar, S. Khan, N. K. Johnson-McDaniel, R. Dudi, and W. Tichy (2019), 1905.06011.

[55] T. D. Abbott et al. (LIGO Scientific, Virgo), Phys. Rev. **X6**, 041014 (2016), 1606.01210.

[56] S. A. Usman et al., Class. Quant. Grav. **33**, 215004 (2016), 1508.02357.

[57] S. Sachdev et al. (2019), 1901.08580.

[58] C. Cutler and E. E. Flanagan, Phys. Rev. **D49**, 2658 (1994), gr-qc/9402014.

[59] C. Rao, Bullet. Calcutta Math. Soc **37**, 81 (1945).

[60] H. Cramer, *Mathematical methods in statistics* (Pergamon Press, Princeton University Press, NJ, U.S.A., 1946).

[61] W. Del Pozzo, J. Veitch, and A. Vecchio, Phys.Rev. **D83**, 082002 (2011), 1101.1391.

[62] M. Agathos, W. Del Pozzo, T. G. F. Li, C. V. D. Broeck, J. Veitch, et al., Phys.Rev. **D89**, 082001 (2014), 1311.0420.

[63] J. Veitch and A. Vecchio, Phys.Rev. D **81**, 062003 (2010), 0911.3820.

[64] J. Skilling, Bayesian Anal. **1**, 833 (2006).

[65] F. Feroz and M. P. Hobson, Mon. Not. Roy. Astron. Soc. **384**, 449 (2008), 0704.3704.

[66] F. Feroz, M. P. Hobson, and M. Bridges, Mon. Not. Roy. Astron. Soc. **398**, 1601 (2009), 0809.3437.

[67] F. Feroz, M. P. Hobson, E. Cameron, and A. N. Pettitt (2013), 1306.2144.

[68] J. Weber, Phys. Rev. Lett. **20**, 1307 (1968).

[69] J. Weber, Phys. Rev. Lett. **18**, 498 (1967).

[70] J. Weber, Phys. Rev. Lett. **22**, 1320 (1969).

[71] J. H. Taylor and J. M. Weisberg, apj **253**, 908 (1982).

[72] J. H. Taylor and J. M. Weisberg, apj **345**, 434 (1989).

[73] J. M. Weisberg and Y. Huang, Astrophys. J. **829**, 55 (2016), `1606.02744`.

[74] The Nobel Prize in Physics 1993, `https://www.nobelprize.org/prizes/physics/1993/press-release/` (2018).

[75] G. Weinstein, arXiv e-prints arXiv:1602.04040 (2016), `1602.04040`.

[76] P. Saulson, *Fundamentals of Interferometric Gravitational Wave Detectors* (World Scientific, 1994), ISBN 9789810218201.

[77] J. Aasi et al. (LIGO Scientific, VIRGO), Phys. Rev. Lett. **113**, 231101 (2014), `1406.4556`.

[78] P. Fritschel, Proc. SPIE Int. Soc. Opt. Eng. **4856**, 282 (2003), `gr-qc/0308090`.

[79] B. P. Abbott et al. (Virgo, LIGO Scientific), Phys. Rev. **X6**, 041015 (2016), `1606.04856`.

[80] N. J. Cornish and T. B. Littenberg, Class. Quant. Grav. **32**, 135012 (2015), `1410.3835`.

[81] B. P. Abbott et al. (Virgo, LIGO Scientific), Phys. Rev. Lett. **116**, 221101 (2016), `1602.03841`.

[82] B. P. Abbott et al. (LIGO Scientific, Virgo) (2019), `1903.04467`.

[83] A. Ghosh, N. K. Johnson-Mcdaniel, A. Ghosh, C. K. Mishra, P. Ajith, W. Del Pozzo, C. P. L. Berry, A. B. Nielsen, and L. London (2017), `1704.06784`.

[84] A. Ghosh, N. K. Johnson-McDaniel, A. Ghosh, C. Kant Mishra, P. Ajith, W. Del Pozzo, C. P. L. Berry, A. B. Nielsen, and L. London, Classical and Quantum Gravity **35**, 014002 (2018), `1704.06784`.

[85] J. Healy, C. O. Lousto, and Y. Zlochower, Phys. Rev. **D90**, 104004 (2014), `1406.7295`.

[86] K. G. Arun, B. R. Iyer, M. S. S. Qusailah, and B. S. Sathyaprakash, Class. Quantum Grav. **23**, L37 (2006), gr-qc/0604018.

[87] K. Yagi, L. C. Stein, N. Yunes, and T. Tanaka, Phys. Rev. **D85**, 064022 (2012), [Erratum: Phys. Rev.D93,no.2,029902(2016)], 1110.5950.

[88] K. G. Arun, B. R. Iyer, M. S. S. Qusailah, and B. S. Sathyaprakash, Phys. Rev. D **74**, 024006 (2006), gr-qc/0604067.

[89] N. Yunes and F. Pretorius, Phys. Rev. **D80**, 122003 (2009), 0909.3328.

[90] C. K. Mishra, K. G. Arun, B. R. Iyer, and B. S. Sathyaprakash, Phys. Rev. **D 82**, 064010 (2010), 1005.0304.

[91] M. Agathos, W. Del Pozzo, T. G. F. Li, C. Van Den Broeck, J. Veitch, and S. Vitale, Phys. Rev. **D89**, 082001 (2014), 1311.0420.

[92] B. P. Abbott et al. (Virgo, LIGO Scientific), Phys. Rev. Lett. **116**, 221101 (2016), 1602.03841.

[93] B. P. Abbott et al. (LIGO Scientific, Virgo) (2018), 1811.00364.

[94] N. Yunes, K. Yagi, and F. Pretorius, Phys. Rev. **D94**, 084002 (2016), 1603.08955.

[95] C. M. Will, Phys. Rev. **D50**, 6058 (1994), gr-qc/9406022.

[96] B. P. Abbott et al. (LIGO Scientific, Virgo) (2018), 1811.00364.

[97] D. Mattingly, Living Rev. Rel. **8**, 5 (2005), gr-qc/0502097.

[98] A. Samajdar and K. G. Arun, Phys. Rev. **D96**, 104027 (2017), 1708.00671.

[99] G. Amelino-Camelia, Nature **418**, 34 (2002), gr-qc/0207049.

[100] C. M. Will, Living Rev. Rel. **17**, 4 (2014), 1403.7377.

[101] G. Calcagni, Phys. Rev. Lett. **104**, 251301 (2010), 0912.3142.

[102] S. Mirshekari, N. Yunes, and C. M. Will, Phys. Rev. **D85**, 024041 (2012), 1110.2720.

[103] B. P. Abbott et al. (Virgo, LIGO Scientific), Phys. Rev. Lett. **119**, 141101 (2017), 1709.09660.

[104] B. P. Abbott et al. (LIGO Scientific Collaboration and Virgo Collaboration), Phys. Rev. Lett. **119**, 161101 (2017).

[105] B. P. Abbott et al., Astrophys. J. **848**, L12 (2017), `1710.05833`.

[106] E. Waxman and J. Bahcall, Phys. Rev. Lett. **78**, 2292 (1997).

[107] A. Margiotta (ANTARES), Nucl. Instrum. Meth. **A725**, 98 (2013).

[108] M. G. Aartsen et al. (IceCube), Astrophys. J. **796**, 109 (2014), `1406.6757`.

[109] A. Aab et al. (Pierre Auger), Nucl. Instrum. Meth. **A798**, 172 (2015), `1502.01323`.

[110] A. Albert et al. (ANTARES, IceCube, Pierre Auger, LIGO Scientific, Virgo), Astrophys. J. **850**, L35 (2017), `1710.05839`.

[111] B. F. Schutz, Nature **323**, 310 (1986).

[112] S. Nissanke, D. E. Holz, N. Dalal, S. A. Hughes, J. L. Sievers, and C. M. Hirata (2013), `1307.2638`.

[113] P. A. R. Ade et al. (Planck), Astron. Astrophys. **594**, A13 (2016), `1502.01589`.

[114] A. G. Riess et al., Astrophys. J. **826**, 56 (2016), `1604.01424`.

[115] A. W. Steiner, S. Gandolfi, F. J. Fattoyev, and W. G. Newton, Phys. Rev. **C91**, 015804 (2015), `1403.7546`.

[116] S. De, D. Finstad, J. M. Lattimer, D. A. Brown, E. Berger, and C. M. Biwer, Phys. Rev. Lett. **121**, 091102 (2018), [Erratum: Phys. Rev. Lett.121,no.25,259902(2018)], `1804.08583`.

[117] B. P. Abbott et al. (LIGO Scientific, Virgo), Phys. Rev. Lett. **121**, 161101 (2018), `1805.11581`.

[118] C. Deffayet and K. Menou, Astrophys. J. **668**, L143 (2007), `0709.0003`.

[119] K. Pardo, M. Fishbach, D. E. Holz, and D. N. Spergel, JCAP **1807**, 048 (2018), `1801.08160`.

[120] B. P. Abbott et al. (LIGO Scientific, Virgo, Fermi-GBM, INTEGRAL), Astrophys. J. **848**, L13 (2017), `1710.05834`.

[121] T. Akutsu et al. (KAGRA), Class. Quant. Grav. **36**, 165008 (2019), `1901.03569`.

[122] C. S. Unnikrishnan, Int. J. Mod. Phys. **D22**, 1341010 (2013), 1510.06059.

[123] *LSC Instrument Science White Paper Tech. rep. LIGO Scientific Collaboration*, https://dcc.ligo.org/public/0125/T1600119/004/wp2016.pdf.

[124] J. Miller, L. Barsotti, S. Vitale, P. Fritschel, M. Evans, and D. Sigg, Phys. Rev. **D91**, 062005 (2015), 1410.5882.

[125] LSC Instrument Science White Paper Tech. rep. LIGO Scientific Collaboration, *The lsc-virgo white paper on instrument science (2016-2017 edition)*, https://dcc.ligo.org/LIGO-T1600119/public.

[126] S. A. Hughes and K. S. Thorne, Phys. Rev. **D58**, 122002 (1998), gr-qc/9806018.

[127] P. R. Saulson, Phys. Rev. D **30**, 732 (1984).

[128] G. M. Harry, P. Fritschel, D. A. Shaddock, W. Folkner, and E. S. Phinney, Class. Quant. Grav. **23**, 4887 (2006), [Erratum: Class. Quant. Grav.23,7361(2006)].

[129] P. Amaro-Seoane et al., Classical and Quantum Gravity **29**, 124016 (2012).

[130] M. Armano et al., arXiv e-prints arXiv:1903.08924 (2019), 1903.08924.

[131] M. A. et. al., Classical and Quantum Gravity **26**, 094019 (2009).

[132] L. P. collaboration, Journal of Physics: Conference Series **840**, 012001 (2017).

[133] M. Armano et al., Phys. Rev. Lett. **116**, 231101 (2016).

[134] N. Seto, S. Kawamura, and T. Nakamura, Phys. Rev. Lett. **87**, 221103 (2001).

[135] S. S. et. al., Journal of Physics: Conference Series **840**, 012010 (2017).

[136] C. Cutler and J. Harms, Phys. Rev. **D73**, 042001 (2006), gr-qc/0511092.

[137] K. Yagi, Class. Quant. Grav. **29**, 075005 (2012), 1202.3512.

[138] K. Yagi, Int. J. Mod. Phys. **D22**, 1341013 (2013), 1302.2388.

[139] D. Gerosa, S. Ma, K. W. K. Wong, E. Berti, R. O'Shaughnessy, Y. Chen, and K. Belczynski, Phys. Rev. **D99**, 103004 (2019), 1902.00021.

[140] C. Cutler et al. (2019), 1903.04069.

[141] S. Vitale, Phys. Rev. Lett. **117**, 051102 (2016), 1605.01037.

[142] A. Sesana, Phys. Rev. Lett. **116**, 231102 (2016), `1602.06951`.

[143] K. W. K. Wong, E. D. Kovetz, C. Cutler, and E. Berti, Phys. Rev. Lett. **121**, 251102 (2018), `1808.08247`.

[144] E. Barausse, N. Yunes, and K. Chamberlain, Phys. Rev. Lett. **116**, 241104 (2016), `1603.04075`.

[145] Z. Carson and K. Yagi (2019), `1905.13155`.

[146] T. Robson, N. Cornish, and C. Liu, Class. Quant. Grav. **36**, 105011 (2019), `1803.01944`.

[147] C. Shi, J. Bao, H. Wang, J.-d. Zhang, Y. Hu, A. Sesana, E. Barausse, J. Mei, and J. Luo (2019), `1902.08922`.

[148] J. Aasi et al. (LIGO Scientific), Class. Quant. Grav. **32**, 074001 (2015), `1411.4547`.

[149] P. O. Mazur and E. Mottola, Proc. Nat. Acad. Sci. **101**, 9545 (2004), `gr-qc/0407075`.

[150] M. Colpi, S. L. Shapiro, and I. Wasserman, Phys. Rev. Lett. **57**, 2485 (1986).

[151] G. F. Giudice, M. McCullough, and A. Urbano, JCAP **1610**, 001 (2016), `1605.01209`.

[152] V. Cardoso and P. Pani (2019), `1904.05363`.

[153] S. O. Kepler, S. J. Kleinman, A. Nitta, D. Koester, B. G. Castanheira, O. Giovannini, A. F. M. Costa, and L. Althaus, Mon. Not. Roy. Astron. Soc. **375**, 1315 (2007), `astro-ph/0612277`.

[154] J. Antoniadis et al., Science **340**, 6131 (2013), `1304.6875`.

[155] K. Yagi and N. Yunes, Phys. Rev. **D88**, 023009 (2013), `1303.1528`.

[156] R. O. Hansen, Journal of Mathematical Physics **15**, 46 (1974).

[157] B. Carter, Phys. Rev. Lett. **26**, 331 (1971).

[158] N. Gürlebeck, Phys. Rev. Lett. **114**, 151102 (2015), `1503.03240`.

[159] F. D. Ryan, Phys. Rev. **D52**, 5707 (1995).

[160] R. Geroch, Journal of Mathematical Physics **11**, 2580 (1970).

[161] R. Geroch, Journal of Mathematical Physics **11**, 1955 (1970).

[162] R. Narayan and J. E. McClintock (2013), 1312.6698.

[163] C. Bambi (2019), 1906.03871.

[164] J. Georg and S. Watson, JHEP **09**, 138 (2017), 1703.04825.

[165] S. Shandera, D. Jeong, and H. S. G. Gebhardt, Phys. Rev. Lett. **120**, 241102 (2018), 1802.08206.

[166] A. Authors (LIGO Scientific, Virgo) (2019), 1904.08976.

[167] B. P. Abbott et al. (LIGO Scientific, Virgo) (2018), 1811.12940.

[168] J. Casares, IAU Symp. **238**, 3 (2007), astro-ph/0612312.

[169] M. Mezcua, International Journal of Modern Physics D **26**, 1730021 (2017), 1705.09667.

[170] R. P. van der Marel, in *Carnegie Observatories Centennial Symposium. 1. Coevolution of Black Holes and Galaxies Pasadena, California, October 20-25, 2002* (2003), astro-ph/0302101.

[171] S. A. Farrell, N. A. Webb, D. Barret, O. Godet, and J. M. Rodrigues, nat **460**, 73 (2009), 1001.0567.

[172] D. R. Pasham, T. E. Strohmayer, and R. F. Mushotzky (2015), [Nature513,74(2014)], 1501.03180.

[173] B. Kiziltan, H. Baumgardt, and A. Loeb, nat **542**, 203 (2017), 1702.02149.

[174] L. Ferrarese and H. Ford, Space Sci. Rev. **116**, 523 (2005), astro-ph/0411247.

[175] M. C. Begelman, R. D. Blandford, and M. J. Rees, nat **287**, 307 (1980).

[176] Event Horizon Telescope Collaboration, K. Akiyama, A. Alberdi, W. Alef, K. Asada, R. Azulay, A.-K. Baczko, D. Ball, M. Baloković, J. Barrett, et al., apjl **875**, L1 (2019).

[177] A. Boehle, A. M. Ghez, R. Schödel, L. Meyer, S. Yelda, S. Albers, G. D. Martinez, E. E. Becklin, T. Do, and J. R. Lu, apj **830**, 17 (2016), 1607.05726.

[178] S. Gillessen, P. M. Plewa, F. Eisenhauer, R. Sari, I. Waisberg, M. Habibi, O. Pfuhl, E. George, J. Dexter, and S. von Fellenberg, apj **837**, 30 (2017), 1611.09144.

[179] X.-H. Fan et al. (SDSS), Astron. J. **131**, 1203 (2006), astro-ph/0512080.

[180] X.-B. Wu, F. Wang, X. Fan, W. Yi, W. Zuo, F. Bian, L. Jiang, I. D. McGreer, R. Wang, J. Yang, et al., nat **518**, 512 (2015), 1502.07418.

[181] D. J. Mortlock, S. J. Warren, B. P. Venemans, M. Patel, P. C. Hewett, R. G. McMahon, C. Simpson, T. Theuns, E. A. Gonzáles-Solares, A. Adamson, et al., nat **474**, 616 (2011), 1106.6088.

[182] S. L. Liebling and C. Palenzuela, Living Rev. Rel. **15**, 6 (2012), [Living Rev. Rel.20,no.1,5(2017)], 1202.5809.

[183] J. Eby, C. Kouvaris, N. G. Nielsen, and L. C. R. Wijewardhana, JHEP **02**, 028 (2016), 1511.04474.

[184] E. Berti and V. Cardoso, Int. J. Mod. Phys. **D15**, 2209 (2006), gr-qc/0605101.

[185] D. F. Torres, S. Capozziello, and G. Lambiase, Phys. Rev. **D62**, 104012 (2000), astro-ph/0004064.

[186] F. H. Vincent, Z. Meliani, P. Grandclement, E. Gourgoulhon, and O. Straub, Class. Quant. Grav. **33**, 105015 (2016), 1510.04170.

[187] D. J. Kaup, Phys. Rev. **172**, 1331 (1968).

[188] R. Friedberg, T. D. Lee, and Y. Pang, prd **35**, 3658 (1987).

[189] M. Colpi, S. L. Shapiro, and I. Wasserman, Phys. Rev. Lett. **57**, 2485 (1986).

[190] V. Cardoso, E. Franzin, A. Maselli, P. Pani, and G. Raposo (2017), 1701.01116.

[191] B. Kleihaus, J. Kunz, and M. List, Phys. Rev. **D72**, 064002 (2005), gr-qc/0505143.

[192] E. W. Mielke, Fundam. Theor. Phys. **183**, 115 (2016).

[193] F. D. Ryan, Phys. Rev. D. **55**, 6081 (1997).

[194] M. A. Gunderson and L. G. Jensen, Phys. Rev. **D48**, 5628 (1993), astro-ph/9308014.

[195] D. F. Torres, Phys. Rev. **D56**, 3478 (1997), gr-qc/9704006.

[196] Z.-J. Tao and X. Xue, Phys. Rev. **D45**, 1878 (1992).

[197] M. Bezares, C. Palenzuela, and C. Bona, Phys. Rev. **D95**, 124005 (2017), 1705.01071.

[198] C. Palenzuela, P. Pani, M. Bezares, V. Cardoso, L. Lehner, and S. Liebling, Phys. Rev. **D96**, 104058 (2017), 1710.09432.

[199] V. Cardoso, E. Franzin, and P. Pani, Phys. Rev. Lett. **116**, 171101 (2016), [Erratum: Phys. Rev. Lett.117,no.8,089902(2016)], 1602.07309.

[200] C. Palenzuela, L. Lehner, and S. L. Liebling, Phys. Rev. **D77**, 044036 (2008), 0706.2435.

[201] M. Visser and D. L. Wiltshire, Class. Quant. Grav. **21**, 1135 (2004), gr-qc/0310107.

[202] K. Yagi and L. C. Stein, Class. Quant. Grav. **33**, 054001 (2016), 1602.02413.

[203] N. A. Collins and S. A. Hughes, Phys. Rev. **D69**, 124022 (2004), gr-qc/0402063.

[204] S. J. Vigeland and S. A. Hughes, Phys. Rev. **D81**, 024030 (2010), 0911.1756.

[205] C. J. Moore, A. J. K. Chua, and J. R. Gair, Class. Quant. Grav. **34**, 195009 (2017), 1707.00712.

[206] L. Barack and C. Cutler, Phys. Rev. **D69**, 082005 (2004), gr-qc/0310125.

[207] F. Ryan, Phys. Rev. D **56**, 1845 (1997).

[208] K. Glampedakis and S. Babak, Class. Quant. Grav. **23**, 4167 (2006), gr-qc/0510057.

[209] T. Johannsen and D. Psaltis, Astrophys. J. **726**, 11 (2011), 1010.1000.

[210] T. Johannsen and D. Psaltis, Astrophys. J. **716**, 187 (2010), 1003.3415.

[211] T. Johannsen and D. Psaltis, Astrophys. J. **718**, 446 (2010), 1005.1931.

[212] C. A. R. Herdeiro and E. Radu, Phys. Rev. Lett. **112**, 221101 (2014), 1403.2757.

[213] Y.-Q. Wang, Y.-X. Liu, and S.-W. Wei, Phys. Rev. **D99**, 064036 (2019), 1811.08795.

[214] S. Sen and N. Banerjee, Pramana **56**, 487 (2001), gr-qc/9809064.

[215] C. Herdeiro and E. Radu, Phys. Rev. **D89**, 124018 (2014), 1406.1225.

[216] J. F. M. Delgado, C. A. R. Herdeiro, and E. Radu (2019), 1903.01488.

[217] S. N. Zhang, W. Cui, and W. Chen, Astrophys. J. **482**, L155 (1997), astro-ph/9704072.

[218] D. F. Torres, Nucl. Phys. **B626**, 377 (2002), hep-ph/0201154.

[219] F. S. Guzman, Phys. Rev. **D73**, 021501 (2006), gr-qc/0512081.

[220] Y. Lu and D. F. Torres, Int. J. Mod. Phys. **D12**, 63 (2003), astro-ph/0205418.

[221] C. Bambi and D. Malafarina, Phys. Rev. **D88**, 064022 (2013), 1307.2106.

[222] L. Kong, Z. Li, and C. Bambi, Astrophys. J. **797**, 78 (2014), 1405.1508.

[223] A. C. Fabian, K. Iwasawa, C. S. Reynolds, and A. J. Young, Publ. Astron. Soc. Pac. **112**, 1145 (2000), astro-ph/0004366.

[224] L. W. Brenneman and C. S. Reynolds, Astrophys. J. **652**, 1028 (2006), astro-ph/0608502.

[225] C. S. Reynolds, Space Sci. Rev. **183**, 277 (2014), 1302.3260.

[226] J. Jiang, C. Bambi, and J. F. Steiner, Astrophys. J. **811**, 130 (2015), 1504.01970.

[227] J. Jiang, C. Bambi, and J. F. Steiner, Phys. Rev. **D93**, 123008 (2016), 1601.00838.

[228] A. Maselli, L. Gualtieri, P. Pani, L. Stella, and V. Ferrari, Astrophys. J. **801**, 115 (2015), 1412.3473.

[229] H. Falcke, F. Melia, and E. Agol, Astrophys. J. **528**, L13 (2000), astro-ph/9912263.

[230] A. E. Broderick, T. Johannsen, A. Loeb, and D. Psaltis, Astrophys. J. **784**, 7 (2014), 1311.5564.

[231] Event Horizon Telescope Collaboration, K. Akiyama, A. Alberdi, W. Alef, K. Asada, R. Azulay, A.-K. Baczko, D. Ball, M. Baloković, J. Barrett, et al., apjl **875**, L1 (2019).

[232] T. Binnington and E. Poisson, Phys. Rev. **D80**, 084018 (2009), 0906.1366.

[233] N. Gürlebeck, Physical Review Letters **114**, 151102 (2015), 1503.03240.

[234] É. É. Flanagan and T. Hinderer, Phys. Rev. D **77**, 021502 (2008), 0709.1915.

[235] J. Vines, É. É. Flanagan, and T. Hinderer, Phys. Rev. **D83**, 084051 (2011), `1101.1673`.

[236] N. Sennett, T. Hinderer, J. Steinhoff, A. Buonanno, and S. Ossokine, Phys. Rev. **D96**, 024002 (2017), `1704.08651`.

[237] N. K. Johnson-Mcdaniel, A. Mukherjee, R. Kashyap, P. Ajith, W. Del Pozzo, and S. Vitale (2018), `1804.08026`.

[238] N. Sennett, T. Hinderer, J. Steinhoff, A. Buonanno, and S. Ossokine, Phys. Rev. **D96**, 024002 (2017), `1704.08651`.

[239] A. Maselli, P. Pnigouras, N. G. Nielsen, C. Kouvaris, and K. D. Kokkotas, Phys. Rev. **D96**, 023005 (2017), `1704.07286`.

[240] N. Uchikata, S. Yoshida, and P. Pani, Phys. Rev. **D94**, 064015 (2016), `1607.03593`.

[241] C. V. Vishveshwara, Nature **227**, 936 (1970).

[242] O. Dreyer et al., Class. Quantum Grav. **21**, 787 (2004), `gr-qc/0309007`.

[243] E. Berti, V. Cardoso, and A. O. Starinets, Class. Quant. Grav. **26**, 163001 (2009), `0905.2975`.

[244] J. Meidam, M. Agathos, C. Van Den Broeck, J. Veitch, and B. S. Sathyaprakash, Phys. Rev. **D90**, 064009 (2014), `1406.3201`.

[245] S. Gossan, J. Veitch, and B. S. Sathyaprakash, Phys. Rev. **D85**, 124056 (2012).

[246] C. F. B. Macedo, V. Cardoso, L. C. B. Crispino, and P. Pani, Phys. Rev. **D93**, 064053 (2016), `1603.02095`.

[247] E. Berti and V. Cardoso, Int. J. Mod. Phys. **D15**, 2209 (2006), `gr-qc/0605101`.

[248] C. F. B. Macedo, P. Pani, V. Cardoso, and L. C. B. Crispino, Phys. Rev. **D88**, 064046 (2013), `1307.4812`.

[249] C. B. M. H. Chirenti and L. Rezzolla, Classical and Quantum Gravity **24**, 4191 (2007).

[250] P. Pani, E. Berti, V. Cardoso, Y. Chen, and R. Norte, PhysRevD.90.104004prd **80**, 124047 (2009), `0909.0287`.

[251] C. B. M. H. Chirenti and L. Rezzolla, Class. Quant. Grav. **24**, 4191 (2007), 0706.1513.

[252] S. Yoshida, Y. Eriguchi, and T. Futamase, Phys. Rev. **D50**, 6235 (1994).

[253] C. F. B. Macedo, P. Pani, V. Cardoso, and L. C. B. Crispino, Phys. Rev. **D88**, 064046 (2013), 1307.4812.

[254] P. Pani, E. Berti, V. Cardoso, Y. Chen, and R. Norte, Phys. Rev. **D81**, 084011 (2010), 1001.3031.

[255] P. Pani, E. Berti, V. Cardoso, Y. Chen, and R. Norte, Phys. Rev. **D80**, 124047 (2009), 0909.0287.

[256] J. B. Hartle, Phys. Rev. **D8**, 1010 (1973).

[257] K. Chatziioannou, E. Poisson, and N. Yunes, Phys. Rev. **D87**, 044022 (2013), 1211.1686.

[258] K. Chatziioannou, E. Poisson, and N. Yunes, Phys. Rev. **D94**, 084043 (2016), 1608.02899.

[259] A. Maselli, P. Pani, V. Cardoso, T. Abdelsalhin, L. Gualtieri, and V. Ferrari (2017), 1703.10612.

[260] V. Cardoso, S. Hopper, C. F. B. Macedo, C. Palenzuela, and P. Pani, Phys. Rev. **D94**, 084031 (2016), 1608.08637.

[261] R. K. L. Lo, T. G. F. Li, and A. J. Weinstein, Phys. Rev. **D99**, 084052 (2019), 1811.07431.

[262] E. Berti, V. Cardoso, and C. M. Will, Phys. Rev. D **73**, 064030 (2006), gr-qc/0512160.

[263] D. Brown et al., Phys. Rev. Lett. **99**, 201102 (2007).

[264] S. A. Hughes, Phys. Rev. D **64**, 064004 (2001).

[265] V. Cardoso, E. Franzin, A. Maselli, P. Pani, and G. Raposo (2017), 1701.01116.

[266] A. Maselli, P. Pani, V. Cardoso, T. Abdelsalhin, L. Gualtieri, and V. Ferrari (2017), 1703.10612.

[267] N. Sennett, T. Hinderer, J. Steinhoff, A. Buonanno, and S. Ossokine (2017), 1704.08651.

[268] W. G. Laarakkers and E. Poisson, Astrophys. J. **512**, 282 (1999), gr-qc/9709033.

[269] G. Pappas and T. A. Apostolatos, Phys. Rev. Lett. **108**, 231104 (2012), 1201.6067.

[270] W. G. Laarakkers and E. Poisson, Astrophys. J. **512**, 282 (1999), gr-qc/9709033.

[271] G. Pappas and T. A. Apostolatos (2012), 1211.6299.

[272] G. Pappas and T. A. Apostolatos, Physical Review Letters **108**, 231104 (2012), 1201.6067.

[273] N. Uchikata and S. Yoshida, Class. Quant. Grav. **33**, 025005 (2016), 1506.06485.

[274] L. Blanchet, Living Rev. Rel. **17**, 2 (2014), 1310.1528.

[275] L. Blanchet, T. Damour, G. Esposito-Farèse, and B. R. Iyer, Phys. Rev. Lett. **93**, 091101 (2004), gr-qc/0406012.

[276] L. Blanchet, G. Faye, B. R. Iyer, and B. Joguet, Phys. Rev. D **65**, 061501(R) (2002), Erratum-ibid **71**, 129902(E) (2005), gr-qc/0105099.

[277] L. Blanchet, T. Damour, B. R. Iyer, C. M. Will, and A. G. Wiseman, Phys. Rev. Lett. **74**, 3515 (1995), gr-qc/9501027.

[278] S. Marsat, A. Bohé, G. Faye, and L. Blanchet, Class. Quant. Grav. **30**, 055007 (2013), 1210.4143.

[279] A. Bohé, S. Marsat, G. Faye, and L. Blanchet, Class. Quant. Grav. **30**, 075017 (2013), 1212.5520.

[280] A. Bohé, S. Marsat, and L. Blanchet, Class. Quant. Grav. **30**, 135009 (2013), 1303.7412.

[281] S. Marsat, A. Bohé, L. Blanchet, and A. Buonanno, Class. Quant. Grav. **31**, 025023 (2014), 1307.6793.

[282] A. Bohé, G. Faye, S. Marsat, and E. K. Porter, Class. Quant. Grav. **32**, 195010 (2015), 1501.01529.

[283] S. Marsat, Class. Quant. Grav. **32**, 085008 (2015), 1411.4118.

[284] K. G. Arun, A. Buonanno, G. Faye, and E. Ochsner, Phys. Rev. D **79**, 104023 (2009), 0810.5336.

[285] L. E. Kidder, Phys. Rev. **D52**, 821 (1995), gr-qc/9506022.

[286] C. M. Will and A. G. Wiseman, Phys. Rev. **D54**, 4813 (1996), gr-qc/9608012.

[287] A. Buonanno, G. Faye, and T. Hinderer, Phys. Rev. **D87**, 044009 (2013), 1209.6349.

[288] C. K. Mishra, A. Kela, K. G. Arun, and G. Faye, Phys. Rev. **D93**, 084054 (2016), 1601.05588.

[289] E. Poisson, Phys. Rev. **D57**, 5287 (1998), gr-qc/9709032.

[290] S. Marsat, Class. Quant. Grav. **32**, 085008 (2015), 1411.4118.

[291] C. Cutler and E. Flanagan, Phys. Rev. D **49**, 2658 (1994).

[292] M. Vallisneri, Phys. Rev. D **77**, 042001 (2008), gr-qc/0703086.

[293] C. Van Den Broeck and A. S. Sengupta, Class. Quantum Grav. **24**, 1089 (2007), gr-qc/0610126.

[294] K. G. Arun, B. R. Iyer, B. S. Sathyaprakash, S. Sinha, and C. Van Den Broeck, Phys. Rev. D **76**, 104016 (2007), 0707.3920.

[295] S. Husa et al., Phys. Rev. **D93**, 044006 (2016), 1508.07250.

[296] M. Favata, K. G. Arun, C. Kim, J. Kim, and H. W.Lee (In preparation).

[297] R. Balasubramanian and S. V. Dhurandhar, Phys. Rev. D **57**, 3408 (1998).

[298] M. Armano et al., Phys. Rev. Lett. **116**, 231101 (2016).

[299] N. Uchikata and S. Yoshida, Class. Quant. Grav. **33**, 025005 (2016), 1506.06485.

[300] N. V. Krishnendu et al. (In preparation).

[301] M. Campanelli, C. O. Lousto, and Y. Zlochower, Phys. Rev. **D79**, 084012 (2009), 0811.3006.

[302] N. V. Krishnendu, K. G. Arun, and C. K. Mishra, Phys. Rev. Lett. **119**, 091101 (2017), 1701.06318.

[303] LIGO Scientific Collaboration, https://wiki.ligo.org/DASWG/LALSuite (2018).

[304] K. G. Arun, A. Buonanno, G. Faye, and E. Ochsner, Phys. Rev. **D79**, 104023 (2009), [Erratum: Phys. Rev.D84,049901(2011)], 0810.5336.

[305] A. Buonanno and T. Damour, Phys. Rev. **D59**, 084006 (1999), gr-qc/9811091.

[306] M. Hannam, P. Schmidt, A. Bohé, L. Haegel, S. Husa, F. Ohme, G. Pratten, and M. Pürrer, Phys. Rev. Lett. **113**, 151101 (2014), 1308.3271.

[307] A. Taracchini et al., Phys. Rev. **D89**, 061502 (2014), 1311.2544.

[308] A. Buonanno and T. Damour, Phys. Rev. **D62**, 064015 (2000), gr-qc/0001013.

[309] P. Ajith et al., Phys. Rev. Lett. **106**, 241101 (2011).

[310] N. V. Krishnendu, C. K. Mishra, and K. G. Arun, Phys. Rev. **D99**, 064008 (2019), 1811.00317.

[311] LIGO Scientific Collaboration, https://www.advancedligo.mit.edu/ (2018).

[312] G. M. Harry (LIGO Scientific), Class. Quant. Grav. **27**, 084006 (2010).

[313] LIGO Scientific Collaboration, https://dcc.ligo.org/LIGO-M060056/public (2009).

[314] F. Acernese and P. A. et.al., Classical and Quantum Gravity **23**, S635 (2006).

[315] F. Acernese et al. (VIRGO), Class. Quant. Grav. **32**, 024001 (2015), 1408.3978.

[316] LIGO Scientific Collaboration, https://dcc.ligo.org/cgi-bin/private/DocDB/ShowDocument?docid=T1800044&version=5 (2018).

[317] LIGO Scientific Collaboration, https://dcc.ligo.org/LIGO-T1000218/public (2018).

[318] E. Baird, S. Fairhurst, M. Hannam, and P. Murphy, Phys. Rev. **D87**, 024035 (2013), 1211.0546.

[319] N. Cornish, L. Sampson, N. Yunes, and F. Pretorius, Phys. Rev. **D84**, 062003 (2011), 1105.2088.

[320] W. Del Pozzo, K. Grover, I. Mandel, and A. Vecchio, Class. Quant. Grav. **31**, 205006 (2014), 1408.2356.

[321] LIGO Scientific Collaboration, https://www.gw-openscience.org/data/ (2009).

[322] B. Sathyaprakash et al., in *Proceedings, 46th Rencontres de Moriond on Gravitational Waves and Experimental Gravity: La Thuile, Italy, March 20-27, 2011* (2011), pp. 127–136, 1108.1423.

[323] T. Regimbau et al., Phys. Rev. **D86**, 122001 (2012), 1201.3563.

[324] S. Hild et al., Class. Quant. Grav. **28**, 094013 (2011), 1012.0908.

[325] S. Hild, S. Chelkowski, and A. Freise (2008), 0810.0604.

[326] M. Vallisneri, Phys. Rev. **D77**, 042001 (2008).

[327] E. Weinstein and A. J. Weiss, IEEE Transactions on Information Theory **34**, 338 (1988), ISSN 0018-9448.

[328] K. G. Arun, B. R. Iyer, B. S. Sathyaprakash, and S. Sinha, Phys. Rev. **D75**, 124002 (2007).

[329] S. Dwyer, D. Sigg, S. W. Ballmer, L. Barsotti, N. Mavalvala, and M. Evans, prd **91**, 082001 (2015), 1410.0612.

[330] E. Barausse, Mon. Not. Roy. Astron. Soc. **423**, 2533 (2012), 1201.5888.

[331] A. Sesana, E. Barausse, M. Dotti, and E. M. Rossi, Astrophys. J. **794**, 104 (2014), 1402.7088.

[332] F. Antonini, E. Barausse, and J. Silk, Astrophys. J. **806**, L8 (2015), 1504.04033.

[333] F. Antonini, E. Barausse, and J. Silk, Astrophys. J. **812**, 72 (2015), 1506.02050.

[334] M. Bonetti, A. Sesana, F. Haardt, E. Barausse, and M. Colpi, Mon. Not. Roy. Astron. Soc. **486**, 4044 (2019), 1812.01011.

[335] M. Volonteri, F. Haardt, and P. Madau, Astrophys. J. **582**, 559 (2003), astro-ph/0207276.

[336] A. Sesana, M. Volonteri, and F. Haardt, Class. Quant. Grav. **26**, 094033 (2009), 0810.5554.

[337] M. Volonteri, F. Haardt, P. Madau, and A. Sesana (2003), [Astrophys. Space Sci. Libr.301,227(2004)], astro-ph/0310211.